2013

Zinc Environment in Proteins: The Flexible and Reactive Core of HIV-1 NCp7 and The Inhibitory Site of Caspase-3

A. Gerard Daniel
Virginia Commonwealth University

Zinc Environment in Proteins:
The Flexible and Reactive Core of HIV-1 NCp7
and
The Inhibitory Site of Caspase-3

A dissertation submitted in partial fulfillment of the requirements for the degree of Doctor of Philosophy in Chemistry at Virginia Commonwealth University.

by

Amalanayagame Gerard Daniel
Master of Philosophy in Chemistry
Pondicherry University, 2006

Director: Nicholas P. Farrell, Ph. D.
Professor, Department of Chemistry

Virginia Commonwealth University
Richmond, Virginia
December, 2013

Acknowledgment

I am grateful to my advisor, Dr. Nicholas P. Farrell, for all his counsel and support. I greatly appreciate that he let me pursue my fascination for computational chemistry and molecular biology in my research. I sincerely thank my dissertation committee members, Dr. James Terner, Dr. Dusan Bratko, Dr. Glen Kellogg, Dr. Matthew Hartman and Dr. Craig Bayse, for their helpful discussions and suggestions. I extend my hearty thanks to Erica, a great friend to share my woes and naïve philosophies, without her help and advice, a great part of my thesis would not have been possible. I would also like to thank my friend Vijay for his help in the lab and some "wonderful" tea time. I would like to thank my previous and present lab mates, Sarah, Samantha, Daniel, João, Susana, Queite, Camilla, Carolina and Bruno for being cordial and helpful. I would like to thank all my friends, especially, Mike, Suresh, Bala and Dev for being great roommates and also Tanu & Nitai, Hema & Kalyan, Debo, Spanny, Gunjan & Ketan, Shanthi, Sudhu, Logu and Vereen: thank you all for the fun moments. I specially thank my family for their love and support.

I would like to thank Virginia Commonwealth University and the Department of Chemistry for the opportunities and financial support. I am grateful to Altria for their support through a fellowship.

Table of Contents

List of Tables

List of Figures

Abstract

ZINC ENVIRONMENT IN PROTEINS: THE FLEXIBLE AND REACTIVE CORE OF HIV-1 NCP7 AND THE INHIBITORY SITE OF CASPASE-3

By Amalanayagame Gerard Daniel, M. Phil.

A dissertation submitted in partial fulfillment of the requirements for the degree of Doctor of Philosophy in Chemistry at Virginia Commonwealth University.

Virginia Commonwealth University, 2013.

Major Director: Nicholas P. Farrell, Ph. D., Professor, Department of Chemistry

Zinc is an essential cofactor of several proteins. The roles of zinc in these proteins are classified as catalytic, structural or regulatory. Zinc present in structural sites is considered to be a chemically inert, static structural element. On the contrary, previous studies on a C_2H_2 type zinc finger model compound and the C_3H type HIV-1 NCp7 C-terminal zinc knuckle have shown that zinc at these sites can undergo coordination sphere expansion under the influence of a Pt based electrophile. The pentacoordination observed around zinc in these experiments raises an important question: are the structural zinc motifs found in the proteins susceptible to coordination sphere expansion? Through DFT modeling, the existence and nature of the five

coordinate zinc species was investigated. mPW1PW91 was chosen as the DFT method by benchmarking against the experimental parameters of a molecule that closely resembles those to be modeled. The results suggest that the observed coordination sphere expansion is due to the flexible nature of thiolate and chloride ligands that are part of the structure. However, if certain conditions are not met, the same flexibility can lead to the destabilization of these rather fragile structures.

Unlike the stable three or four coordinate catalytic and structural zinc sites, at regulatory sites, zinc is typically bound to one or two protein ligands. Zinc inhibition of caspases which are central to the process of apoptosis is one such scenario. Several of the caspases are inhibited by zinc at low micromolar range. Regulation of caspases is a strategy for drug development toward apoptosis related diseases; thus it is important to know the molecular details of zinc inhibition of caspases. Currently, it is speculated that zinc binds to the active site His and Cys residues of caspases thus competing with the substrate. However our studies on caspase-3, using enzyme kinetics and biophysical methods, imply more than one zinc binding sites. Contrary to current beliefs, more than 50% of the inhibition is achieved by zinc without affecting substrate binding. Using DFT models, an alternative inhibitory zinc binding site, which better fits our experimental observations, is predicted.

1. General Introduction

1.1. Role of Metals in Biology

Metals or metal clusters are cofactors of proteins which perform life sustaining, fundamental biological processes such as photosynthesis, respiration, electron transfer etc.[1] Prevalence of metals in biology can be perceived by considering that about 30% of all proteins bind to metals[2] and about half of all enzymes require metals for their function. Metalloproteins are found in all six classes of Enzyme Commission and thus are inevitable for cellular metabolism, growth and homeostasis.[3] In earlier stages of evolution, metalloproteins would have evolved based on the abundance of metals in the species' immediate environment[4] and based on the relative affinities of these metals as given by the Irving – William series:[5]

$$\mathbf{Mg^{2+}/Ca^{2+} < Mn^{2+} < Fe^{2+} < Co^{2+} < Ni^{2+} < Cu^{2+} \sim Zn^{2+}}$$

However the unique chemical properties of each metal often makes it harder to be replaced without much loss of function. The fact that Photosystem II has changed very little since the time of its evolution about 2.5 billion years ago,[6] proves that the metals central to the intermediary processes in the conversion of light energy to chemical energy are well suited for their function and are irreplaceable. The functions of the metal ions are highly correlated to their chemical properties. The monovalent alkali metals such as Na^+ and K^+, which are highly mobile, are used as charge carriers and to maintain osmotic balance.[7] Several of the transition metals that can exist in multiple oxidation states (Fe, Co, Mn, Mo, etc.) are utilized to catalyze redox reactions,

electron transport and small molecule transport. Divalent cations Mg^{2+}, Ca^{2+} and Zn^{2+}, which are redox inert, are commonly employed as structural elements. Among these Mg^{2+}, being a hard acid, has a great affinity towards oxygen ligands and is often associated with phosphate groups, stabilizing the nucleic acid backbones and in phosphoryl transfer reactions. Ca^{2+} is well known as a secondary messenger in signal transmission and recent discoveries suggest that Zn^{2+} can act as a secondary messenger too.[8]

Zinc is the second most common transition metal in biology. It is estimated that the zinc proteome makes up 4 to 10% of the genome of an organism.[9] The advent of zinc in proteins marks an important stage in eukaryotic evolution since it accelerated diversification.[4] Zinc is vital for the functioning of many proteins. In these proteins, based on its function, zinc is known to bind to three types of sites: structural, catalytic or cocatalytic and inhibitory sites.[7,10,11] The choice of Zn in these diverse functioning proteins is due to a set of desirable properties stemming from its electronic structure.

1.2. Zinc Chemistry in Biology

The following are the unique properties and their applicability for the many roles of Zn in proteins. Zinc is a borderline Lewis acid;[12] the most important consequence of this property is that it is capable of binding to all four major protein ligands[7] (His, Asp, Glu and Cys) and water, covering three elements N, O and S. Asp and Glu are hard bases, His is a borderline base while Cys is a soft base, Zn^{2+} being a borderline acid, however, has enough affinity to all these ligands.[13] The Lewis acidity is also useful during catalysis to activate the exogenous ligand, which frequently is a water molecule.[14] Of course there are other transition metal ions, such as Fe^{2+}, Co^{2+}, Ni^{2+} and Cu^{2+}, which are borderline acids too, but they lack another desirable property that Zn^{2+} possesses: namely its redox inertness due to a stable d^{10} electronic

configuration. It is the combination of these two properties that allows Zn^{2+} to have a variety of coordination spheres to fine tune its Lewis acidity,[15] while the metal itself is not involved in any complete electron transfer process. The redox inertness is mainly useful for proteins in which zinc ions help maintain their structural integrity. The importance of this can be better appreciated by knowing the fact that some of these structural proteins known as zinc fingers act as transcription factors, that bind to DNA. Here, the redox inertness of the metal is important to avoid any damage to the DNA.[16] In addition to the redox inertness, the d^{10} configuration gives rise to one more property that makes Zn^{2+} even more versatile: a completely filled d-orbital implies that there is no ligand field stabilization involved during the process of complex formation.[16] Therefore, the coordination number and the geometry around the metal are said to be enforced by the bulkiness of the ligands and the charge on them;[7] nevertheless, metal empty s and p orbitals may play a role. Thus, the coordination environment is quite flexible allowing expansion or reduction in the number of ligands without much of an energy cost. This property is useful for fast ligand exchange that is often involved in the catalytic sites of zinc. Although the most prevalent geometry around Zn in proteins is found to be distorted tetrahedron, other lower or higher coordination geometries are also seen. An analysis of the PDB database shows that the coordination number of Zn can be any number from 2 to 6, with 4 being the most common.[17] The flexibility to have lower coordination numbers such as 2 or 3 may be required for the inhibitory action of zinc where zinc needs to bind reversibly depending on its concentration.[18] While tetra coordination is the only mode found in structural Zn sites, catalytic sites with Zn in five coordination state are prevalent.

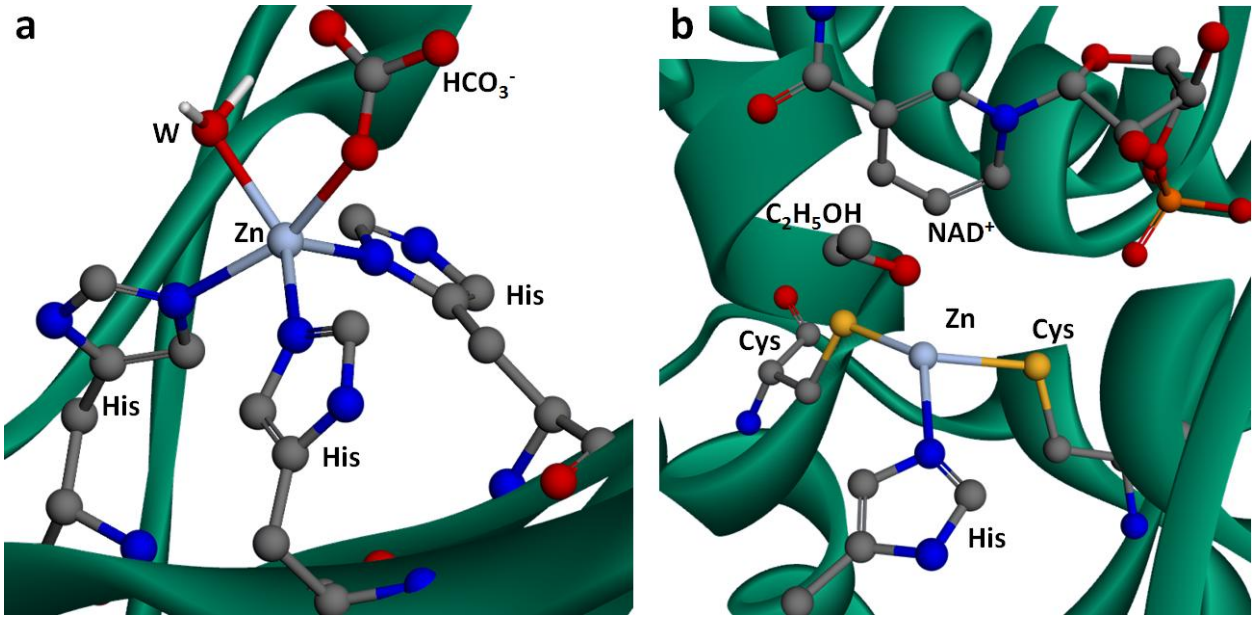

Figure 1.1. Examples of catalytic zinc sites: a) active site of carbonic anhydrase with zinc bound to three His residues, a water molecule and a bicarbonate ion are shown (PDB ID: 1CAM).[19] Zinc acts a dual role of activating the water molecule and positioning the substrate. b) active site of alcohol dehydrogenase with zinc bound to a His, two Cys residues and a trifluoroethanol molecule (F atoms not shown) are shown (PDB ID: 1AXG).[20] Zinc helps to position the substrate facilitating a hydride transfer to a NAD^+ molecule.

1.3. Catalytic Zinc Sites

In a catalytic site, Zn^{2+} may be involved in any or a combination of these three functions: i) activation of the substrate as in metallo-β-lactamase[21] or activation of a water molecule by polarization as in carbonic anhydrase[19] (Figure 1.1a) ii) recognition and positioning of the substrate as in alcohol dehydrogenase[20] (Figure 1.1b) and cysteine t-RNA synthetase[22] and iii) stabilization of the reaction intermediate as in metallo-β-lactamase[21] and carboxypeptidase.[23] The common feature of a catalytic zinc site is a tetrahedral geometry with 3 protein ligands and a water molecule as the fourth ligand. The water molecule may be utilized during the catalysis or just displaced by the incoming substrate. The most common protein ligands in a catalytic site are His and Glu but Asp and Cys do occur but less frequently.[24,25] Though tetrahedral geometry is

predominant, five coordinate catalytic sites with four protein ligands and a water molecule also exist, the well known example is the carboxypeptidases,[23] where two His residues, a Glu residue and a water molecule are ligands for Zn. Asp and Glu residue can act as either a mono-dentate or a bi-dentate ligand.[26] The ability of Zn^{2+} to accommodate an extra ligand may facilitate the stabilization of the reaction intermediate during the reaction pathway.

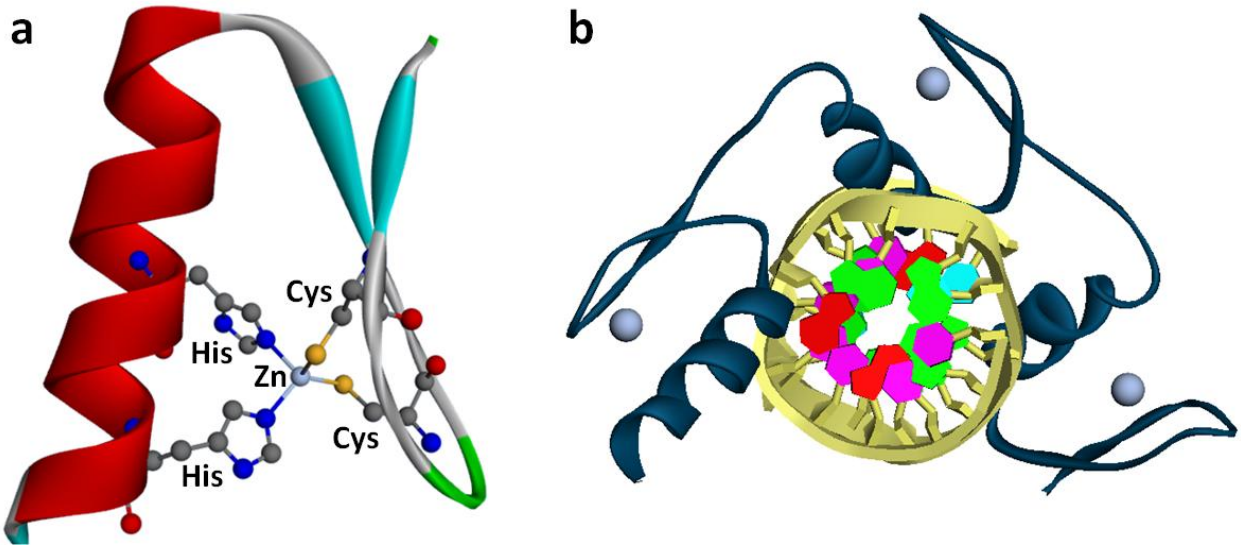

Figure 1.2. An example of a structural zinc site: transcription factor Zif268 (TFIIIA-like zinc finger) (PDB ID: 1AAY):[27] a) a single zinc finger domain with zinc atom and its four ligands are shown. b) three zinc finger domains (blue) in tandem bound to a short DNA duplex (yellow, top-down view). Light blue spheres are Zn^{2+}.

1.4. Structural Zinc Sites

Often the tertiary structure of proteins is formed by stabilizing noncovalent interactions such as van der Waals interactions, cation-π interactions and hydrogen bonds. However covalent interaction such as disulphide bonds is also common. Yet another way to stabilize small domains is by binding to metal ions, commonly Zn^{2+}. These structural zinc sites are indispensible for the functioning of several proteins. The usual feature of a structural zinc site is tetracoordinate zinc with His and Cys as ligands.[25] When compared to a catalytic site where His is the most common

ligand followed by Glu and Asp, in structural sites, Cys is the most common followed by His, while Glu and Asp are seldom found. A prevalent class of structural zinc proteins is known as the Zinc Fingers (ZF) (Figure 1.2a).[16] The first discovered zinc finger was the transcription factor TFIIIA. The protein was named zinc finger because it grasped DNA using DNA binding domains formed by zinc coordination to two Cys and two His residues (Figure 1.2b). Similar structural zinc domains have been identified later with other types of coordination environments.

1.4.1. Classification of Zinc Finger Domains and Proteins

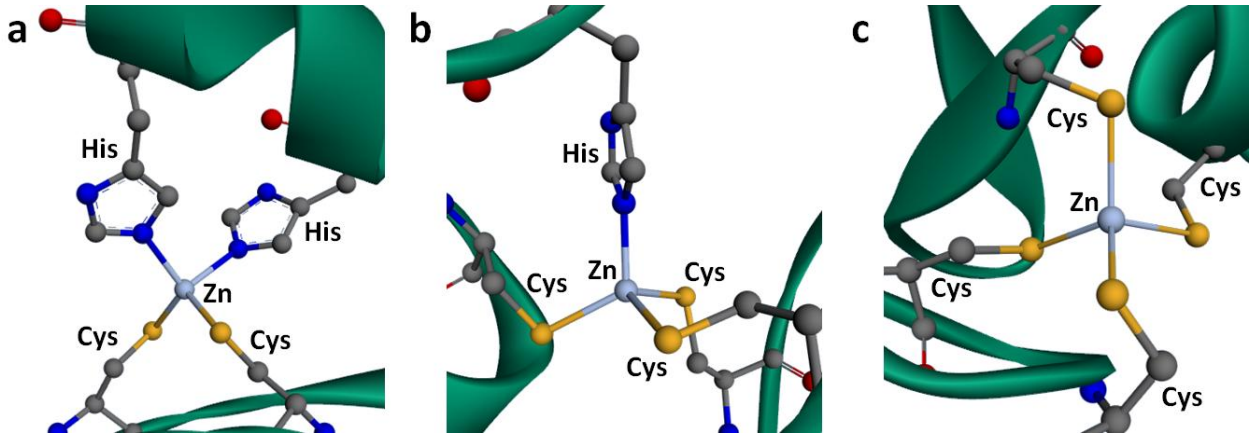

Figure 1.3. Three types of zinc finger cores classified by their coordination environment: a. C_2H_2 type (PDB ID: 2J7J),[28] b. C_3H type (PDB ID: 3KNV),[29] and c. C_4 type (PDB ID: 3DFX).[30]

Zinc fingers can be classified into three types based on their coordination environment. The first type is where zinc is bound to two Cys and two His (C_2H_2 type) (Figure 1.3a), which is the most abundant DNA binding motif in the human genome. It has the ability to mediate binding to both RNA and DNA. The second type has three Cys and one His as zinc ligands (C_3H type) (Figure 1.3b). Based on the sequence it can be further classified to C_2HC or C_2CH types. The HIV nucleocapsid protein NCp7 is a C_2HC type zinc knuckle. The third type has all four Cys bound to zinc (C_4 type) (Figure 1.3c). An example of this is the GATA transcription factor.

These three zinc finger cores form the basis of structurally diverse zinc finger proteins that can be again classified based on the fold or tertiary structure that they stabilize.[31]

Currently tertiary structures formed by zinc fingers are classified into eight fold groups: C_2H_2-like, Gag knuckle, treble clef, zinc ribbon, Zn2/Cys6, TAZ2 domain-like, zinc binding loops and metallothionein. However most zinc fingers fall under three major fold groups which are C_2H_2-like finger, treble clef finger and the zinc ribbon.[31,34] The structural aspects of the C_2H_2-like finger and Gag knuckle are under the scope of this thesis and hence will be briefed here.

The C_2H_2-like finger can be identified by the structural feature of a β-hairpin followed by an α-helix. The two cysteines are part of the two β-sheets comprising the β-hairpin and the two histidines are part of the α-helix. Thus, on binding to zinc, together they form a left handed ββα-unit (Figure 1.2a). Each of the domains consists of 28-30 amino acids. The consensus sequence of these ZFs is given by (F/Y)-X-C-X_{2-5}-C-X_3-(F/Y)-X_5-ψ-X_2-H-X_{3-5}-H, where X is any amino acid and ψ is a hydrophobic residue. The aromatic amino acid residue in the middle and the hydrophobic residue form a hydrophobic core which helps in stabilizing the fold. These domains are linked in tandem (Figure 2b) by a short five amino acid linker, forming a nucleic acid sequence recognition moiety.[32] Most cellular transcription factor zinc fingers are of this type.

The Gag knuckles are however shorter, made of about 20 amino acids and usually feature very little secondary structure even when bound to zinc. The consensus sequence is given by X_3-C-X_2-C-X_4-H-X_4-C-X_3, where X stands for any amino acid. The linker in the middle is shorter compared to the C_2H_2-like finger. Most proteins in this family have two of these domains separated by a short linker.[31] The HIV-1 retroviral nucleocapsid protein NCp7 is of this type.

1.4.2. Characteristics and Function of Zinc Finger Proteins

The main function of most zinc finger proteins is site specific binding to nucleic acid sequences for transcription control but interactions with other proteins have also been reported.[33,34] The nucleic acid binding activity is promoted by the fold of zinc finger domains along with specific amino acid interactions with the bases and the backbone of the nucleic acid. Hence as any nucleic acid binding protein, zinc finger proteins contain many basic and aromatic amino acid residues. From the crystal structure of Zif268 (C_2H_2-like finger) in complex with a DNA oligomer, we know that the α-helix binds to the major groove of DNA using electrostatic interactions from His, Glu and Thr to the DNA bases. Additionally, basic amino acids Arg and Lys, from the β-sheets, make contact with the DNA backbone phosphate groups.[35]

1.5. Inhibitory Zinc Sites

An inhibitory or regulatory role of zinc is a late addition to its well studied catalytic and structural roles. The first enzyme reported to be inhibited by zinc is Carboxypeptidase A, which is a zinc enzyme by itself.[36] The catalytic zinc is found adjacent to the inhibitory zinc which is bound to a glutamate residue and to a hydroxyl group bridging to the catalytic zinc (Figure 1.4).[37] Now several enzymes have been shown to be inhibited by zinc in vitro.[38] Since, the inhibitory concentration of Zn^{2+} in most cases is above physiological Zn^{2+} concentration, their relevance is being questioned. However, regulatory role requires reversibility of function. Hence these zinc binding sites should be kinetically labile or of low affinity. Since zinc binds to protein ligands strongly, binding to fewer ligands would be better for the sake of reversibility.

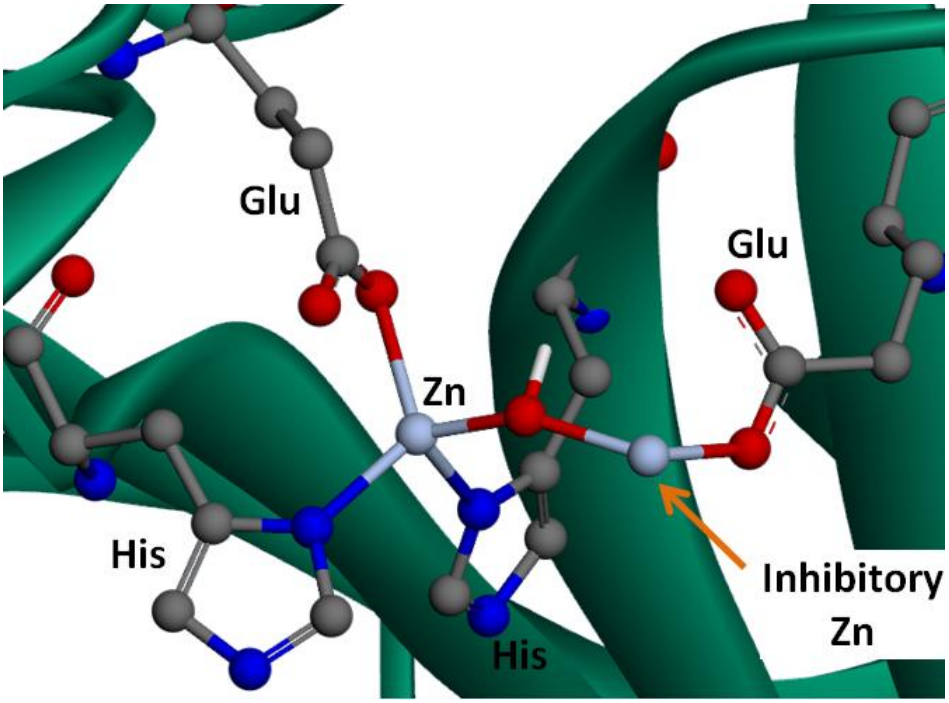

Figure 1.4. Active site of Carboxypeptidase A bound to both the catalytic Zn^{2+} and the inhibitory Zn^{2+} (PDB ID: 1CPX).[37] The light blue spheres are Zn^{2+}. The inhibitory zinc is bound to just one protein ligand.

However, the lower binding affinity of Zn^{2+} towards enzymes is also the limiting factor that makes characterization of such binding sites challenging. Even prediction of such sites is difficult due to the lack of knowledge about general characteristics of inhibitory zinc binding sites and the absence of predictable domains as in structural zinc binding sites. Nevertheless, a few recently characterized inhibitory zinc sites have been summarized.[18] A common feature of these is zinc binding to fewer ligands or to uncommon protein ligands such as Ser and Lys. Based on these few known sites, zinc inhibitory sites have been classified into three types: inhibition by binding at the active site of non-zinc enzymes, allosteric inhibition, and as a special case, binding of a second Zn^{2+} near the catalytic Zn^{2+} as in Carboxypeptidase A.

1.6. Purpose and Scope of the Thesis

The first part of the thesis is aimed at understanding the chemistry involved in coordination sphere expansion of Zn^{2+} that are present in structural sites. In the second part of the thesis, an approach to elucidate the molecular details of inhibitory zinc site in caspases is described. These cases represent the less common zinc coordination environments, where the coordination number is either higher or lower than the most common values (3 and 4) that are found in protein. Hence, general characteristics that may be used to describe and understand such zinc sites are sparse. The purpose of this thesis is to broaden the aspects of zinc coordination chemistry, by studying the molecular aspects of these less common, nevertheless, biologically significant zinc coordination environments.

Much of what is known, about the structure and chemistry of zinc sites in proteins, comes from X-ray crystallography and theoretical calculations. Zn^{2+} with a d^{10} electronic configuration and a nuclear spin of zero is incompatible with the commonly used spectroscopic techniques such as UV-Visible, EPR and NMR spectroscopy. Therefore, the dynamic changes around Zn^{2+} that occurs during coordination to its ligands or during a reaction is hard to be observed. Co^{2+} and Cd^{2+} are often used as a substitute for Zn^{2+} to study such changes, which has proved to be useful.[39,40] Nevertheless such substitution may not be practical in all cases, which is true with the scenarios presented in this thesis. In the chapters below, the background that is required to understand the problem and to interpret the results, followed by the experimental results, which were used to derive speculations about the zinc coordination environments and DFT models, which were used to evaluate the stability and to gain structural insights about the species, are presented.

PART I

The Flexible and Reactive Core of HIV-1 NCp7

2. Introduction

Zinc finger motifs are designed to maintain the structural integrity of the protein and to orient the aromatic and positively charged residues for interaction with nucleic acids. The tetra coordination of zinc gives little room for any more ligands,[41] thus the structure is considered to be static and stable. But recent discoveries show that the sulfur ligands in the core may be reactive.

2.1. Reactivity of Zinc Bound Thiolates in Structural Zinc Sites

The reactivity varies by the type of zinc coordination sphere, increasing with increasing number of sulfur ligands. Several studies using zinc finger model compounds have elucidated the effect of zinc ligands and stabilizing hydrogen bonding on the reactivity of zinc bound thiolates.[26,42,43] A few enzymes such as the ADA repair protein,[44] methyl reductase[45] and methionine synthase[46] are known to utilize this reactivity to form carbon-sulfur bonds. From a therapeutic perspective this reactivity can be targeted to inactivate viral zinc finger proteins such as HIV-1 NCp7.[47]

2.2. Structure and Function of HIV-1 NCp7 Zinc Finger Protein

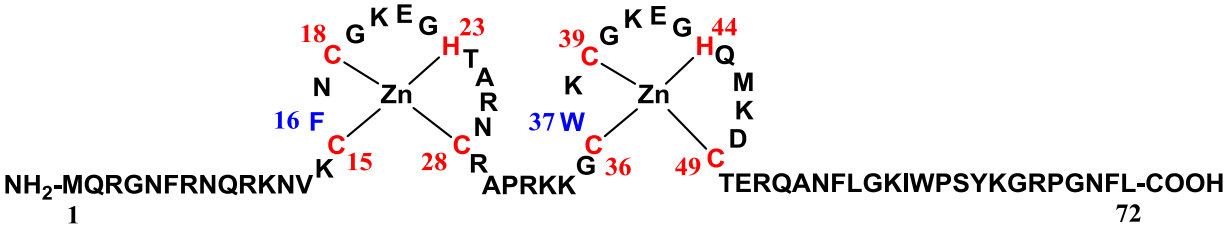

Figure 2.1. Sequence of HIV-1 NCp7 and the two constituent zinc knuckle are shown. The coordinating residues are in red and the aromatic amino acids involved in nucleic acid binding are in blue.

The HIV-1 NCp7 is a 72 amino acid polypeptide with two Cys-X_2-Cys-X_4-His-X_4-Cys (C_2HC) zinc finger motifs separated by a short linker.[48] The zinc binding affinity of this retroviral type motif is higher than the normal cellular zinc fingers.[49] The entire sequence with the key residues numbered is shown in Figure 2.1. The two aromatic amino acids in blue are important for RNA binding.[50] The protein is completely flexible except for the zinc finger knuckles.[48] Both zinc fingers are shown to be structurally similar; however, the C-terminal zinc finger is seen to be more dynamic compared to the N-terminal one.[26] Unlike the C_2H_2-like zinc fingers, which preferably binds to double stranded DNA, these knuckles are designed to bind to single stranded DNA and RNA molecule.[16] A solution NMR structure of HIV-1 NCp7 bound to a DNA molecule reveals the motifs involved in nucleic acid recognition (Figure 2.2). Here, the flexibility of the single stranded DNA is exploited by the aromatic residues of the protein to π-stack with the bases on the nucleic acid. Several hydrogen bonding interactions, between basic amino acid residues and the nucleic acid backbone, further stabilize the complex.[51]

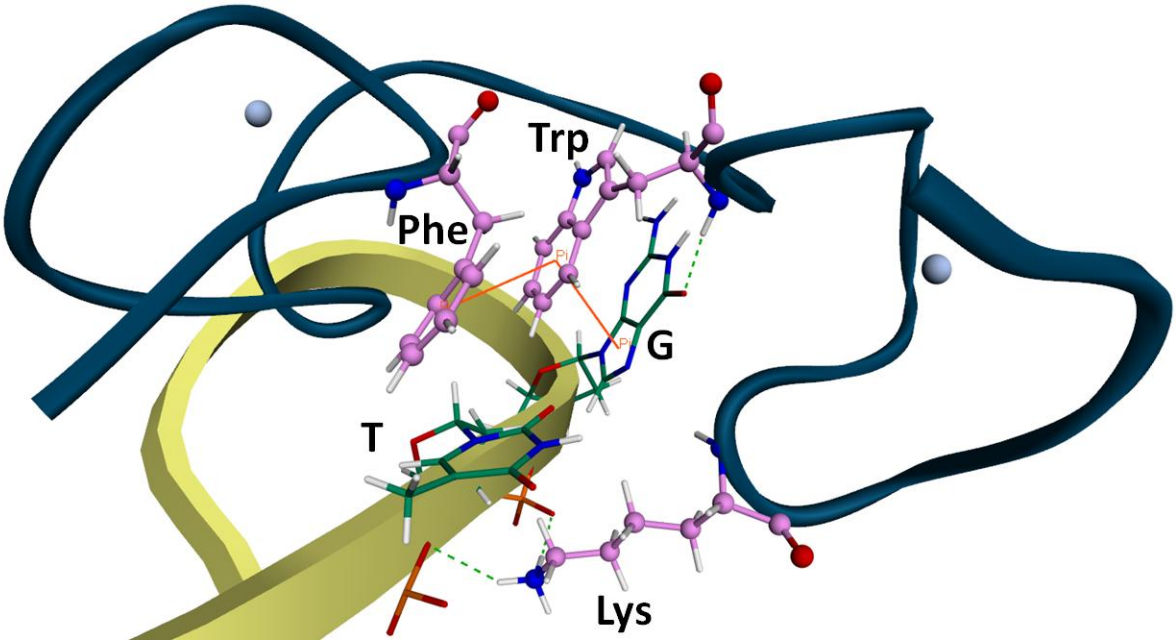

Figure 2.2. HIV-1 NCp7(blue) bound to single strand 18-mer DNA (yellow) (PDB ID:2JZW)[51]: A few primary contacts are shown. Trp and Phe are involved in π-stacking with the Guanine and Thymine bases. A Lys in contact with the phosphate back bone is shown.

2.3. HIV-1 NCp7 as a Drug Target

The sulfur ligands of zinc fingers can react with a number of electrophilic agents, with the concomitant release of zinc. This reactivity is used strategically to target the NCp7 zinc fingers.[47,49] The NCp7 protein is involved in multiple processes during the viral lifecycle[52] and is considered mutationally nonpermissive,[53] which makes it a potential target for drug development. Similarly studies have shown that the C-terminal zinc finger is more reactive towards electrophilic agents.[54] Specifically, Cys49 of the C-terminal finger is known to be easily dissociable and reactive towards electrophiles.[55] Nevertheless there are other reports of involvement of Cys36[56] and Cys39[57] in electrophilic attacks.

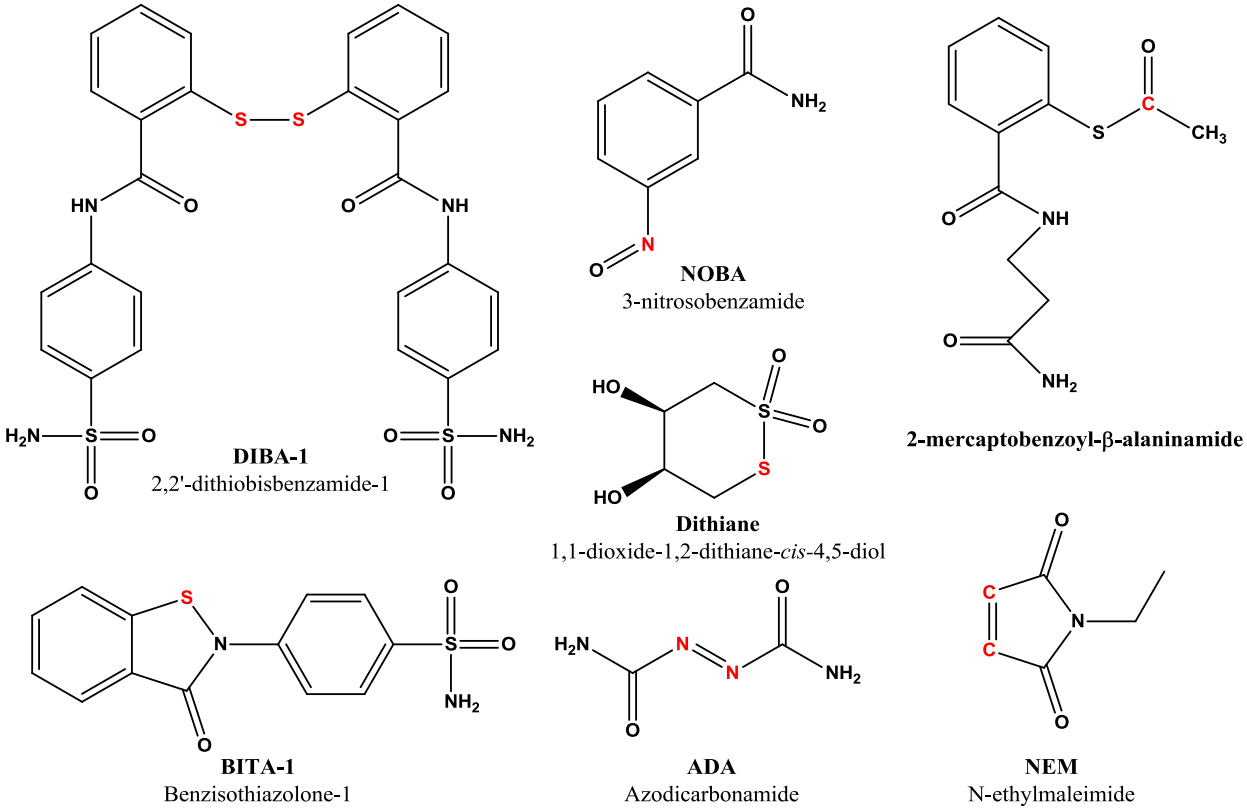

Figure 2.3. Representative electrophilic chemotypes used to target NCp7. The electrophilic centers are shown in red.

Many electrophilic compounds have been tested for activity against NCp7 zinc fingers. A variety of chemotypes such as disulfide, C-nitroso compounds, thioester, isothiazolone, dithiaheterocyclic compounds, α-carbonyl azoic compounds and many others have been shown active.[47,49,52] The representatives of these compounds are shown in Figure 2.3, with the electrophilic centers in red. These compounds act by covalently binding to the zinc bound thiolates and thereby inducing ejection of zinc, ultimately leading to loss of activity.

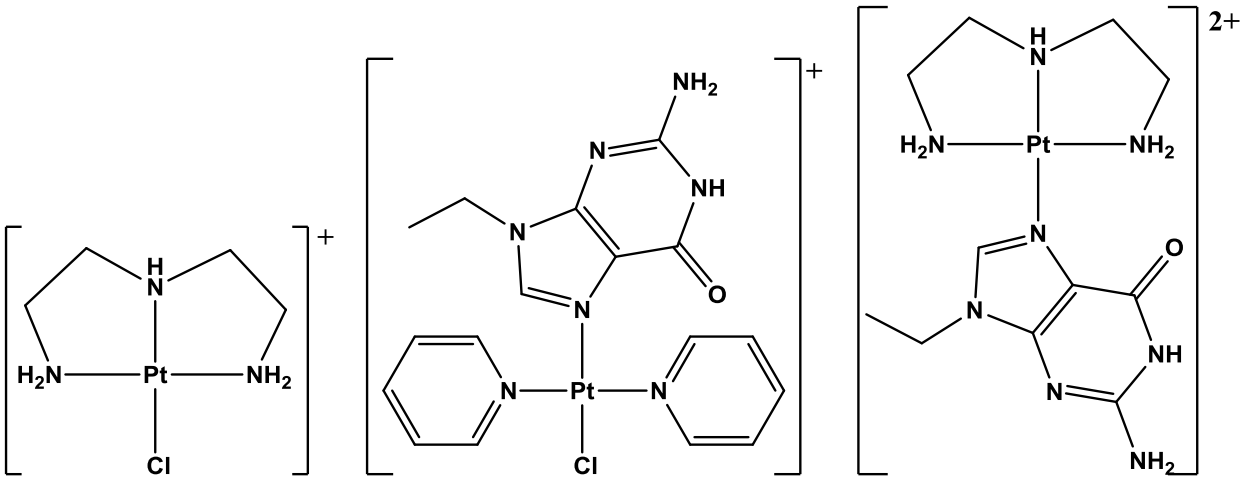

Figure 2.4. Monofunctional and non-covalent Pt compounds designed to target NCp7. The 9-Ethylguanine moiety in the later two compounds would target the Trp in the zinc finger protein.

As an alternate, trans-platinum compounds have shown encouraging results as antiviral agents (Figure 2.4).[58] In monofunctional trans-platinum complexes, the electrophilic Pt targets the zinc bound thiolates of NCp7. In addition, the coordination sites in Pt can be used to bind nucleobases such as 9-ethylguanine to improve the specificity towards NCp7 by targeting its Trp residue. On the other hand, noncovalent compounds such as $[Pt(9\text{-}EtGua)(dien)]^{2+}$ have been developed to antagonize the interactions between NCp7 and nucleic acids.[59] Mass spectrometry studies of interaction of these compounds with both zinc finger model compounds and the NCp7 C-terminal zinc finger have shown that these drugs can eject zinc or undergo metal replacement reactions.[59,60]

2.4. Reactivity of Zinc in Zinc finger proteins

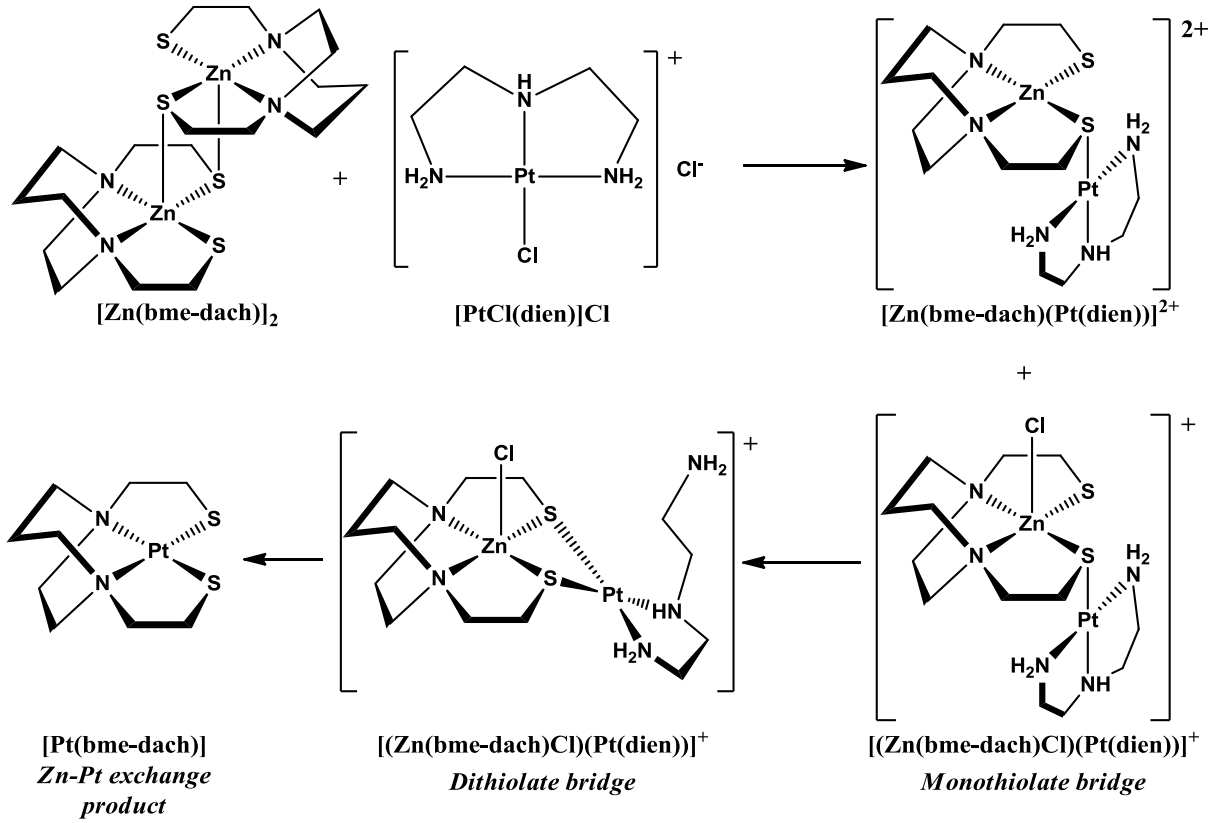

Figure 2.5. Reaction between C_2H_2-type model compound with $[PtCl(dien)]^+$. Binuclear complexes and metal exchange complexes are produce from the interaction.

In bioinorganic chemistry, model compounds that mimic metal environment in protein are an indispensible tool for elucidation of structure, function and reactivity of metal centers.[26] During the mass spectrometry study of the interaction of $[PtCl(dien)]^+$ with a zinc finger model compound $[Zn(bme\text{-}dach)]_2$ (Figure 2.5), in addition to the $[Zn(bme\text{-}dach)(Pt(dien))]^{2+}$ adduct, a species with the mass-to-charge ratio corresponding to $[(Zn(bme\text{-}dach)Cl)(Pt(dien))]^+$ was observed.[61] The same species was isolated from the reaction and characterized using X-ray crystallography that shows Pt^{2+} bound through a sulfur bridging to the Zn^{2+} and the Cl^- bound to the Zn^{2+}. The presence of the intermediate monothiolate bridge adduct was confirmed using Pt NMR but it was not isolated.

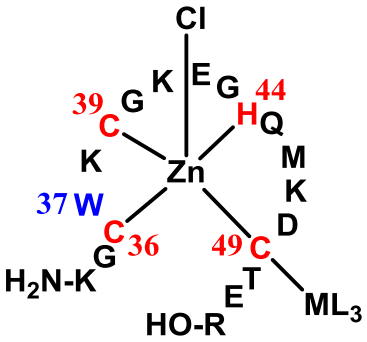

Figure 2.6. Proposed pentacoordination at C-terminal NCp7 zinc finger on reaction with electrophilic metal complexes. ML_3 is the electrophilic metal complex.

Later, in mass spectrometric studies of $[PtCl(dien)]^+$ with a C-terminal NCp7 zinc finger, a similar 1:1 adduct of ZF:$[PtCl(dien)]^+$ was observed.[60] In analogy with the product observed in the model compound studies, a five coordinate zinc was proposed. The structure of this adduct is speculated as the monofunctional Pt bound to the ZF through a bridging thiolate, while the labile Cl^- is the fifth ligand to zinc (Figure 2.6). The pentacoordination observed around zinc in these experiments raises an important question: are the structural zinc motifs found in the proteins susceptible to modification in their coordination sphere? Although the pentacoordinate zinc is observed by mass spectrometry, it is not isolable. Hence, other ways of investigating this speculation are essential.

2.5. Objective

The central objective of this study is to explore the possibility of coordination sphere expansion in structural zinc sites in proteins using computational models. Electronic structure based methods that would provide structural evidence and insights about the nature of such species will be used for the study.

3. Theory: Essentials of Electronic Structure Methods

Computational methods for solving molecular problems range from highly parameterized methods such as molecular mechanics (MM) to pure wave function based methods known as *ab initio* (meaning "from the beginning") methods.[62] Each of these methods is well suited to address a specific kind of problem depending on the size of the system, required accuracy and in case of parameterized methods, the resemblance to the model system used for the purpose. Hence, defining the problem to be solved often narrows down the methods that are applicable. Since the problems addressed in this study involve prediction of unknown structures of transition metal complexes, the choice is restricted to electronic structure based methods – especially *ab initio*.

3.1. Solving the Schrödinger Equation

The only reliable way to obtain the electronic configuration of a system at a particular state is through quantum mechanics by solving the Schrödinger equation. For a single electron system such as a H atom or H_2^+ ion the Schrödinger equation can be solved analytically. Nevertheless, analytical solution for systems with more than one electron is impractical and so several approximations are used to solve the problem numerically to obtain an agreeable solution.[63]

3.1.1. Born-Oppenheimer Approximation

Since the nuclei of an atom is at the minimum ~2000 times heavier than the electrons, it can be consider to be stationary compared to the electrons. This is the Born-Oppenheimer approximation[64] which helps to simplify the Schrödinger equation by decoupling the nuclear and electronic parts. Applying this approximation, the Schrödinger equation[65] for a molecule is given by:

$$(\hat{T} + \hat{V} + \hat{U})\Psi(r_1, r_2 \ldots, r_n) = E\Psi(r_1, r_2 \ldots, r_n), \tag{3.1}$$

where $\hat{T}$ is the kinetic energy operator,

$$\hat{T} = -\frac{\hbar^2}{2m}\sum_{i}^{N} \nabla_i^2 \tag{3.2}$$

$\hat{V}$ is the Coulomb potential from the nuclei,

$$\hat{V} = \sum_{ik} \frac{Z_k}{|r_i - R_k|} \tag{3.3}$$

$\hat{U}$ is the electron-electron interaction term,

$$\hat{U} = \sum_{i<j} \frac{q^2}{|r_i - r_j|} \tag{3.4}$$

$\Psi(r_1, r_2 \ldots, r_n)$ is the many-body antisymmetric wave function, E is the energy of the system at the given state. N is the number of electrons, r_i is the position of the electron i, m is the mass of the electron, Z_k is the charge of the nucleus at R_k and q is the charge of the electron.

3.1.2 Variational Theorem

Definition of the wave function that describes the state of a system again needs to be approximated. According to the variational principle, the ground state wave function of system Ψ_0 has the lowest energy eigenvalue, E_0 compared to a state defined by any other Ψ.[66] Thus, a guess wave function with a number of parameters can be used and tuned iteratively to attain the minimum energy. For any initial guess wave function the following is true:

$$E[\Psi] \leq \frac{\langle \Psi | \widehat{H} | \Psi \rangle}{\langle \Psi | \Psi \rangle} \tag{3.5}$$

3.1.3. Hartree-Fock (HF) Approximation

The electron-electron repulsion term in Eq. 3.4 is still too complicated to be solved. This was simplified by the first approximation introduced by Hartree.[67] Here, the many electron Schrödinger equation is split into a product of one-electron equations and each electron interacting with an average field of all other electrons. This is known as the mean field approximation. Hence the electron-electron interaction term in Eq. 3.4 can be replaced by U^{el}, the Hartree energy:

$$U^{el} = \sum_i \int dr' \frac{|\Psi_i(r_i)|^2}{|r_i - r'|} \tag{3.6}$$

Further, the many electron wave function can be written as a product of one electron wave functions:

$$\Psi(r_1, r_2 \ldots, r_n) = \psi_1(r_1)\psi_2(r_2) \ldots \psi_N(r_N) \tag{3.7}$$

Making the wave function to be anitsymmetric with respect to interchanging electrons as required by Pauli exclusion principle, results in a wave function that can be written in the form of a Slater determinant.[68]

$$\Psi_{HF} = \frac{1}{\sqrt{\mathrm{N}!}} \begin{vmatrix} \psi_1(r_1) & \psi_2(r_1) & \dots & \psi_{\mathrm{N}}(r_1) \\ \psi_1(r_2) & \psi_2(r_2) & \dots & \psi_{\mathrm{N}}(r_2) \\ \vdots & \vdots & & \vdots \\ \psi_1(r_N) & \psi_2(r_N) & \dots & \psi_{\mathrm{N}}(r_{\mathrm{N}}) \end{vmatrix} \tag{3.8}$$

The one-electron wave functions ψ_i are constructed in such a way that they are orthonormal. Furhter, these are one-electron wave functions given as the product of spatial orbital and a spin function (α or β). The HF wave function is restricted to a single Slater determinant which means that electron correlation is only considered as an average effect, thus ignoring explicit repulsions. Solving for energy from the Schrödinger equations using the ψ_i in Slater determinant for the wave functions and summing up all yields the HF energy;

$$\begin{aligned} E_{HF} = & \int \psi_i^*(r_i)\left(\hat{T} + \hat{V}\right)\psi_i(r_i)d^3r \\ & + \frac{1}{2}\sum_{i,j,i\neq j} \int\int \frac{\psi_i^*(r_i)\psi_i(r_i)\psi_j^*(r')\psi_j(r')}{|r_i - r'|} d^3\, r_i d^3 r' \\ & - \frac{1}{2}\sum_{i,j,i\neq j} \delta_{s_i s_j} \int\int \frac{\psi_i^*(r_i)\psi_j(r_i)\psi_i(r')\psi_j^*(r')}{|r_i - r'|} d^3 r_i d^3 r' \end{aligned} \tag{3.9}$$

The second term is the Hartree energy described previously Eq. 3.6 and the third term is the exchange energy which is zero when $s_i \neq s_j$. The above equation leads to the Hartree-Fock equations:

$$\left(\hat{T} + \hat{V} + U^{el}\right)\psi_i(r_i) - \sum_i \int \frac{\psi_j(r_i)\psi_j^*(r')}{|r_i - r'|}\psi_i(r')dr' = \epsilon_i\psi_i(r_i) \tag{3.10}$$

The solution of these equations gives a set of spin orbitals and their energies. These equations can be solved numerically by integration over a grid but the exchange energy term makes it complex.[63,69] Hence, a linear combination of atom centered, hydrogen-like orbitals are used as basis functions to the produce a trial wave function. Thus, the wave functions in Slater determinant can be expanded as:

$$\psi_i(r) = \sum_{pk} C_{pk}\chi_p\,(r) \tag{3.11}$$

From the trial wave function, the 'true' wave function can be obtained by applying the variational method and changing the orbital coefficients. However, each orbital is dependent on all other orbitals and the problem should be solved iteratively until the orbital energies and their coefficients remain constant for two consecutive iterations. This is known as self-consistent field procedure.

The assumption that the wave function can be described by a single Slater determinant implies that movement of electrons is not correlated as it is in a real system. Therefore, the HF energy is always higher than the ground state energy. The missing correlation energy is given by,

$$E_{\text{corr}} = E_0 - E_{HF} \tag{3.12}$$

Nevertheless, HF forms the basis for several other methods available today. The post Hartree-Fock methods such as configuration Interaction (CI), coupled cluster (CC) and Møller-Plesset perturbation theory (MP), aim to account for electron correlation by mixing a linear combination of excited state Slater determinants. These methods provide higher accuracy, but they are

computationally demanding. An alternative to these correlated wave function methods is a greatly simplified method known as density functional theory.

3.1.4. Density Functional Theory

Density functional theory (DFT) has become the most widely used method for electronic structure calculation of complex chemical systems. This huge success is attributed to the conceptual simplicity and computational efficiency.[70] Compared to most *ab initio* methods that are wave function based, DFT treats electron density, $\rho(r)$, as its fundamental quantity. DFT preserves the mean-field approach used in HF except that here a set of non interacting, one-electron spin-orbitals are used to construct the ground state spin density.[66,69] This largely simplifies the solution for many electron systems by defining the system based on three dimensional electron density rather than the use of 3N dimensional wave functions. The advantage of DFT over traditional wave function methods becomes apparent for larger systems (> 10 heavy atoms) where DFT offers accuracy comparable to correlated wave function methods at a much lower computational cost.[71]

DFT is built on the Hohenberg-Kohn theorem[72] that states, "the ground state electron density, $\rho(r)$ uniquely determines the external potential $v(r)$." In case of molecules, the $v(r)$ is the Coulomb potential due to the nuclei. As usually the electron density is deduced from the potential it is experiencing, this theorem reverses it. Thus, if the ground state electron density is known, the external potential that influences it can be deduced. In other words $v(r)$ is a functional of $\rho(r)$. Similarly, the number of electrons N, the full Hamiltonian, the wave function Ψ, and the total energy can all be given as functionals of $\rho(r)$. Using this theorem energy can be given as a functional of $\rho(r)$:

$$E_v[\rho(r)] \equiv \int v(r)\rho(r)dr + F[\rho(r)] \tag{3.13}$$

where,

$$F[\rho(r)] \equiv \left(\Psi[\rho(r)]\left(\hat{T} + \hat{U}\right)\Psi[\rho(r)]\right) \tag{3.14}$$

$F[\rho(r)]$ is defined as a universal function, valid for any N and any $v(r)$. The minimal principle is,

$$E_v[\rho(r)] \geq E_v[\rho_0(r)] \equiv E \tag{3.15}$$

where $\rho_0(r)$ and E are the electron density and energy of the ground state. The above equality hold only if $\rho(r) = \rho_0(r)$.

$F[\rho(r)]$ can be further split as,

$$F[\rho(r)] = T_s[\rho(r)] + \frac{1}{2}\int \frac{\rho(r)\rho(r')}{|r - r'|}drdr' + E_{xc}[\rho(r)] \tag{3.16}$$

where $T_s[\rho(r)]$ is the non-interacting kinetic energy, the second term is the Hartree energy in terms of electron density. $F[\rho(r)]$ has a large contribution from these two terms and a small contribution from E_{xc}, which is defined as the exchange correlation energy. However the kinetic energy calculated as a functional of electron density yielded poor results. Hence Kohn and Sham[73] suggested that $T_s[\rho(r)]$ be evaluated from single particle wave function which is used to construct the electron density. Thus the Kohn-Sham (KS) model resembles HF to a large extent with comparable results. Now the only unknown term, E_{xc}, needs to be approximated. From the energy expression in Eq. 3.13, a set of KS equations can be constructed similar to HF equations:

$$\left(T_s + v(r)\right)\psi_i(r) - \int \frac{\rho(r)}{|r_i - r'|}\psi_i(r)dr' + v_{xc}(r) = \epsilon_i\psi_i(r) \tag{3.17}$$

where,

$$\rho(r) = \sum_{i}^{occ} |\psi_i(r)|^2 \tag{3.18}$$

$$N = \int \rho(r) d^3 r \tag{3.19}$$

and $v_{xc}(r)$, the exchange correlation potential is

$$v_{xc}(r) = \frac{\delta E_{xc}[\rho(r)]}{\delta n(r)} \tag{3.20}$$

As the KS orbitals are an approximation to the exact density, except the energy of the HOMO, the other orbitals and energies do not have strict physical significance.[70] The E_{xc} is the sum of errors incurred in the theory due to approximations such as assuming the kinetic energy as non-interacting and treating the electron-electron term classically. Although trivial in its contribution, this term makes the KS model formally exact and includes the many-body effects which HF does not. It is known that E_{xc} is a functional of electron density but the exact functional is unknown. Several methods have been developed to approximate for the exchange-correlation functional, which resulted in a range of DFT methods to choose from. The knowledge of the nature of these approximations would help making better decision while choosing an appropriate DFT method.

3.2. Exchange-Correlation Functionals

3.2.1. Local Desnity Approximation

The most basic approximation that leads to good improvement over HF method is the local density approximation (LDA) proposed by Kohn and Sham.[73] This stems from a predecessor of modern DFT, the Thomas-Fermi-Dirac[74] model that assumed a homogeneous electron gas in an external potential. In this model, the kinetic and exchange energy are expressed in terms of local density. This suggests that local exchange-correlation energy per electron can be approximated as a function of local charge density. The exchange-correlation functional takes the form,

$$E_{xc}^{LDA}[\rho(r)] = \int \epsilon_{xc}(\rho(r))\rho(r) d\, r \tag{3.21}$$

where ϵ_{xc} is a function of local density only. ϵ_{xc} can be further separated into an exchange part and a correlation part as,

$$\epsilon_{xc}(\rho(r)) = \epsilon_x(\rho(r)) + \epsilon_c(\rho(r)) \tag{3.22}$$

and the exchange energy for a homogeneous electron gas is given by the Dirac formula.

$$\epsilon_x\big(\rho(r)\big) = -C_x\rho^{1/3} \tag{3.23}$$

The exact form of correlation energy is known only for high and low density limits. The correlation energies for intermediate densities have been simulated using quantum Monte Carlo methods.[69] Various analytical forms have been used to fit these results to produce different LDAs. The spin-dependent form of LDA is termed local spin-density approximation (LSDA).

Despite its simplicity, LDA is known to perform remarkably well with an accuracy similar to HF methods. This is especially true for band structure and local energy calculations in

solid-state physics. However the inadequateness of LDA/LSDA is apparent in molecular systems, where it is known to overestimate bond strengths.[71] The assumed homogeneity in electron cloud is apparently the limitation, since real charge density is inhomogeneous. Some often used LSDA are VWN (Vosko, Wilk and Nusair)[75] and PW92 (Perdew and Wang in 92).[76]

3.2.2. Generalized Gradient Approximation

The next obvious improvement over LSDA was to include a local spin-density gradient. Including just first order gradient correction results in an approximation that does not obey certain conditions.[69,71] In the generalized gradient approximation, a functional that obeys all conditions is chosen and the functional is of the form,

$$E_{xc}^{GGA}[\rho(r)] \approx \int \epsilon_{xc}(\rho(r), \nabla\rho(r))\rho(r)d\,r \tag{3.24}$$

GGA offers significant improvement over LDA for most cases, including better bond length and binding energy of molecules. This led the adoption of DFT in the field of chemistry. Some popular GGAs include, BP86 (B stands for Becke's 1988 exchange functional[77] and P86 stands for Perdew's 1986 correlation functional[78]), BLYP (LYP stands for Lee-Yang-Parr),[79] PW91(Perdew and Wang in 1991)[80] and PBE (Perdew, Burke and Ernzerhof)[81] and mPWPW(modified Perdew-Wang functional of Adamo and Barone),[82] which is very similar to PBE. GGAs can be formed by combining an exchange functional from one source with a correlation functional from another.

3.2.3. Hybrid GGA

Both LSDA and GGA functionals include the self-interaction error,[69] while HF is free of it. Thus, further improvement in E_{xc} can be obtained by mixing a fraction of HF exchange into

the DFT exchange functional, which may decrease or eliminate self-interaction.[69,70] The general form of the hybrid functional is:

$$E_{xc}^{Hybrid} = aE_{xc}^{GGA} + bE_{x}^{Exact} \tag{3.25}$$

Depending on the choice of GGA exchange-correlation functionals, the parameters that determine the weight of each functional is obtained by fitting the outcome of the combinations to accurately known results. B3LYP is a commonly used hybrid functional. Here, B3 denotes Beckee's three parameters which are used to weigh the functionals used. In this functional, 20% HF exchange energy is mixed with the DFT exchange-correlation functional.[83] Other popular hybrid functionals include B3PW91, mPW1PW[82] and PBE1PBE (also called PBE0).[84] The latter two functionals use only one parameter to define the amount of HF exchange mixing, thus are considered parameter free.

3.3. Basis Functions

In most electronic structure calculations, the complex wave function or the electron density function is represented as a linear combination of a set of simpler basis functions. This makes it easier for computation. However, the accurate reproduction of the original function would require an infinite number of basis functions. Since this is impossible, a finite number of basis functions are used to produce an approximate representation of the 'real' function. Hence, the type and number of the basis function used in the approximation affects the accuracy of the computational result.

These functions are named orbitals because they are combined to mimic atomic orbitals of hydrogen, for which the exact solutions are known. One of these functions, known as Slater type orbitals (STO)[85] is given by:

$$\chi_{\zeta,n,l,m}(r,\theta,\varphi) = NY_{l,m}(\theta,\varphi)r^{n-1}e^{-\zeta r} \tag{3.26}$$

where N is the normalization constant and $Y_{l,m}$ represents spherical harmonic functions that define the angular part of the orbitals. The exponential form of this function resembles the electron distribution from the nucleus to any distance. The nodes present in the radial part of hydrogen-like atomic orbitals are produced by linear combination of STOs. Thus, STOs can be made to closely match the required atomic orbital. However, for larger systems the integrals of these functions are expensive.

The other type of function used for this purpose is Gaussian type. The general form of Gaussian type orbitals (GTO)[86] can be written as:

$$\chi_{\zeta,n,l,m}(r,\theta,\varphi) = NY_{l,m}(\theta,\varphi)r^{2n-2-l}e^{-\zeta r^2} \tag{3.27}$$

The r^2 dependence in the exponential of GTOs makes them poorer in representing the distribution of electrons around the nucleus and the way it falls off moving away from the nucleus. Hence, more GTOs need to be used to produce accuracies comparable to STOs. However, the ease of computation using GTOs makes them preferable to STOs. At the minimum, a combination of three GTOs is required to closely reproduce the same orbital formed by a single STO. The orbitals thus formed are known as contracted Gaussian type orbitals. Thus, a number of primitive Gaussian type orbitals (PGTO) are combined together to form a single contracted Gaussian type orbital (CGTO). This is represented as:

$$\chi(\text{CTGO}) = \sum_i c_i \chi_i(\text{PGTO}) \tag{3.28}$$

where c_i is the contraction coefficient for the function χ_i. A minimal basis of an atom contains one (C)GTO for each of its core and valence orbitals. As an example, for carbon a minimal basis

is represented by two s-functions (1s and 2s) and a set of p-functions. Minimal basis is not flexible enough to represent the changes and polarization in molecules. Hence, each orbital is described with 2 or more functions. The resulting basis is termed an *n*-tuple-ζ basis function (e.g. double-zeta, triple-zeta, etc.). A set of such basis functions defined for a group of elements is called a basis set.

3.3.1. Pople Basis Sets

It is the valence orbitals that take part in chemical bonding, while the core electrons for the most part remain unaffected. Thus, the core orbitals do not need much flexibility. Therefore it is reasonable to represent the core orbitals with just one contracted basis function, while the valence orbitals are represented by multiple basis functions, as this still allows the enough flexibility required to represent the chemical bond. The split valence basis sets designed by Pople group are one among the widely used basis sets.[87] As an example, consider 6-31G, the '6' here denotes 6 PGTOs used to represent the core orbitals, while '31' represents a set of two basis functions used to represent the valence orbitals, the first one made of 3 PGTO and the second a single PGTO. Similarly, 6-311G stands for a triple-zeta split valence basis set. As a double-zeta basis set is better than a single-zeta basis set, so is a triple-zeta better than a double zeta. However, when considering increasing the quality of a basis function, adding polarization functions should take the priority over increasing the number of basis functions.

3.3.2. Augmenting Basis Functions

Polarization functions add more flexibility to an orbital. This is done by adding a higher angular momentum orbital to the current orbital. For example, adding d-functions to a p-orbital improves its polarizability. Just increasing the number of basis function without adding

polarization does not lead to improved results. The number and type of these functions can be varied as required. Another consideration is to add diffuse functions to represent loosely bound electrons. This is especially important for proper representation anions or excited states.

3.3.3. Effective Core Potential

For heavier atoms with large atomic numbers, the core electrons that constitute a large part of their electronic structure do not participate in bonding, but add to the computational cost when using full basis set. In addition, relativistic effects come into play in these atoms that need to be accounted for. The solution is to model an effective core potential (ECP) including relativistic effects to substitute the core electrons. When using ECP, the gain in computational efficiency and the advantage of built in relativistic effects are visible in cases of large atoms down the periodic table.

4. Modeling of Coordination Sphere Expansion in Structural Zinc Sites Using DFT

The primary objective of this study is to investigate the possibility of Zn^{2+} at structural sites undergoing coordination sphere expansion due to perturbation of its pre-bound ligands by electrophilic Pt compounds. Structural insight of these bimetallic complexes is sought after to understand the chemistry involved in the process. These species were observed in NMR and mass spectrometric studies but were not isolable due to the complex nature of the model system involved.[60,61] Hence, it is appropriate to investigate these species using electronic structure based computational models. The organometallic nature of the species involved requires the use of a correlated wave function theory methods or DFT to address the problem. The size of the system under study at the minimum would involve more than 20 heavy atoms. Among the two, DFT is preferred as it is economical with accuracy comparable to correlated wave function based methods.

4.1. Choice of DFT Method

The applicability of DFT is largely determined by the method in which the exchange-correlation functional is approximated. Clearly GGA and hybrid GGA or those that include other corrections are better than LSDA for molecular structure. Further, to narrow down the choice from the myriad of available functionals, suggestions from previous studies for transition metal containing systems were considered.[70,88,89] Seven functionals which consistently performed

better were chosen based on these studies for further benchmarking. The chosen functionals are G96LYP,[90] PBE, B3LYP, mPWLYP1M,[88] PBE0, B3PW91 and mPW1PW91. Out of these, the first two are GGAs and the rest are hybrid GGAs. Benchmarking of these DFT functionals against experimental results was the logical next step to find the best among these functional.

4.2. Benchmarking of DFT Methods

The most convincing choice can be made by comparing the performance of DFT functionals to experimental results. The closer the experimentally known system resembles the computational model, the more reliable would be the results. Luckily, in this case, there exists X-ray crystal data for the dithiolate bridged pentacoordinate zinc complex, $[(Zn(bme\text{-}dach)Cl)(PtCl(dien))]^+$ (**I**) (Figure 4.1). Hence, the performance of the DFT functionals can be accessed based on the structural parameters (Table 4.1) of this complex.

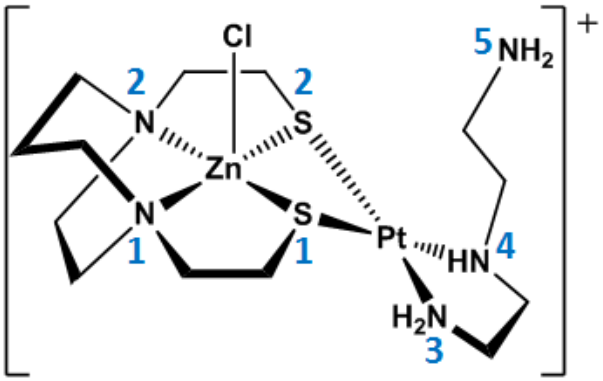

Figure 4.1. Dithiolate bridged (Zn,Pt) bimetallic compound with zinc in pentacoordinate state, isolated from reaction between $[Zn(bme\text{-}dach)_2]$ and $[PtCl(dien)]^+$. The numbering for the ligating atoms to be followed is shown.

Table 4.1. Structural parameters of dithiolate bridged (Zn,Pt) bimetallic compound taken from X-ray crystal structure.

Bond lengths (Å)		Bond angles (deg)	
Zn-N(1)	2.148	∠N(1)-Zn-N(2)	75.1
Zn-N(2)	2.167	∠S(1)-Zn-S(2)	82.3
Zn-S(1)	2.457	∠S(1)Zn-N(1)	84.6
Zn-S(2)	2.421	∠S(1)-Zn-N(2)	85.5
Zn-Cl	2.258	∠S(2)-Zn-N(1)	136.2
Pt-S(1)	2.308	∠S(2)-Zn-N(2)	135.1
Pt-S(2)	2.311	∠Cl-Zn-N(1)	109.0
Pt-N(3)	2.069	∠Cl-Zn-N(2)	108.6
Pt-N(4)	2.103	∠Cl-Zn-S(1)	115.8
		∠Cl-Zn-S(2)	114.3
		∠S(1)-Pt-S(2)	88.0
		∠S(1)-Pt-N(3)	94.1
		∠S(2)-Pt-N(4)	95.4
		∠N(3)-Pt-N(4)	82.5

The geometry around Zn^{2+} in the X-ray crystal structure can be view as distorted trigonal bipyramidal, with the trigonal plane being formed by N(1)-S(2)-Cl or N(2)-S(1)-Cl, since it is almost symmetric. In synthetic models[26,91-98] and in proteins[99] Zn-S bonds range from 2.2 – 2.5 Å and Zn-N bonds range from 2.0 – 2.3 Å. As can be seen, there is a huge variation in these observed bond lengths. In synthetic compounds[93-98] with $ZnCl_4$ or with a ligand environment similar to the one under study, Zn-Cl bond lengths of 2.24 – 2.34 Å have been reported. In comparison to these values, the Zn-S bond lengths are towards the upper limit for **I**. This can be rationalized as due to sharing of the thiolate ligands with Pt. However, the Pt-S bonds are much closer to the normal value.[61] The Zn-N bonds are a bit elongated too; this is probably due to steric constraints in the bme-dach ligand since the same trend is observed in the zinc finger

model compound, [Zn(bme-dach)$_2$]. The Zn-Cl bond length is well within the normal range of values.

4.2.1. Basis Set and Software

For all the calculations, Pople split-valence basis set was used on Zn, C, H, N, S and Cl. The quality of the basis set is varied, as will be mentioned. Polarization functions and diffuse functions are also varied and will be indicated. The Lanl2DZ basis set was used for Pt with ECP. All calculations were performed using the Gaussian03[100] suite of programs.

4.2.2. Benchmarking of DFT Functionals

To begin, the performance of the selected functionals were tested with the 6-311G++(d,p) basis set. The performance of the functionals was compared using select bond lengths and bond angles as in Table 4.2. The primary focus here is the geometry and bonding parameters of zinc.

Table 4.2. Comparison of performance of select DFT methods using 6-311++G(d,p) basis set with experimental values.

Bond lengths (Å)

Method	Zn-Cl	Zn-S(1)	Zn-S(2)	Zn-N(1)	Zn-N(2)	Pt-S(1)	Pt-S(2)	Pt-N(3)	Pt-N(4)
Experimental	2.258	2.457	2.421	2.148	2.167	2.308	2.311	2.069	2.103
B3LYP/6-311++g(d,p)	2.220	2.500	2.497	2.256	2.256	2.368	2.369	2.151	2.187
G96LYP/6-311++g(d,p)	2.236	2.503	2.508	2.274	2.267	2.379	2.380	2.169	2.208
MPWLYP1M/6-311++(d,p)	2.231	2.519	2.514	2.278	2.277	2.383	2.383	2.172	2.211
B3PW91/6-311++(d,p)	2.206	2.473	2.472	2.228	2.229	2.344	2.344	2.128	2.159
mPW1PW91/6-311++(d,p)	2.202	2.469	2.467	2.220	2.222	2.339	2.339	2.120	2.150
PBE/6-311++(d,p)	2.202	2.469	2.467	2.220	2.222	2.339	2.339	2.120	2.150
PBE0/6-311++(d,p)	2.201	2.468	2.465	2.219	2.222	2.336	2.336	2.117	2.147

Table 4.2. (continued) Comparison of performance of select DFT methods using 6-311++G(d,p) basis set with experimental values.

Bond angles (deg)

Method	N(1)-Zn-N(2)	S(1)-Zn-S(2)	N(1)-Zn-S(1)	N(2)-Zn-S(2)	Cl-Zn-N(1)	Cl-Zn-N(2)	Cl-Zn-S(1)	Cl-Zn-S(2)
Experimental	75.1	82.3	84.6	85.5	109.0	108.6	115.8	114.3
B3LYP/6-311++g(d,p)	72.5	81.9	84.5	84.6	109.9	109.8	116.8	116.5
G96LYP/6-311++g(d,p)	72.3	82.5	85.3	85.6	110.2	110.6	114.8	114.5
MPWLYP1M/6-311++(d,p)	72.2	81.9	84.6	84.7	109.8	109.8	116.8	116.5
B3PW91/6-311++(d,p)	73.0	81.8	84.7	84.8	109.7	109.5	116.6	116.3
mPW1PW91/6-311++(d,p)	73.0	81.8	84.6	84.6	109.5	109.2	116.9	116.6
PBE/6-311++(d,p)	72.8	81.8	85.0	85.0	109.2	109.0	116.8	116.4
PBE0/6-311++(d,p)	73.0	81.7	84.5	84.5	109.3	109.0	117.3	116.9

In Table 4.2 the DFT methods are grouped according to the correlation functionals they use: LYP, PW91 or PBE. The difference in performance is more apparent in the bond lengths than in the bond angles. The trend that is clearly seen is that the performance of PW91 and PBE are better compared to LYP correlation functional. Thus, the commonly used B3LYP functional is not suitable to describe the system under study. Similarly, G96LYP and MPWLYP1M that were reported to be the first two among the better performing functionals failed in this case.[88] In the cases of functionals using LYP, the Zn-S bonds are longer by an average of 0.06 Å and the Zn-N bonds are also longer by an average of 0.11 Å. These are huge deviations for DFT methods where an accuracy of 0.02 Å can be reached. The Pt-S and Pt-N bonds are predicted to be longer too. It is only the Zn-Cl bond where these functionals performed better compared to the functionals using PW91 or the closely resembling PBE correlation functional. The effect from variation of exchange functionals among these studied methods is not huge as seen by comparing B3LYP, G96LYP and MPWLYP1M. Comparing PBE and PBE0 it can be said that there is only a little gain in performance of hybrid GGA compared to GGA as the difference in these is only in the exchange part of the functionals.

Among the better performing B3PW91, mPW1PW91 and PBE0 functionals, the latter two that share a resemblance in their basic functional form are the best. Although the bond distances predicted by these methods are still not close enough to a satisfactory accuracy, they are certainly better. The Zn-S bond lengths are better compared to the Zn-N bond lengths. The Pt-S and Pt-N bond lengths are also closer to the experimental values. However the Zn-Cl bond is predicted to be shorter by these methods. Further improvement is possible by using extra polarization functions or by using a mixed basis on various atoms. In the following discussions,

the bond lengths will only be used, as the bond angles only vary within an agreeable degree and not much insight is gained from them.

4.2.3. Mixing and benchmarking of Basis Functions

The other essential part of a DFT calculation that can be improved is the basis set. In order to assess the effect of variation in quality of the basis function, the DFT functional will be fixed while effects from changes in the basis function will be tested systematically. B3LYP was chosen for this purpose as the deviation from experimental data was among the largest for this functional. Thus, any change in performance could be tracked easily through comparison. At first the effect of increasing the number of basis functions and adding diffuse functions will be tested. For this purpose, 6-31G(d,p), 6-311G(d,p) and the same with added diffuse functions on all atoms were compared.

Table 4.3. Comparison of double-zeta and triple-zeta basis functions with and without diffuse functions. Optimized bond lengths (Å) for model **I** using B3LYP are shown.

Method	Zn-Cl	Zn-S(1)	Zn-S(2)	Zn-N(1)	Zn-N(2)	Pt-S(1)	Pt-S(2)	Pt-N(3)	Pt-N(4)
Experimental	2.258	2.457	2.421	2.148	2.167	2.308	2.311	2.069	2.103
B3LYP/6-31g(d,p)	2.222	2.529	2.522	2.176	2.178	2.364	2.364	2.149	2.187
B3LYP/6-31++g(d,p)	2.221	2.505	2.499	2.246	2.246	2.367	2.367	2.151	2.189
B3LYP/6-311g(d,p)	2.242	2.522	2.518	2.197	2.195	2.370	2.366	2.147	2.179
B3LYP/6-311++g(d,p)	2.220	2.500	2.497	2.256	2.256	2.368	2.369	2.151	2.187

Comparing the double-zeta basis function with the triple-zeta here, both with just basic polarization, in the absence of diffuse functions, just increasing the number of basis functions seems to worsen the quality of the results (Table 4.3). However inclusion of diffuse functions counteracts the effect in most bonds. A trend that is apparent is that the Zn-S bonds are improved

by adding diffuse functions while Zn-N bond distances are worsened. Hence, the next logical step was to vary the diffuse functions on some atom types to see the effect it has on the quality of the geometry of model **I**.

Diffuse functions are necessary to describe systems with loosely bound electrons. The complex as a whole is positively charged but the S and Cl ligands are anionic. These ligands are softer and hence require diffuse functions; however, this may not be true in the case of the other atoms. Especially Zn^{2+} would not require diffuse functions for its orbitals to be described properly. This may be true in case of nitrogen too, which is classified as an intermediate base. The trends observed in the above experiment suggest the same. Hence, mixed basis functions were tested with diffuse function only on anionic ligands. In addition, from the above result it can be inferred that double-zeta quality basis set is comparable to a triple-zeta basis. Hence only Zn and the ligating atoms were treated with 6-311G basis while 6-31G was used for C and H. Basic polarization was added on all atoms.

Table 4.4. Comparison of mixed basis functions with diffuse functions only on anionic ligands. Optimized bond lengths (Å) for model **I** using B3LYP are shown.

Method	Zn-Cl	Zn-S(1)	Zn-S(2)	Zn-N(1)	Zn-N(2)	Pt-S(1)	Pt-S(2)	Pt-N(3)	Pt-N(4)
Experimental	2.258	2.457	2.421	2.148	2.167	2.308	2.311	2.069	2.103
B3LYP/6-311++g(d,p)	2.220	2.500	2.497	2.256	2.256	2.368	2.369	2.151	2.187
B3LYP/mixBasis1	2.234	2.515	2.511	2.200	2.201	2.366	2.365	2.152	2.185

mixBasis1 – C, H: 6-31g(d,p); N, Zn: 6-311g(d); S, Cl: 6-311+(d)

As seen from Table 4.4 avoiding the use of diffuse functions on N and Zn improves Zn-N and Zn-Cl bond distances. Nevertheless, the Pt-N bond distances are not affected by this change and the effect arises from the combined improvement on Zn and N. Further, since the geometry of Zn^{2+} and its ligand is complex, including more polarization functions might result in better bonding. Therefore, the effect of including polarization on various atoms was investigated next.

Table 4.5. Comparison of the effect of higher order polarization functions on various atoms. Optimized bond lengths (Å) for model **I** using B3LYP are shown.

Method	Zn-Cl	Zn-S(1)	Zn-S(2)	Zn-N(1)	Zn-N(2)	Pt-S(1)	Pt-S(2)	Pt-N(3)	Pt-N(4)
Experimental	2.258	2.457	2.421	2.148	2.167	2.308	2.311	2.069	2.103
B3LYP/6-311++g(d,p)	2.220	2.500	2.497	2.256	2.256	2.368	2.369	2.151	2.187
B3LYP/mixBasis1	2.234	2.515	2.511	2.200	2.201	2.366	2.365	2.152	2.185
B3LYP/mixBasis2	2.230	2.516	2.511	2.197	2.198	2.365	2.365	2.152	2.185
B3LYP/mixBasis3	2.209	2.486	2.482	2.212	2.213	2.348	2.347	2.162	2.195
B3LYP/mixBasis4	2.244	2.464	2.457	2.199	2.200	2.339	2.339	2.144	2.177
B3LYP/mixBasis5	2.243	2.466	2.460	2.202	2.204	2.338	2.337	2.145	2.178

mixBasis1 – C, H: 6-31g(d,p); N, Zn: 6-311g(d); S, Cl: 6-311+(d)
mixBasis2 – C, H: 6-31g(d,p); N: 6-311g(d); Zn: 6-311g(3df); S, Cl: 6-311+(d)
mixBasis3 – C, H: 6-31g(d,p); N: 6-311g(d); Zn: 6-311g(3df); S, Cl: 6-311+(2d)
mixBasis4 – C, H: 6-31g(d,p); N, Zn: 6-311g(3df); S: 6-311+(3df); Cl: 6-311+(d)
mixBasis5 – C, H: 6-311g(d,p); N, Zn: 6-311g(3df); S: 6-311+(3df); Cl: 6-311+(d)

As an improvement to mixBasis1, the polarization on Zn was increased using 3d and one f type function (mixBasis2). This, however, resulted only in a slight improvement in Zn-N bond distance (Table 4.5). On the other hand, stepping up the polarization on S using just one extra d function (mixBasis3) greatly improves the Zn-S bond. This also results in better Pt-S bond distance. However, the imbalance in polarization on N is seen as an increase in Zn-N bond distance. In mixBasis3 the polarization on Cl was improved by one extra d type function too. This leads to shortening of Zn-Cl bond, which in this case is not desirable. Hence, the polarization on Cl will be reduced back to minimum. In mixBasis4, extra polarization functions are added on Zn, N and S with only basic polarization on Cl. This, overall, gives the best results. Further, improving the quality of basis on C and H to triple-zeta level, the mixed basis function is referred to as mixBasis5, produces very little effect on bonds formed by Zn and Pt.

4.2.4. The Chosen DFT Method

Having improved the basis function to a large extent to suit the needs of the current system used for benchmarking, the final mixed basis was used in combination with the better performing DFT functionals.

Table 4.6. Evaluation of Chosen DFT functionals in combination with optimized mixed basis function. Optimized bond lengths (Å) of model **I** using mixBasis5 and select DFT functionals are given.

Method	Zn-Cl	Zn-S(1)	Zn-S(2)	Zn-N(1)	Zn-N(2)	Pt-S(1)	Pt-S(2)	Pt-N(3)	Pt-N(4)
Experimental	2.258	2.457	2.421	2.148	2.167	2.308	2.311	2.069	2.103
B3LYP/6-311++g(d,p)	2.220	2.500	2.497	2.256	2.256	2.368	2.369	2.151	2.187
B3LYP/mixBasis5	2.243	2.466	2.460	2.202	2.204	2.338	2.337	2.145	2.178
mPW1PW91/6-311++(d,p)	2.202	2.469	2.467	2.220	2.222	2.339	2.339	2.120	2.150
mPW1PW91/mixBasis5	2.224	2.437	2.434	2.172	2.174	2.310	2.309	2.115	2.143
PBE0/6-311++(d,p)	2.201	2.468	2.465	2.219	2.222	2.336	2.336	2.117	2.147
PBE0/mixBasis5	2.223	2.436	2.432	2.171	2.174	2.307	2.306	2.113	2.139

mixBasis5 – C, H: 6-311g(d,p); N, Zn: 6-311g(3df); S: 6-311+(3df); Cl: 6-311+(d)

The improvement produced by using the optimal basis functions defined by mixBasis5 makes the results from mPW1PW91 and PBE0 even better (Table 4.6). The average Zn-S bond distance of 2.439 Å is very close to the experimental average. The Zn-N bond distance is longer by 0.02 Å. The Zn-Cl bond deviates by 0.04 Å, which is acceptable. The geometry around Pt is also improved similarly.

In summary, mPW1PW91 or PBE0 functionals, along with split valence triple-zeta polarized basis function with additional polarization on Zn, N and S and diffuse functions on S and Cl, gives the best results for the bimetallic complex used for benchmarking. Hence, here mPW1PW91/mixBasis5 level of theory will be used to investigate the proposed problem.

4.3. Modeling Mimics of Zinc at Structural Sites

The ligand environment around zinc in structural sites can be mimicked by truncating the amino acid residues to basic ligand units. Thus, histidine is usually modeled as imidazole and cysteine is modeled as thiomethane (Figure 4.1 b).[101,102] This simplification will be adopted here, as it reduces the computational cost and offers the flexibility required for expansion of coordination sphere.

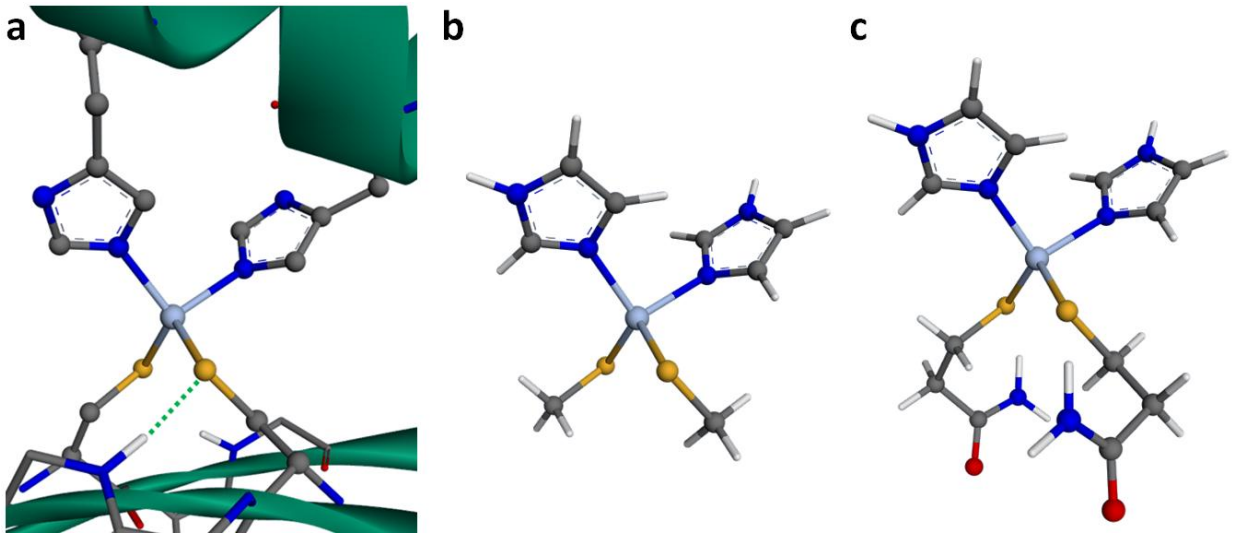

Figure 4.2. Modeling structural zinc sites mimicking protein ligands: a) C_2H_2 type structural zinc site with stabilizing interaction from amide backbone (PDB ID: 2J7J)[28]. b) a minimal model of C_2H_2 type zinc site. c) an improved model of C_2H_2 type zinc site with amide groups which mimic stabilizing interaction in proteins.

However, in protein environments more often the thiolates bound to Zn^{2+} are stabilized by electrostatic interactions from amide hydrogens (Figure 4.1 a).[103] This is an important interaction to include, as these interactions may facilitate the formation of five-coordinate zinc by removing charge density on the sulfur atoms. Hence, these will be model, if required, as 3-sulfanylpropanamide replacing the thiomethane (Figure 4.2 b).

4.4. Results and Discussion

Using the chosen DFT method, the possibilities of structural zinc sites undergoing coordination sphere expansion was explored. All of the following geometry optimizations were performed using mPW1PW91/mixBasis5. Vibrational analysis was performed at the same level to confirm that the resulting structures are global minima. The models studied here are either C_2H_2 type or C_3H type zinc finger mimics. Both the possibilities of dithiolate bridge and monothiolate bridge to Pt are considered.

4.4.1. Monothiolate Bridged intermediate, $[(Zn(bme\text{-}dach)Cl)(Pt(dien))]^+$

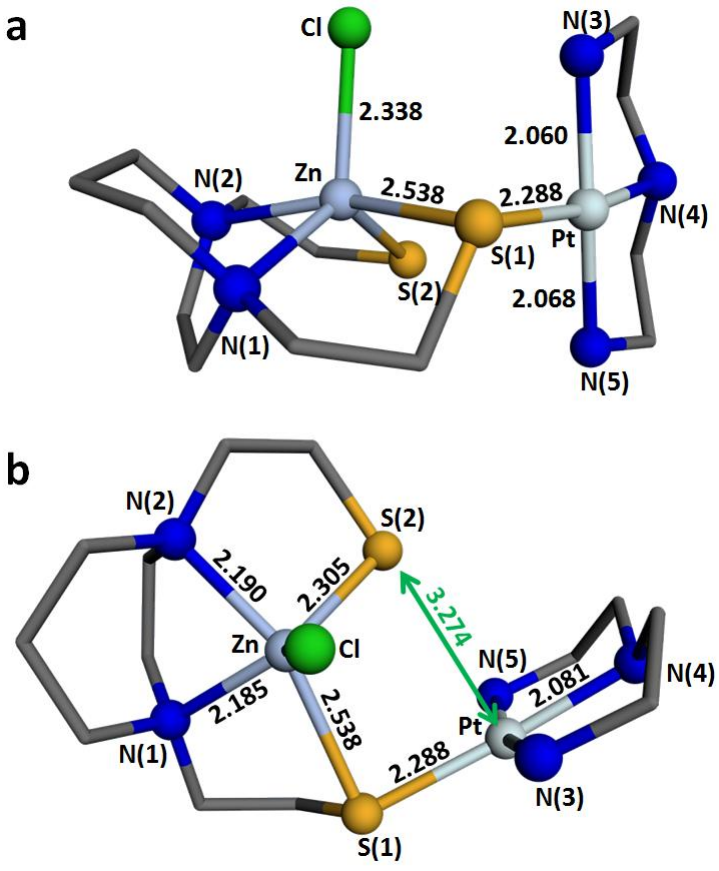

Figure 4.3. Optimized structure of monothiolate bridged $[(Zn(bme\text{-}dach)Cl)(Pt(dien))]^+$. a) side view b) top view. Bond lengths and interatomic distances are in Å.

Table 4.7. Geometric parameters of energy minimized C_2H_2 model complexes. Bond lengths are in Å and bond angles are in deg.

	I	II	III	IV
Zn-N(1)	2.172	2.185	2.101	2.011
Zn-N(2)	2.174	2.190	2.092	2.036
Zn-S(1)	2.437	2.538	2.498	-
Zn-S(2)	2.434	2.305	2.551	2.260
Zn-Cl	2.224	2.338	2.277	2.332
Pt-S(1)	2.310	2.288	2.287	2.285
Pt-S(2)	2.309	-	2.296	-
Pt-N(3)	2.115	2.060	2.116	2.064
Pt-N(4)	2.143	2.081	2.158	2.099
Pt-N(5)	-	2.068	-	2.058
∠N(1)-Zn-N(2)	74.7	74.5	91.8	107.5
∠S(1)-Zn-S(2)	81.5	105.1	77.2	-
∠S(1)Zn-N(1)	85.8	81.5	90.6	-
∠S(1)-Zn-N(2)	136.0	155.8	155.9	-
∠S(2)-Zn-N(1)	136.1	124.0	149.8	109.9
∠S(2)-Zn-N(2)	85.9	86.0	89.0	109.6
∠Cl-Zn-N(1)	109.4	122.3	100.5	101.8
∠Cl-Zn-N(2)	109.2	100.9	103.1	99.6
∠Cl-Zn-S(1)	114.5	94.5	100.0	-
∠Cl-Zn-S(2)	114.2	112.7	108.7	126.9
∠S(1)-Pt-S(2)	87.0	-	86.8	-
∠S(1)-Pt-N(3)	93.9	88.5	91.9	92.0
∠S(1)-Pt-N(5)	-	102.5	-	100.3
∠S(2)-Pt-N(4)	96.8	-	99.8	-
∠N(3)-Pt-N(4)	82.0	84.2	81.5	83.8
∠N(4)-Pt-N(5)	-	84.2	-	84.0

I – $[(Zn(bme\text{-}dach)Cl)(Pt(dien))]^+$ dithiolate bridge; II – $[(Zn(bme\text{-}dach)Cl)(Pt(dien))]^+$ monothiolate bridge
III – $[ZnCl(His)_2(\mu\text{-}Cys)_2Pt(dien)]^+$; IV – $[ZnCl(Cys)(His)_2(\mu\text{-}Cys)Pt(dien)]^+$

During the same study that produced the dithiolate bridged bimetallic compound (**I**), the structure of which was used here for benchmarking purposes, a monothiolate bridged intermediate $[(Zn(bme\text{-}dach)Cl)(Pt(dien))]^{+}$ (**II**) was observed using Pt NMR. The optimized structure is shown in Figure 4.2 and the bonding parameters of metal-ligand bonds are given in Table 4.7. The geometry of this compound is almost trigonal bipyramidal with Cl-N(1)-S(2) forming the trigonal plane (as seen from the angles formed by these atoms with Zn). The N(2) and S(1), which is the bridging thiolate, are the axial ligands. The Zn-S(1) bond length is 2.538, Å while the Pt-S bond length is 2.288 Å. Thus, the bridging thiolate is more tightly bound to Pt than to Zn. The other bonds formed by zinc appear normal. Interestingly, the Zn-Cl (2.338 Å) is longer when compared to the optimized structure of **I** (2.224 Å). Given that one of the ligands is weakly bound, the Cl should have bound to Zn^{2+} better. This is because the other S atom binds tighter to zinc (Zn-S(2): 2.305 Å) and the Zn-Cl bond being more ionic is labile. Thus, Cl might be a suitable ligand for zinc to undergo coordination sphere expansion. Another feature that is present in this structure is the orientation of Pt towards S(2) (Figure 4.2). The coordinating plane of Pt is perpendicular to the S(2) and the distance between them is 3.274 Å. Thus, Pt is oriented in the right way for an additive elimination reaction that would lead to the dithiolate bridged model. Given the weak interaction that exists between Zn and bridging S, if it is not part of a chelating ligand, it might leave. However, a quick reaction of Pt with the other S would stabilize the complex as known from the stability of model **I**.

4.4.2. Dithiolate Bridged C_2H_2 Model $[ZnCl(His)_2(\mu\text{-}Cys)_2Pt(dien)]^+$

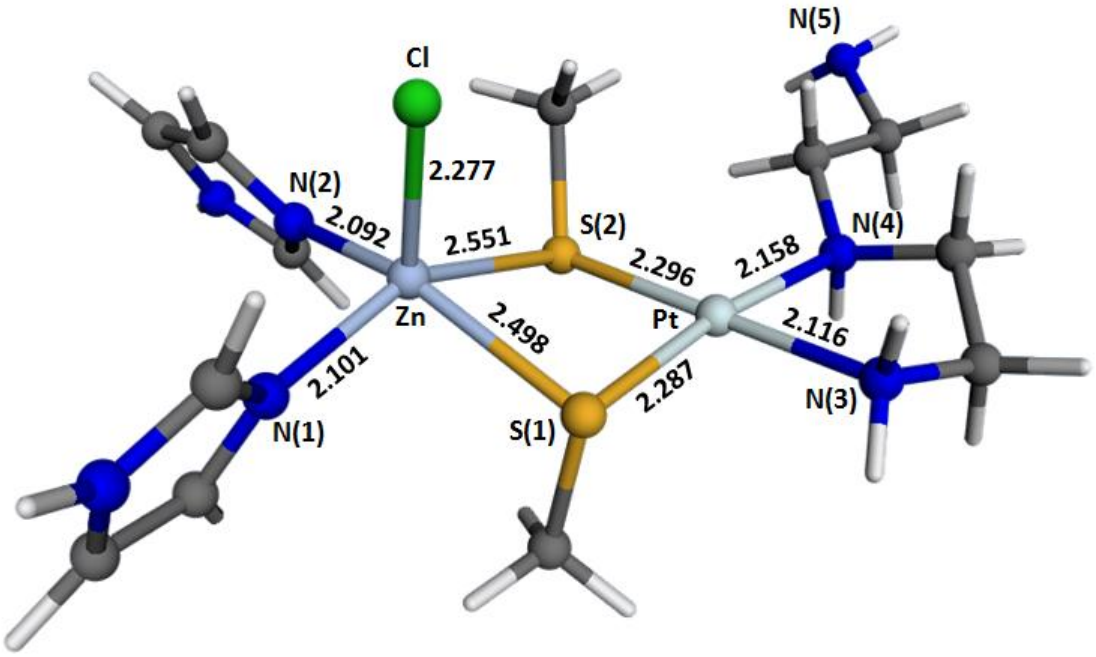

Figure 4.4. Optimized structure of dithiolate bridged $[ZnCl(His)_2(\mu\text{-}Cys)_2Pt(dien)]^+$. The metal-ligand bond distances (Å) are shown.

Based on the geometry of model **I** and using amino acid like ligands, as described in section 4.3, a C_2H_2 type bimetallic, pentacoordinate zinc model with dithiolate bridge $[ZnCl(His)_2(\mu\text{-}Cys)_2Pt(dien)]^+$ (**III**) was built and geometry optimized. Since both the thiolates are bound to Zn and Pt, stabilizing amide groups are not needed. The structure along with metal-ligand bond lengths is shown in Figure 4.3. The entire set of parameters describing the geometry is given in Table 4.7. The geometry of zinc in the structure is distorted square pyramidal (with ∠S(1)-Zn-N(2) and ∠S(2)-Zn-N(1) closer to being linear), as opposed to the previous synthetic models that were trigonal bipyramidal. The ligands being free to move, Zn^{2+} relaxes into a square pyramidal geometry. The Zn-N bond lengths are predicted to be shorter than in the previous two structures. This may be due to the relaxed geometry around Zn^{2+} or due to aromatic nature of nitrogen ligands. The bridging thiolate are once again predicted to be bound tighter to

Pt than to Zn. However, interaction exists between Zn and bridging thiolates, as seen from the geometry of the other ligand around Zn. As the Zn-S bonds are weaker, the Zn-Cl interaction is stronger as compared to model **II**.

4.4.3. Monothiolate Bridged C_2H_2 Model $[ZnCl(Cys)(His)_2(\mu\text{-}Cys)Pt(dien)]^+$

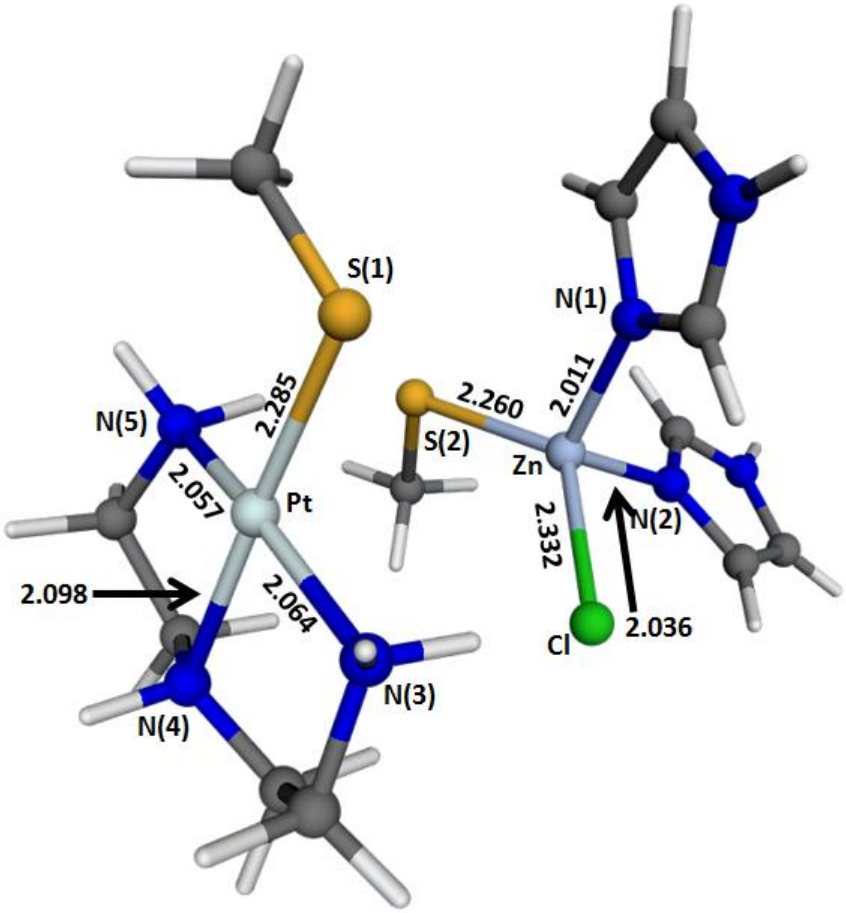

Figure 4.5. Optimization of monothiolate bridged $[ZnCl(Cys)(His)_2(\mu\text{-}Cys)Pt(dien)]^+$ leads to a dissociated structure shown here, thus predicting its instability. The metal-ligand bond distances (Å) are shown.

Similar to the dithiolate model described above, a monothiolate bridged structure with Zn in pentacoordinate geometry resembling model **I** but with amino acid like ligands of the formula $[ZnCl(Cys)(His)_2(\mu\text{-}Cys)Pt(dien)]^+$ (**IV**) was built and geometry optimized. The optimization led

to dissociation of the bridge forming a tetrahedral Zn complex and a square planar Pt complex associated through electrostatic interactions (Figure 4.4). The resulting strucure is of the form $\{[ZnCl(Cys)(His)_2][Pt(Cys)(dien)]\}^+$ (**IV'**). The elongated Zn-Cl bond indicates reduced charge density on Zn^{2+}, which is due to effective binding of the single thiolate group on Zn as seen from the optimal Zn-S bond length of 2.260 Å. Another complex of the same type with stabilzing amide groups to the non-bridging also ended in a similar fashion. The bonding parameters of **IV'** are listed in Table 4.7. It should be noted that in mass spectrometry this would be seen as a single species because these complexes would be part of the same peptide.

4.4.4. Dithiolate Bridged C_3H Model [ZnCl(Cys)(His)(μ-Cys)$_2$Pt(dien)]

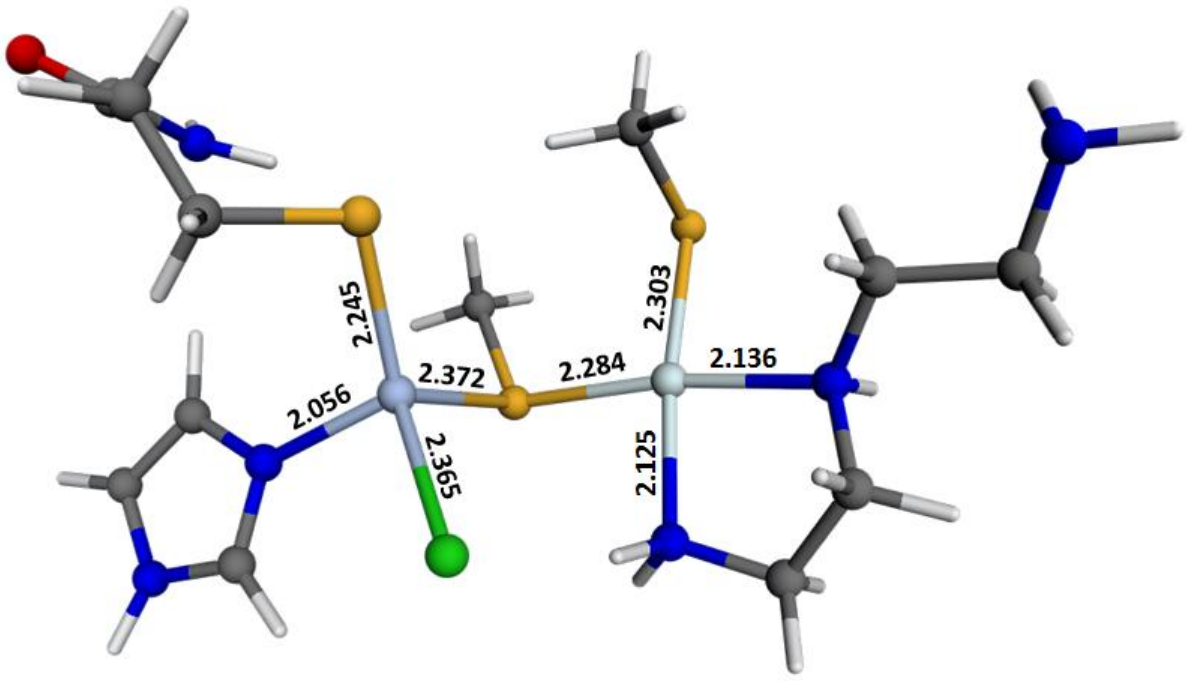

Figure 4.6. Optimization of dithiolate bridged [ZnCl(Cys)(His)(μ-Cys)$_2$Pt(dien)] leads to the formation of monothiolate bridged complex, where zinc is in tetracoordinate state. The metal-ligand bond distances (Å) are shown.

Shown in Figure 4.5 is the optimized geometry of [ZnCl(Cys)(His)(μ-Cys)$_2$Pt(dien)] (**V**), initially modeled with Zn in pentacoordinate state in a C_3H type complex, dithiolate bridged to $[Pt(dien)]^{2+}$. Here, a non-bridging thiolate was modeled to contain an amide group as described in Section 4.3, to mimic stabilization from the protein backbone. The pentacoordinate state of Zn in this complex is not stable as predicted by geometry optimization. This led to the formation of [ZnCl(Cys)(His)(μ-Cys)Pt(Cys)(dien)] (V'), a monothiolate bridged tetrahedral Zn and square planar Pt complex. The geometric parameters of V' are given in Table 4.8. The bridging thiolate of this complex is bound better to Zn than any other complex with a bridging thiolate. Once again, the elongated Zn-Cl bond indicates effective charge neutralization on Zn by the thiolates.

Table 4.8. Geometric parameters of energy minimized complexes the C_3H model complexes. Bond lengths are in Å and bond angles are in deg.

	V	VI
Zn-N(1)	2.056	2.047
Zn-S(1)	2.372	-
Zn-S(2)	-	2.333
Zn-S(3)	2.245	2.272
Zn-Cl	2.365	2.389
Pt-S(1)	2.284	2.295
Pt-S(2)	2.303	-
Pt-N(3)	2.125	2.057
Pt-N(4)	2.136	2.090
Pt-N(5)	-	2.058
∠N(1)-Zn-S(1)	105.2	-
∠N(1)-Zn-S(2)	-	103.2
∠N(1)Zn-S(3)	111.3	112.3
∠S(1)-Zn-S(2)	-	-
∠S(1)-Zn-S(3)	114.9	-
∠S(2)-Zn-S(3)	-	119.6
∠Cl-Zn-N(1)	95.9	96.5
∠Cl-Zn-S(1)	104.1	-
∠Cl-Zn-S(2)	-	112.8
∠Cl-Zn-S(3)	122.7	110.0
∠S(1)-Pt-S(2)	96.5	-
∠S(1)-Pt-N(3)	88.7	92.9
∠S(1)-Pt-N(5)	-	99.4
∠S(2)-Pt-N(4)	92.6	-
∠N(3)-Pt-N(4)	82.3	83.9
∠N(4)-Pt-N(5)	-	83.9

V – [ZnCl(Cys)(His)(μ-Cys)$_2$Pt(dien)]
VI – [ZnCl(Cys)$_2$(His)(μ-Cys)Pt(dien)]

4.4.5 Monothiolate Bridged C_3H Model [($ZnCys_3HisCl$)(Pt(dien))] (VI)

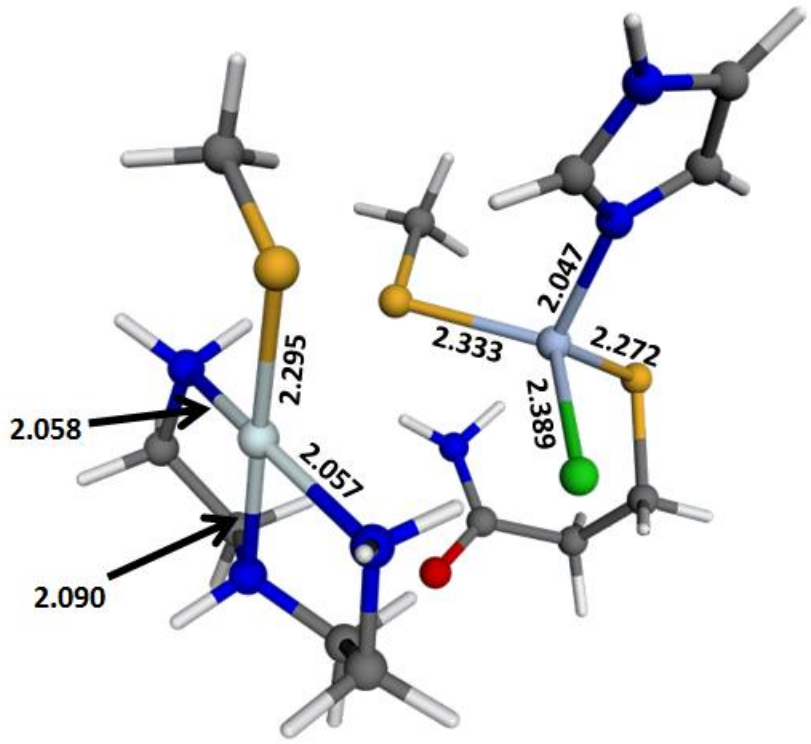

Figure 4.7. Optimization of monothiolate bridged [$ZnCl(Cys)_2(His)(\mu\text{-}Cys)Pt(dien)$] leads to dissociation of the complex, the resulting adduct is shown here. The metal-ligand bond distances (Å) are shown.

The optimization of the [$ZnCl(Cys)_2(His)(\mu\text{-}Cys)Pt(dien)$] (**VI**), where the initial geometry corresponds to a pentacoordinate Zn with monothiolate bridging with Pt, also led to complete dissociation to form two separate complexes as in **IV**. The final structure is of the form {[$ZnCl(Cys)_2(His)$][Pt(Cys)(dien)]}, with Zn in tetrahedral geometry and Pt in square planar geometry. The complexes are again held together by electrostatic interaction from hydrogens of the dien ligand of Pt to a thiolate and chloride that are bound to Zn. The bond between this thiolate and Zn is longer compared to the other thiolate bound to Zn. However, this is not observed in complex **IV,** which is similar except that one of the Cys on Zn is replaced by a His.

The flexibility of Zn^{2+} coordination sphere is well known. However, what dictates the coordination number of zinc in proteins is not well studied. The study of these models suggests that the coordination number on zinc is dictated by the charge density available on the metal. In turn, this greatly depends on the nature and charge of the anionic ligand. In these complexes, the Zn-S bond distance varies between 2.24 – 2.55 Å and the Zn-Cl bond distance varies between 2.22 – 2.38 Å. Thus, compared to Zn-N bond distances formed by imidazole, which vary little (2.01 – 2.10 Å), the thiolate and chloride are much flexible. This can be attributed to the diffuse nature of thiolate and chloride ions compared to smaller N atom. Under the right conditions, as observed in model **III**, the flexibility of these ligands allows zinc to undergo coordination sphere expansion. Another characteristic of Zn that is observable is its preference for sulfur ligands over chloride, given that both are anionic ligands. Chloride is softer than thiolate and Zn^{2+} being an intermediate Lewis acid, prefers to bind to thiolate. As the charge density on the metal would largely depend on the anionic ligands and given that thiolates are preferred over chloride, it can be said that coordination number of Zn^{2+} depends on the number of thiolate ligands. This conclusion is further supported by data from a survey of zinc proteome published earlier.[17] The survey reports a small fraction of Zn^{2+} that exists in pentacoordinate state and most of these do not contain Cys as a ligand. The general trend observed here is that even the presence of a single unperturbed sulfur ligand bound to zinc would destabilize the pentacoordinate zinc intermediate, favoring its dissociation to form tetrahedral zinc. The association complexes that resulted from unstable pentacoordinate geometries will be seen as a single species in mass spectrometry studies. Hence, the results should be interpreted with caution.

4.5. Conclusion

Coordination sphere expansion of structural zinc sites was studied using DFT models. The following conclusions are made from the results presented above:

The choice of appropriate DFT method is important to study zinc complexes. Especially, a good approximation to define electron correlation is required. In this study, PW91 and the similar PBE correlation functionals performed better compared to the commonly used LYP functional. The choice of a proper basis functions is equally important for better results. Use of mixed basis functions on different atoms may be necessary. Higher order polarization on zinc and the ligating nitrogen and sulfur ligands are better. However, basic polarization on chloride was enough to define the bonding between it and zinc. Similarly, diffuse functions are required only on anionic ligands. Using diffuse functions on zinc and nitrogen ligands results in poorer bond lengths between the two atoms.

The diffuse nature of thiolate and chloride ligands allows flexible binding to zinc. This flexibility offered by these ions is the key for the chemistry of coordination sphere expansion in structural zinc sites. This flexibility in the Zn-S bond allows the thiolates stay bound to zinc even under strong external perturbation such as coordination to Pt. However, all the thiolates on zinc should be equally perturbed, or else the same flexibility would lead to stronger bonding between zinc and the unperturbed thiolates, eventually leading to destabilization of the pentacoordinate state.

PART II

The Inhibitory Zinc Site of Caspase-3

5. Introduction

Among the enzymes inhibited by zinc are caspases, the apoptotic proteases. This opens the possibility of metal ions being a regulator of apoptosis, which one of the fundamental processes in higher organisms. As regulation of apoptosis could be the key to cure several neurodegenerative diseases and cancers,[104,105] a better understanding of metal involvement in apoptotic pathways is essential to paint a complete picture of the process.

5.1. Apoptosis: Gene-directed Cell Death

Apoptosis, an integral part of cellular homeostasis in multicellular organisms, is an intrinsically controlled process of cell death.[106,107] It is an ongoing process effective during development, differentiation, tissue maintenance and elimination of defective cells. An apoptotic cell can be recognized by the morphological changes during the process. At the molecular level, these changes are the consequence of DNA fragmentation and protein degradation resulting from the action of apoptotic enzymes. Apoptosis differs from another form of cell death known as necrosis in that the cellular content is always packed within membranes. These apoptotic bodies are assimilated by neighboring cells or macrophages. The classical mode of apoptosis proceeds through the caspase cascade. Central to the process are cysteine dependent aspartate specific proteases (caspases) that cleave off several cellular proteins in a site specific manner culminating in apoptosis. Being a fatal process, it is highly regulated at several stages. Regulatory mechanisms include upregulation of antiapoptotic proteins such as Bcl-2[108] and XIAP,[109]

expression and maintenance of apoptotic enzymes such as caspases as zymogen,[107] protein-mediated activation and posttranslational modification such as phosphorylation and ubiquitination.[110] Dysregulation of these regulators leads to diseased conditions such as degenerative disorder, autoimmune diseases and cancer.[104,105]

5.2. Classification and Commonalities of Apoptotic Caspases:

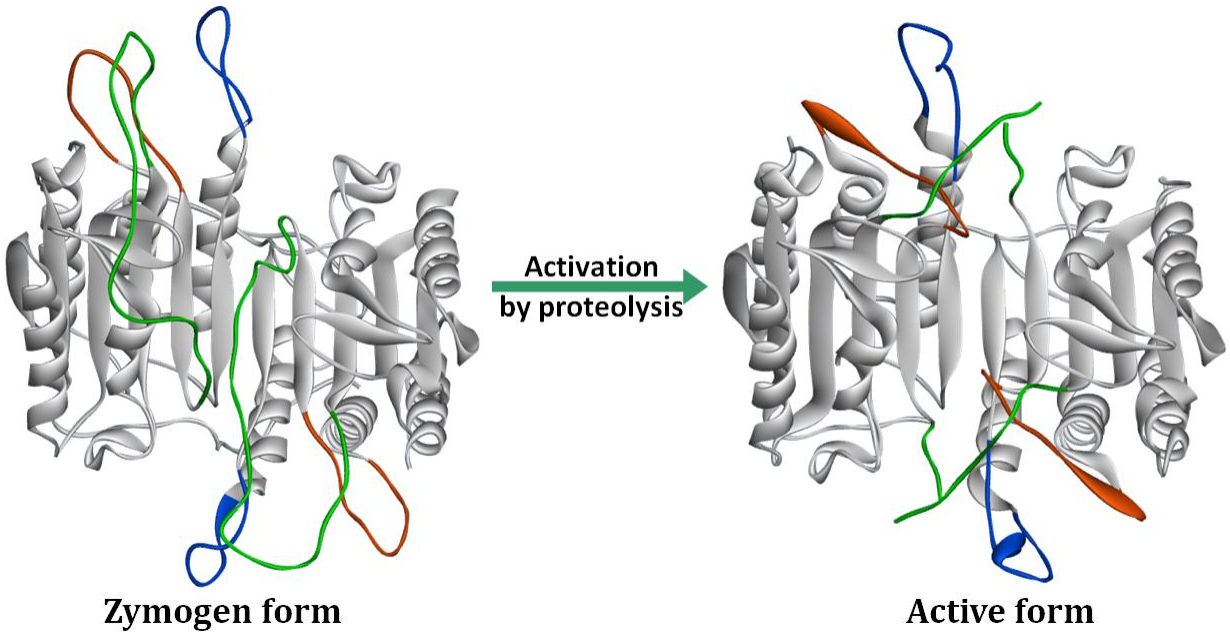

Figure 5.1. Activation of caspases by proteolysis: Changes around the active site of caspases following proteolysis (colored loops) are shown. Procaspase-7 (PDB ID: 1GQF)[111] is on the left and active caspase-7 (PDB ID: 1I4O)[112] is on the right. The site of proteolysis, the intersubunit linker, is in the middle of the green loop.

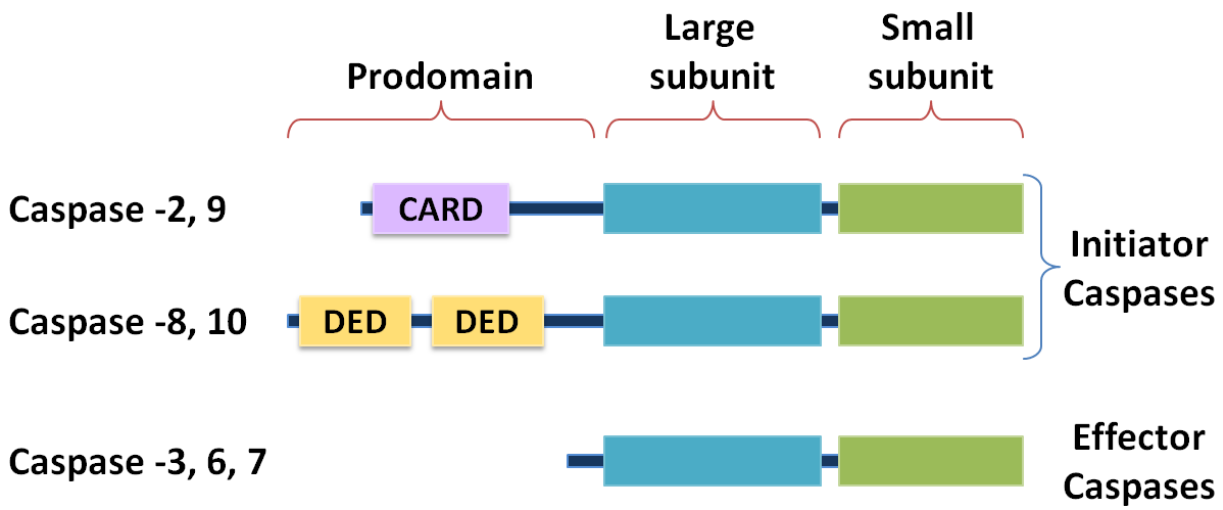

Figure 5.2. Classification of apoptotic caspases based on domains and their roles in apoptosis

Caspases are cysteine proteases that play a major role during inflammation and apoptosis.[113-115] They are highly specific towards an aspartate within a tetrapeptide recognition moiety. Caspases are expressed as zymogens in which the large and small subunits are linked by a short linker. During apoptosis the caspases are activated through proteolysis in a site specific cleavage at the linker regions by other caspases or autocatalysis. The proteolysis leads to a series of new interactions around the active site cavity which leads to proper orientation of the catalytic residues (Figure 5.1). All caspases in their processed form contain a large and a small subunit, which together shape the active site cavity. Apoptotic caspases are broadly classified as initiator caspases and effector caspases (Figure 5.2). The initiator caspases feature one of the two different protein-protein interaction motifs: the caspase activation and recruitment domain (CARD) or the death effector domain (DED). These caspases are activated at an early stage of apoptosis immediately after the apoptotic signal. While the effector caspases are substrates for initiator caspases for activation, they are responsible for the demolition of the apoptotic cell.

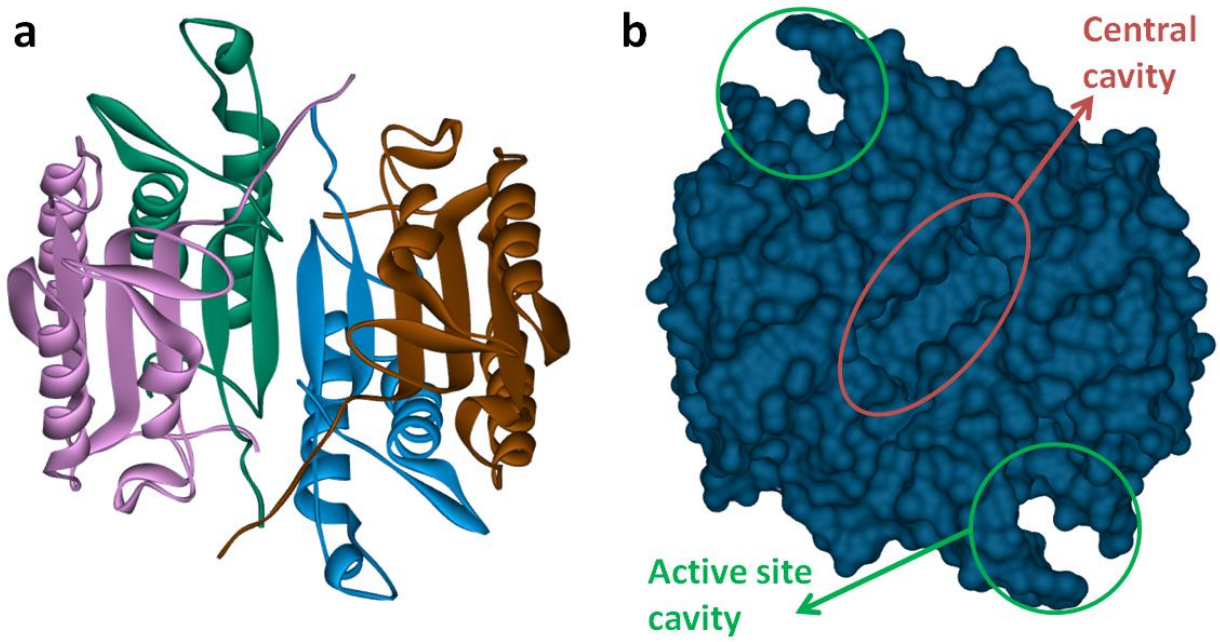

Figure 5.3: Structure of caspases: a) Cartoon of quaternary structure of caspase-3 (PDB ID: 1CP3)[116] with β-sheets and α-helices shown as ribbons. The subunits are colored differently (large subunit: pink and brown; small subunit: green and blue). The other caspases greatly resemble this structure. b) Surface diagram of caspase-3 with the active site cavity and the central cavity formed at the dimer interface highlighted.

Caspases are compactly folded into an open α/β structure (Figure 5.3a).[114,116] In their processed form, each active unit is a heterodimer made of a small and a large subunit and is comprised of a β-sheets formed by 6 β-strands (5 parallel) that are surrounded by five α-helices. In many of the caspases, the heterodimers combine to form a homodimer and this dimerization is required for the activity. The dimerization leads to the formation of a central cavity and the active site cavity is formed from several loops and turns contributed by various subunits (Figure 5.3b). The size of these cavities varies among the caspases and obviously the size of the active site cavity contributes towards substrate specificity. The central cavity is known to have an allosteric site which is a drug target for inhibition of caspases.[117,118]

5.3. Caspase Cascade in Apoptotic Pathway

Apoptosis can be initiated in two different ways, known as the extrinsic or death receptor pathway and the intrinsic or mitochondrial pathway (Figure 5.4).[106,119] In the extrinsic pathway, death ligands (e.g., TNF-α, Fas-L, TRAIL, etc.)[a] from an adjacent cell bind to tumor necrosis factor (TNF) receptors of the cell that is to undergo apoptosis. This leads to oligomerization and internalization of the complex to form the death-inducing signaling complex (DISC). The DISC then recruits adaptor proteins (e.g., FADD, TRADD, etc.)[b] which have death domains (DD). These domains further recruit initiator caspases, caspase-8 and -10 through interaction with homologous death effector domain (DED) present in these caspases. This leads to proximity induced dimerization and subsequent activation of these caspases through autocatalysis. These active initiator caspases that are anchored to the adaptor proteins further activate effector caspase-3 and -7. Caspase-6, another effector caspase, is a substrate for caspase-3. These effector caspases together hydrolyze many of the cellular proteins.[120] Their targets include cytoskeletal proteins such as actin and fodrin, proteolysis of which leads to the cellular morphological changes. Poly(ADP-ribose)-polymerase (PARP), a DNA repair protein, is a caspase-3 substrate thus inactivated during the process. Further, an endonuclease CAD (Caspase-activated DNAse) that exists in its inactive form is activated by caspase-3 by releasing it from its inhibitor through proteolysis. Active CAD fragments DNA at the internucleosomal regions and leads to the chromatin condensation observed during apoptosis.

[a] TNF-a – Tumor necrosis factor alpha; Fas-L – Fas ligand; TRAIL – TNF-related apoptosis inducing ligand
[b] FADD – Fas associated protein with death domain; TRADD – TNF receptor type 1-associated death domain protein

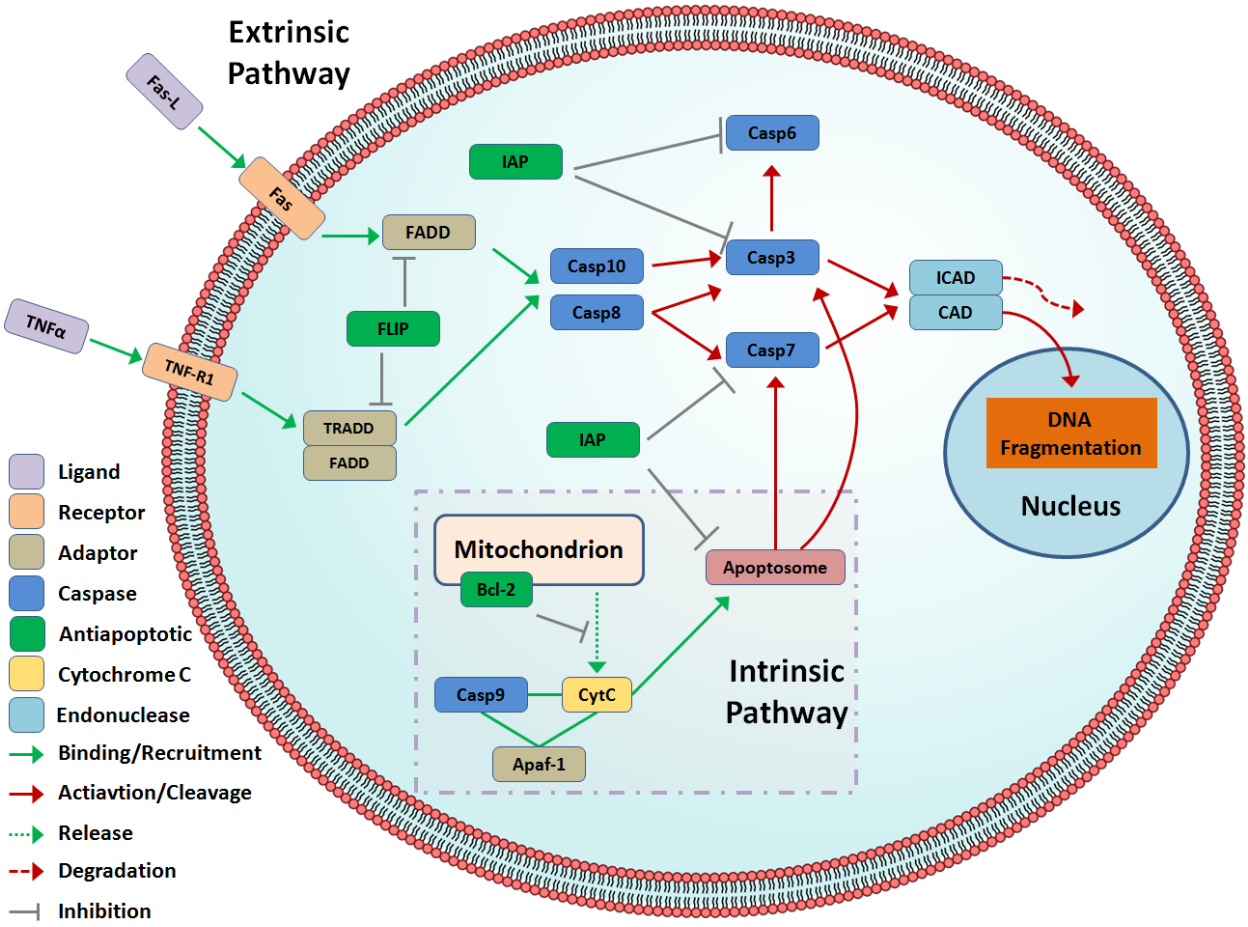

Figure 5.4. A simplified scheme of apoptotic pathways emphasizing the caspase cascade: various proteins involved at different stages are shown.

In the intrinsic pathway, the apoptotic signal is initiated by the mitochondria. Oxidative stress affects the integrity of mitochondrial membrane and leads to permeabilization and release of cytochrome C. The released cytochrome C binds to the apoptotic protease activating factor-1 (Apaf-1) and assists in the formation of an heptameric complex of Apaf-1 known as apoptosome.[121] Formation of the apoptosome allows interaction of CARD (Caspase activation and recruitment domain) on Apaf-1 and caspase-9 leading to the activation of caspase-9. The active caspase-9 then activates caspase-3 and -7 leading to apoptosis.

5.4. Antiapoptotic Proteins

Antiapoptotic proteins add another layer of regulation to this already organized process (Figure 5.4). There are proteins that exert regulation at various stages of the apoptotic pathway. FLIP (FLICE-like inhibitory protein) is homologous to caspase-8 and thus can compete to bind to the DD of the adaptor proteins during death receptor induced apoptosis.[122] Further, the antiapoptotic Bcl-2 family of proteins governs the mitochondrial outer membrane permeabilization (MOMP) and thus prevents the release of cytotoxins such as cytochrome C, Smac (second mitochondria-derived activator of caspases), AIF and endoG, all of which are embedded in the mitochondiral membrane.[108] Along the line, inhibitor of apoptosis (IAP) proteins prevent apoptosis by inhibiting caspases, while this inhibition can be reversed by Smac.[123]

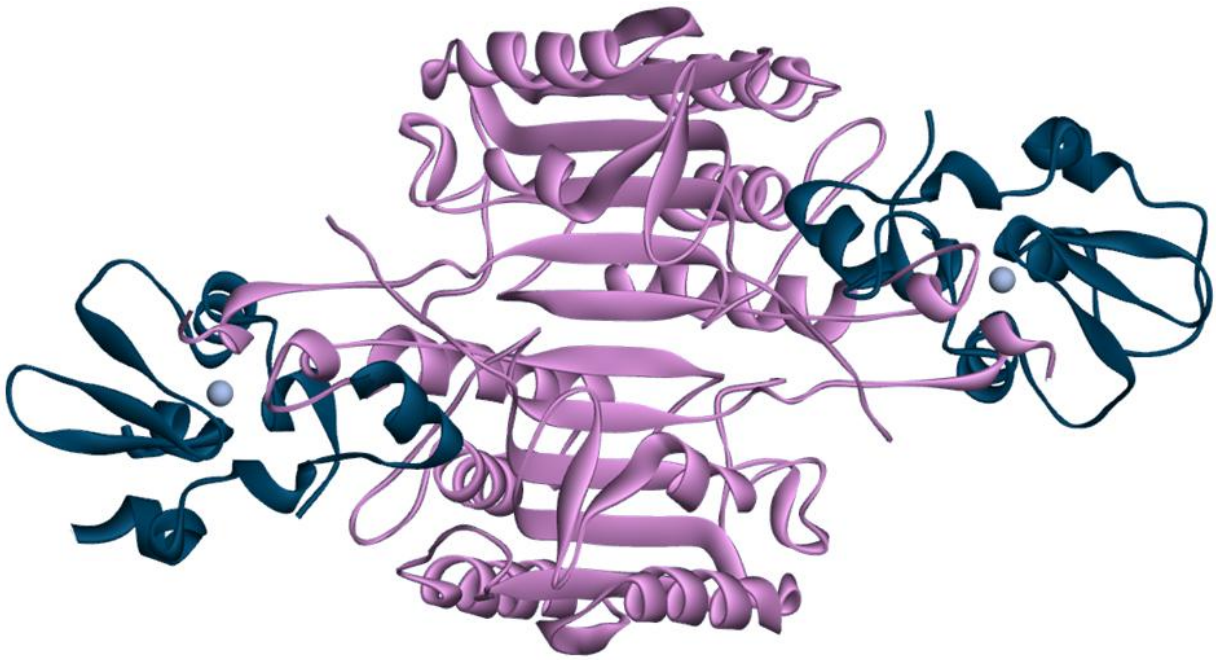

Figure 5.5. XIAP-BIR2 interaction with caspase-3 (PDB ID: 1I3O)[124]. Blue is BIR2 of XIAP and pink is caspase-3. Zinc bound to BIR is shown as grey spheres. The N-terminal end of BIR2 inserts into the active site cavity blocking substrate entry.

XIAP contains three BIR (baculoviral IAP repeat) domains that bind to one zinc each and a RING domain that consists of two zinc binding domains.[125] In the case of caspase-3 and -7, the N-terminal of the second BIR domain (BIR2) of XIAP inserts into the active site cavity preventing the substrate binding (Figure 5.5).[114,125] The third BIR domain (BIR3) is involved in the inhibition of caspase-9, which works by blocking residues that are important for dimerization.[114,125] Smac, which targets both the BIR2 and BIR3, can reverse the inhibition of caspases by XIAP.[125]

5.5. Metal Regulation of Apoptosis

Ca^{2+} is a well known secondary messenger.[126] Its role in apoptosis is also well studied. Release of Ca^{2+} from intracellular stores in response to endoplasmic reticulum stress or cancer drugs lead to apoptosis. The induction of apoptosis by Ca^{2+} signaling is known to happen in multiple ways that involve the mitochondria,[127] calcium activated proteases known as calpains[128] and a Ca^{2+} sensor, calmodulin.[129]

Recently, the involvement of transition metals such as Cu^{2+} and Zn^{2+} in the process of apoptosis has been discovered. Several studies have established the fact that zinc affects apoptosis by using zinc supplementation or deprivation, both *in vitro* and *in vivo*.[16,130-132] In efforts to track down the molecular target of Zn^{2+} in the apoptotic pathway, initially it was reported that the endonuclease, CAD (caspase activated DNase), was the target.[133] CAD being a Ca^{2+}/Mg^{2+} dependent enzyme, it was thought that Zn^{2+} could exchange for Ca^{2+}, thus producing the inhibition. However, later using a cell-free system, it was shown that zinc acts upstream of activation of CAD and that its target was in the cytosol rather than the nucleus.[134] The cytosolic target was identified as caspase-3. Subsequently, *in vitro* studies demonstrated that several of the caspases are susceptible to inhibition by zinc. [135-139]

Additionally, XIAP, a protein from IAP family that regulates apoptosis by inhibiting caspases has been shown to be inhibited by Cu^{2+} reversibly.[140] Interestingly, XIAP has several structural zinc sites. Hence, XIAP loses its activity in the absence of Zn^{2+}.[141] However it is speculated that Cu^{2+} binds to a separate site to bring forth the inhibition. The caspase inhibitory function of XIAP is affected in its Cu^{2+} bound state. Further, the inhibited XIAP has been shown to undergo rapid degradation by cellular proteases.

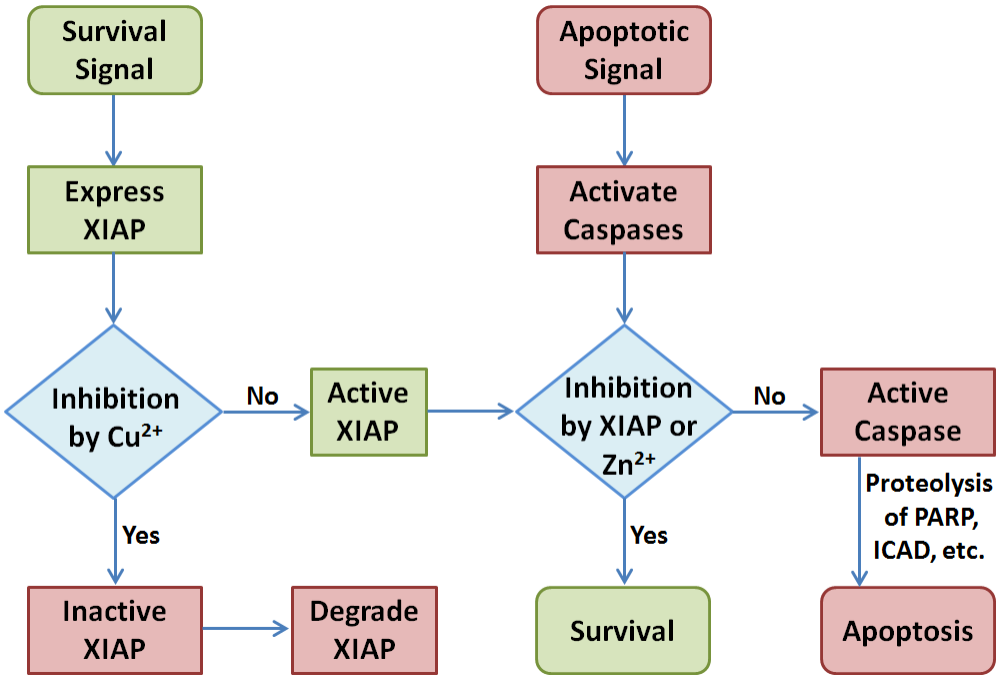

Figure 5.6. Transition metal regulation of apoptosis: Red boxes represent event that favor apoptosis and green boxes represent events that favor survival. The blue diamonds denote regulatory processes involving Cu^{2+} and Zn^{2+}.

This leads us to an emerging picture of how the balance between these two transition metals may act to regulate apoptosis (Figure 5.6). Increase in the level of Zn^{2+} would augment the inhibition of caspases along with XIAP helping evade apoptosis, while an increase in Cu^{2+} would accelerate apoptosis by removal of XIAP, which inhibits caspases. Given that in many forms of cancer and neurodegenerative diseases the levels of these proteins and ions are found to

be abnormal,[105,142-144] further studies are necessary to establish the role of these endogenous ions in regulation of apoptosis.

5.6. Objective

This part of thesis presents an attempt to find the molecular basis of inhibition of caspases by Zn^{2+}, which is aimed at expanding the current knowledge of metal involvement in apoptosis. The studies will be narrowed down to caspase-3, which has been the focus of many studies as it is responsible for the cleavage of several important cellular substrates, and thus effecting apoptosis. Currently a few speculations exist about zinc binding site in caspase-3. During this study, enzyme kinetics and biophysical studies will be used to gain an understanding of the molecular aspects of the inhibitory zinc site. Further, based on the results from these studies, the zinc binding site can be predicted and modeled.

6. Theory and Principles

6.1. Enzyme Kinetics

The study of rates of enzyme catalyzed reactions through mathematical models can provide useful information about the nature of the active site, mechanism and inhibition of the enzyme. Enzymes catalyze reactions by lowering the activation energy required for the transition from the reactant to the product. They bind to their substrates with great specificity to interact and activate the substrate often by placing them in a conformation favorable for the reaction. Further, key residues that help in the process are positioned properly to facilitate the catalysis. Although the steps involved in an enzyme catalyzed reaction can be complex, in most cases approximation is possible to allow the use of a simplified model.

The most commonly used model was developed by Michaelis and Menten.[145] Considering a simple enzymatic reaction of reactant, also known as the substrate, being converted to the product is given by,

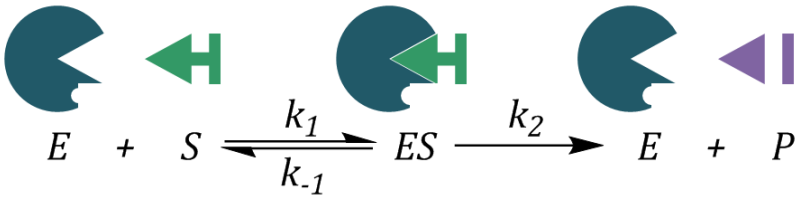

(6.1)

where the enzyme (E) binds to the substrate (S) to form the enzyme substrate complex (ES). This is an equilibrium process, the rate of the forward and reverse directions are k_1 and k_{-1}. The ES then yields the free enzyme and the product (P), the rate of which is determined by k_2. For

such an enzymatic process, the plot of reaction rate (v) versus the substrate concentration, $[S]$, takes a hyperbolic form as shown in Figure 6.1.

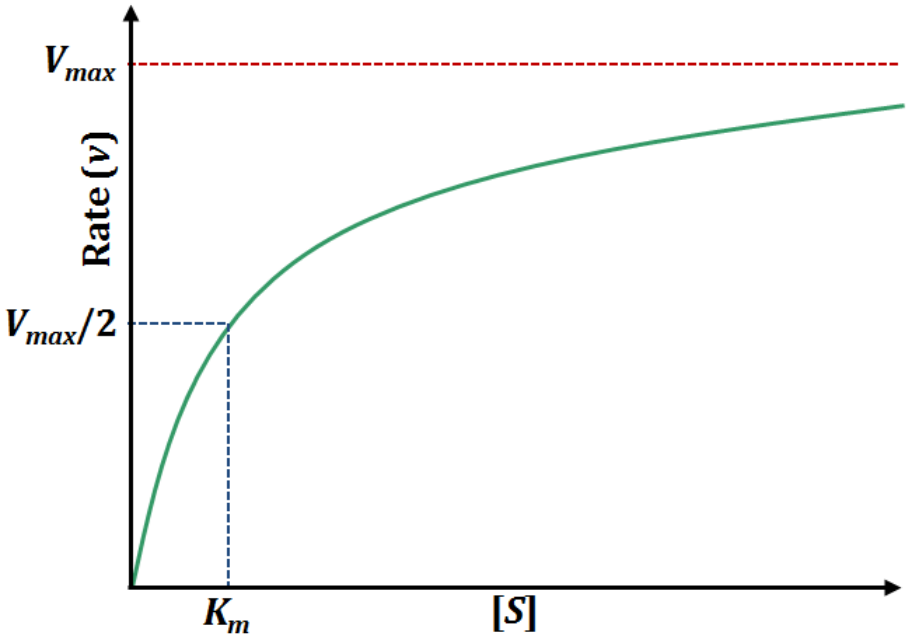

Figure 6.1. A typical plot of change in reaction rate with substrate concentration for a reaction of type shown in Eq. 6.1: The physical significance of the Michaelis – Menten parameters are shown.

At lower $[S]$, v varies linearly with $[S]$, as the $[S]$ increases, the relationship between it and v becomes non-linear and reaches a plateau. The Michaelis – Menten equation, derived using some approximations, fits the hyperbolic behavior of this curve. The equation is given by:

$$v = \frac{V_{max}[S]}{K_m + [S]} \tag{6.2}$$

where K_m is the Michaelis – Menten constant, which is inversely proportional to substrate binding affinity of the enzyme. V_{max} is the maximum reaction velocity that is reachable by the

enzyme at a substrate concentration much higher than the K_m (unit is mol L^{-1}). K_m is a single constant which combines all of the three rate constants in Eq. 6.1,

$$K_m = \frac{k_{-1} + k_2}{k_1} \tag{6.3}$$

and the V_{max} is given by,

$$V_{max} = k_{cat}[E_t] \tag{6.4}$$

where k_{cat} (unit is s^{-1}) is the measure of maximum turnover capacity of the enzyme under saturating substrate conditions. The catalytic efficiency of the enzyme is defined as k_{cat}/K_m.

The kinetic parameters K_m and V_{max} defined above can be obtained by non-linear curve fitting of a plot shown in Figure 6.1. The easier way to get these from a linear plot obtained by linearizing the Eq. 6.2, which can be done by taking a reciprocal of it and using $1/v$ and $1/[S]$ to obtain the double-reciprocal Lineweaver – Burk plot (Figure 6.2).[146]

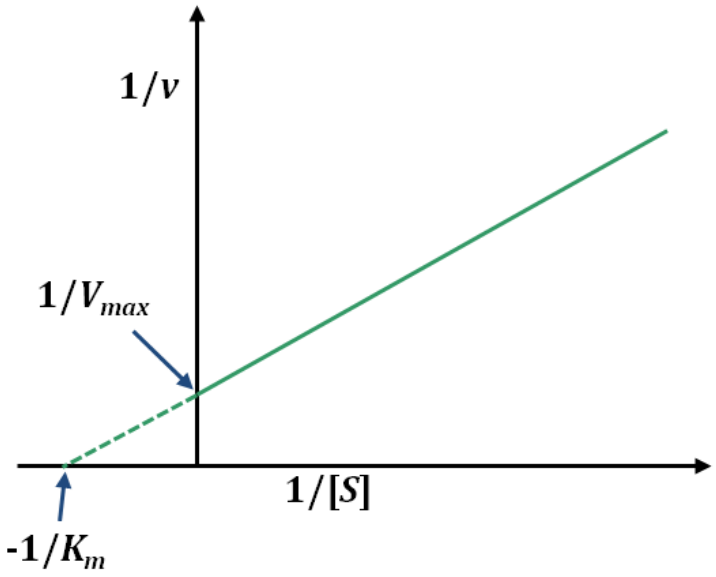

Figure 6.2. A typical Lineweaver-Burk plot obtained from the reciprocal of Eq. 6.2: The significance of the intercepts from which the kinetic parameter can be calculated are shown.

Although the kinetic parameters can be obtained from the Lineweaver – Burk plot in a straightforward manner, these can be less accurate. However, linear plots are really useful in visualizing the changes in parameters during enzyme inhibition studies.

Considering the effect of an inhibitor (I) on the enzymatic reaction of the form given in Eq. 6.1, the possible processes are given by,

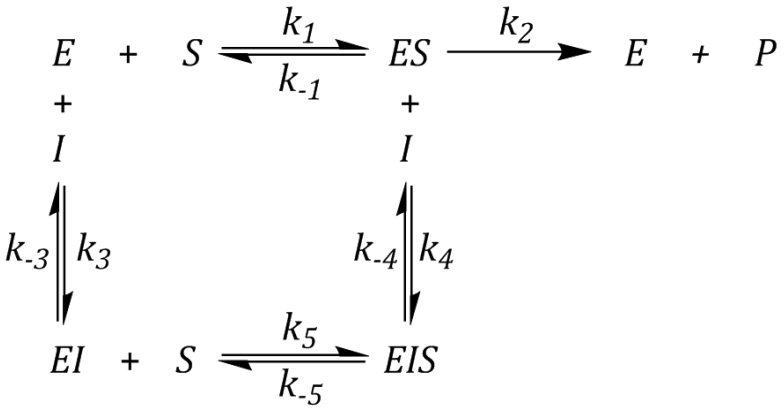

(6.5)

Here, different scenarios of the inhibitor interacting with the enzyme are shown. Two main processes involving the inhibitors in the above equation are the interaction of E with I to form EI and the interaction of ES with I to form EIS. The Michaelis – Menten equation can be modified into a general form that takes into account all these possible interactions:

$$v = \frac{V_{max}[S]}{K_m\left(1 + \frac{[I]}{K_i}\right) + [S]\left(1 + \frac{[I]}{K_i'}\right)} \tag{6.6}$$

where K_i is the dissociation constant for I binding to E and K_i' is the dissociation constant for I binding to ES.

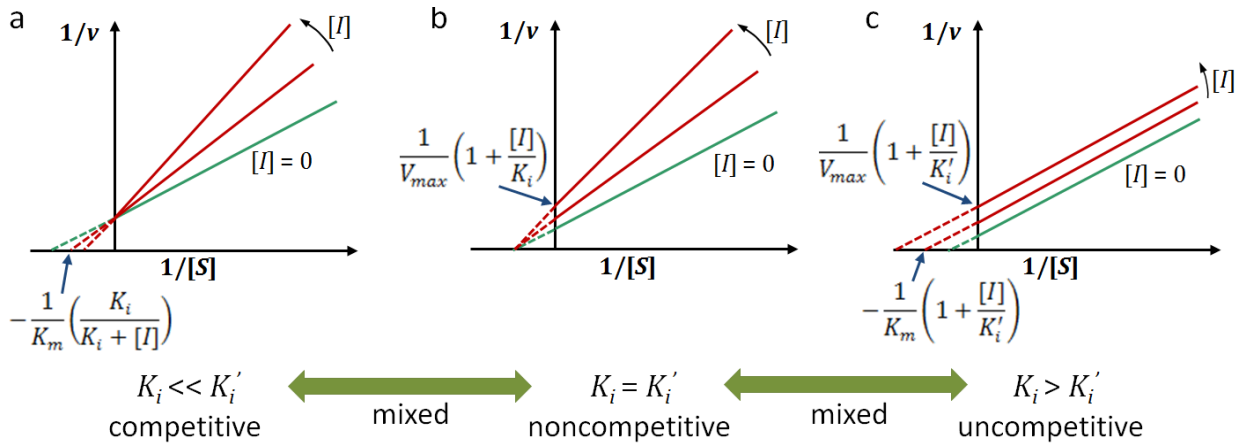

Figure 6.3. Typical Lineweaver – Burk plots demonstrating the three distinct types of inhibition: a) competitive, b) noncompetitive and c) uncompetitive. The condition for mixed inhibition is also shown.

There are three distinct scenarios of enzyme inhibition that can be classified based on the inhibitors affinity to E and ES. The characteristic Lineweaver – Burk plots and the conditions for each type of inhibition are shown in Figure 6.3. In the first case, namely competitive inhibition, the inhibitor competes with the substrate and replaces it. Hence the affinity of I towards ES is too low, in other words, K_i' is too high. The other case is noncompetitive inhibition, where the inhibitor has equal affinity to both E and ES. In this case, the inhibitor would bind to a distinctive pocket other than the substrate binding pocket. The third case is uncompetitive inhibition where I exclusively binds only to the ES. Here, the binding of the substrate induces a change in the enzyme that is required for I to bind. More often, inhibitors do not conform specifically to any of these well defined scenarios. They rather exhibit a mixed behavior, where the inhibitor has unequal but certain affinity to both E and ES; these inhibitions are termed mixed type inhibition. Eq. 6.6 accounts for this type of inhibition.

6.2. Fluorescence Spectroscopy

Luminescence is the phenomenon in which a substance absorbs light of a particular energy. As a result, it gets excited to a higher electronic state and as it returns to the ground state it emits light of a lower energy. Luminescence can be divided into two types: fluorescence and phosphorescence. They differ in their excited state spin from which they emit. Fluorescence occurs from a singlet excited state, while phosphorescence occurs from a triplet excited state. Since the relaxation back to the ground state is spin allowed in the case of fluorescence, the emission occurs quickly, with a typical fluorescence life time of about 10 ns. However, the spin forbidden transition, in case of phosphorescence occurs much slower – in the timescale of milliseconds to seconds. It should be noted that not all of the absorbed photons lead to an emission. There is always a chance of non-radiative decay to return to the ground state. Thus, two competing processes, radiative decay and non-radiative decay, determine the fluorescence lifetime and the quantum yield of the fluorophore (a molecule that fluoresces).

The wavelength maximum and the intensity of fluorescence of a fluorophore are dependent on its environment. Hence, changes in the intrinsic fluorescence of a protein can be used as a tool to study protein folding, substrate binding, changes local to the environment of the fluorescent amino acid, etc. Phenylalanine, tyrosine and tryptophan are fluorescent. However, tryptophan has the highest quantum yield and thus dominates the fluorescence spectrum of a protein containing all three of these residue types. The absorption maximum of tryptophan is at 280 nm. The emission maximum is known to vary from 308 nm to 355 nm depending on the protein environment. A tryptophan buried inside the protein fluoresces with higher intensity and the spectrum is blue shifted. A solvent exposed tryptophan experiences higher quenching; hence, its intensity decreases and the spectra is red shifted. It is known that nearby aspartates and

glutamates can quench the fluorescence of tryptophan. It is predicted that positively charged residues near the benzene or negatively charged residues near the pyrrole end of the indole ring will produce a red shift.[147]

6.3. Fluorescence Polarization

Fluorescence polarization is based on the phenomenon that fluorophores preferentially absorb light when the electric field of the electromagnetic wave is aligned to its transition dipole. Thus, when plane polarized light is used, only those molecules with dipoles properly oriented absorb the light. As the excited molecule tumbles around, the plane of emitted light is randomized. Since the mobility of the molecule is related to its molecular weight, smaller molecules lose the polarization faster than larger molecules. Thus, the technique can be used to measure the association of small molecules, tagged with a fluorophore, to large biomolecules. Polarization is given by

$$P = \frac{F_{\parallel} - F_{\perp}}{F_{\parallel} + F_{\perp}} \tag{6.7}$$

7. Prediction of Inhibitory Zinc Binding Site in Caspase-3

Caspases, which are central to the process of apoptosis, represent the most important targets of apoptosis based therapies. The therapeutic agents include caspase inhibitors and caspase activators.[148,149] Caspase inhibitors act as anti-apoptotic agents, some of which are currently in phase 1 and phase 2 clinical trials for treatment of myocardial infarction, stroke, acute liver failure and rheumatoid arthritis.[148] These are mostly peptide based inhibitors targeting the active site of caspases by mimicking the substrates. On the other hand, caspase activators are in preclinical trials and are being tested as anticancer agents.[149] These include chimeric proteins transferred by gene delivery for induction of dimerization and autocatalysis of caspases, small molecules that promote formation of apoptosome and the RGD peptide that has been shown to directly activate caspase-3. As an alternative, sequestering inhibitory zinc ions by using compounds like PAC-1 (procaspase activating compound-1) or its sulfonamide derivative S-PAC-1 has been shown to activate caspases, induce apoptosis *in vitro* and suppress tumors *in vivo*.[150] Since this method uses a small molecule, it is more effective compared to the others being tested. PAC-1 was discovered in a library screening for an activator of procaspase-3[151] and later the mechanism of its activation was established as a zinc sequestering agent.[152] Knowing the inhibitory zinc binding site in caspases would greatly accelerate design and improvement of target chelating agents. The strategies used to gain additional information about zinc inhibition of caspase-3, which eventually led to the prediction of a potential zinc binding site, is presented in this chapter.

7.1. Speculations from Previous Studies

The first study that established the inhibitory effect of zinc on caspase-3 reports an IC_{50} value of 0.1 µM for recombinant caspase-3 and IC_{50} of 1 µM for an apoptotic extract.[136] In the same paper, based on structural data and mechanism of caspases, and given the low binding affinity of zinc to the site, it was speculated that zinc could bind to one or both the catalytically important His and Cys at the active site of caspases (Figure 8.1) to produce the inhibition. Later, in another study a K_i^{app} of 0.15 µM was reported (K_i^{app} of 8.8 µM before for the influence of β-mercaptoethanol that was used as a reducing agent).[135] The study assumed competitive inhibition based on the same assumption of zinc binding to the active site dyad. Recently, a study predicted the presence of two zinc binding sites in caspase-9 and one of these involves the catalytic dyad.[139] The enzyme kinetics were reported to be of mixed type. Another study reported an allosteric zinc binding site in capase-6 based on the X-ray crystal structure.[138] In the same study, based on ICP-OES data, it was reported that caspase-3 binds to 3 zinc ions, caspase-6 and -7 to one zinc ion, while caspase-9 binds to 2 zinc ions. All these studies still maintain the possibility of the catalytic dyad being an inhibitory zinc binding site.

7.2. Structural Features of Caspase-3 Active Site

The active site fold is common to all caspases and it is formed from several loops and turns that are part of three different subunits (Figure 7.1). In caspase-3, the L1 loop contains residues 52 – 66 and the L2 loop contains residues 163 – 175 with the catalytic Cys is at position 163. Both these are part of large subunit. The L3 loop is made of residues 198 – 213 and the L4 ranges from residue 247 to residue 263. These are part of the small subunit. The L2' loop is formed by residues 176 – 192 and it is contributed by the small subunit of the other caspase

molecule that forms the dimer. The catalytic His121 is part of an antiparallel β-sheet of the large subunit. Many of these loops are properly formed only after the activation by cleavage at the processing sites. The changes in these loops arising after activation are shown in Figure 5.1.

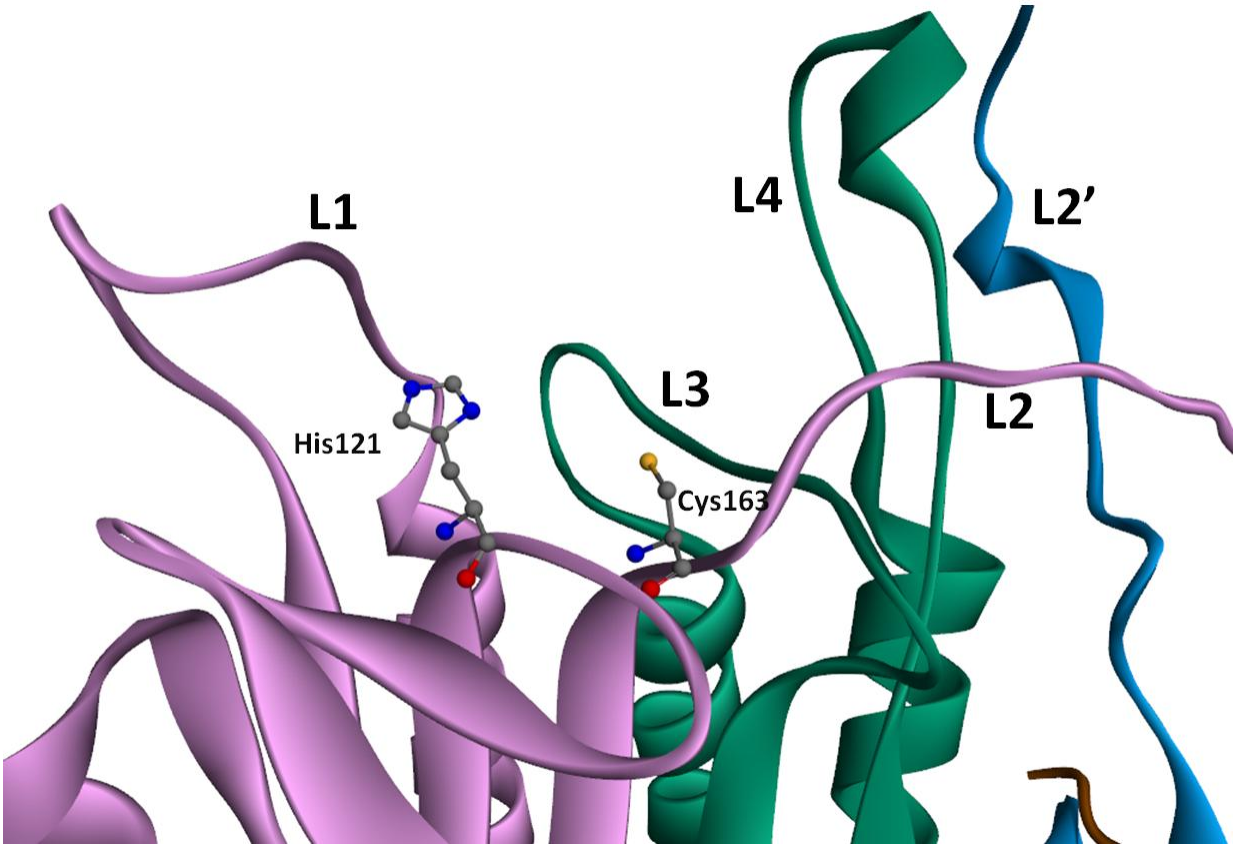

Figure 7.1. The secondary structure that shapes the active site of caspase-3: the five different loops and the catalytic dyad are labeled. The large sub unit is colored pink, the small subunit is colored green and the small subunit from the other caspase molecule in the dimer is colored blue (PDB ID: 1I3O).[124] Ala163 in the crystal structure was changed to Cys163.

Once formed, these loops are held in place by several stabilizing interactions: hydrophobic, hydrogen bonding and ionic. For this reason, very little variability is seen in most X-ray crystal structures as shown in Figure 7.2. Among these loops, L1 and L4 are the most flexible. The backbone at the catalytic residues shows very little variability.

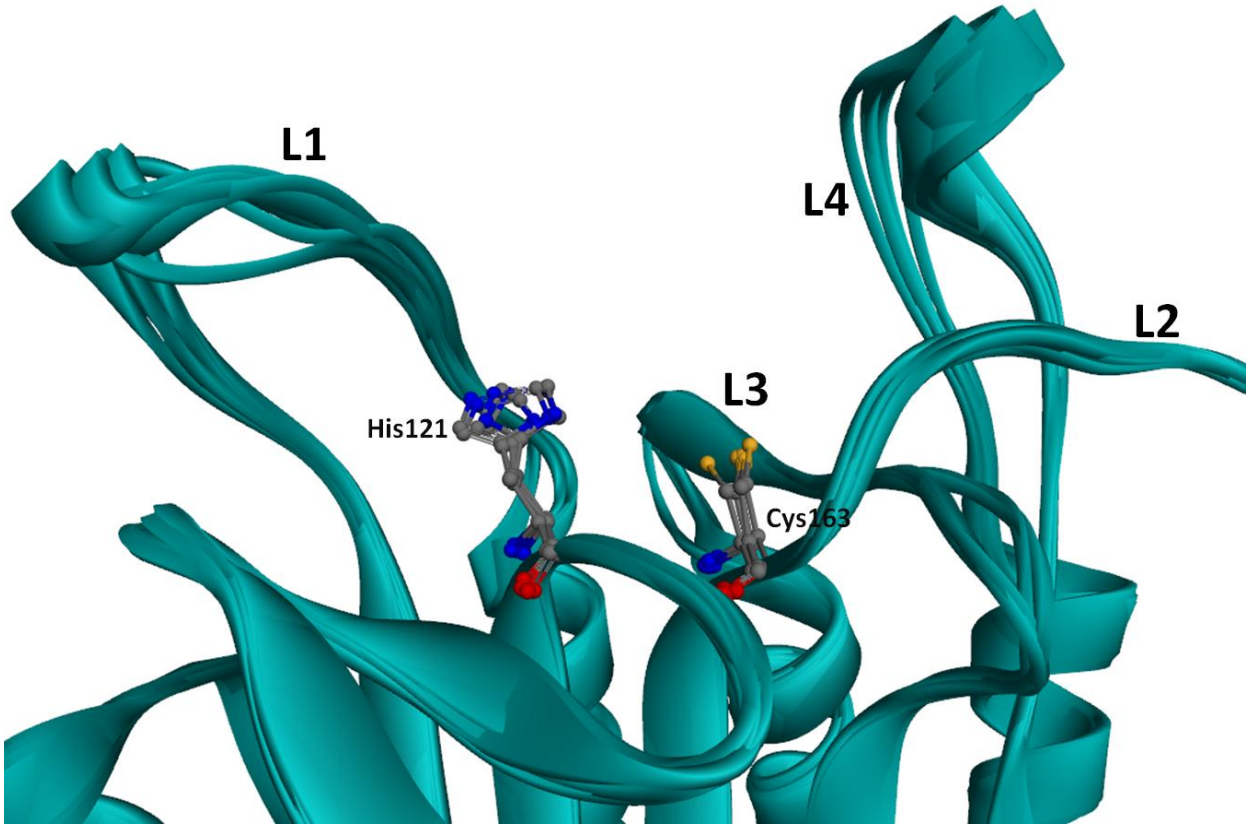

Figure 7.2. Flexibility in the loops that form the active site of caspase-3 shown through an overlay of representative crystal structures of caspase-3 (PDB ID: 1I3O,[124] 1GFW,[153] 1PAU,[154] 3DEK,[155] 3GJQ[156] and 1CP3[116]).

The largest displacement in C_α of Cys163 is 0.49 Å, while C_α of His121 is 0.46 Å. After the activation, the Arg164 forms a cation-π interaction with Tyr197, which stabilizes the fold. This interaction is the known target of allosteric inhibitors.[117] This interaction, along with several hydrogen bonding and ionic interactions along the L2 loop, fix the position of Cys163 in place. The His121, being part of an antiparallel β-sheet, is almost in place well before the activation. However, the side chain being flexible, it is held in place by several hydrophobic groups such as Phe55, Met61 and Phe128. The importance of these residues is apparent when considering that they are partially conserved as bulky hydrophobic groups.

7.3. Important Active Site Residues and Substrate Recognition

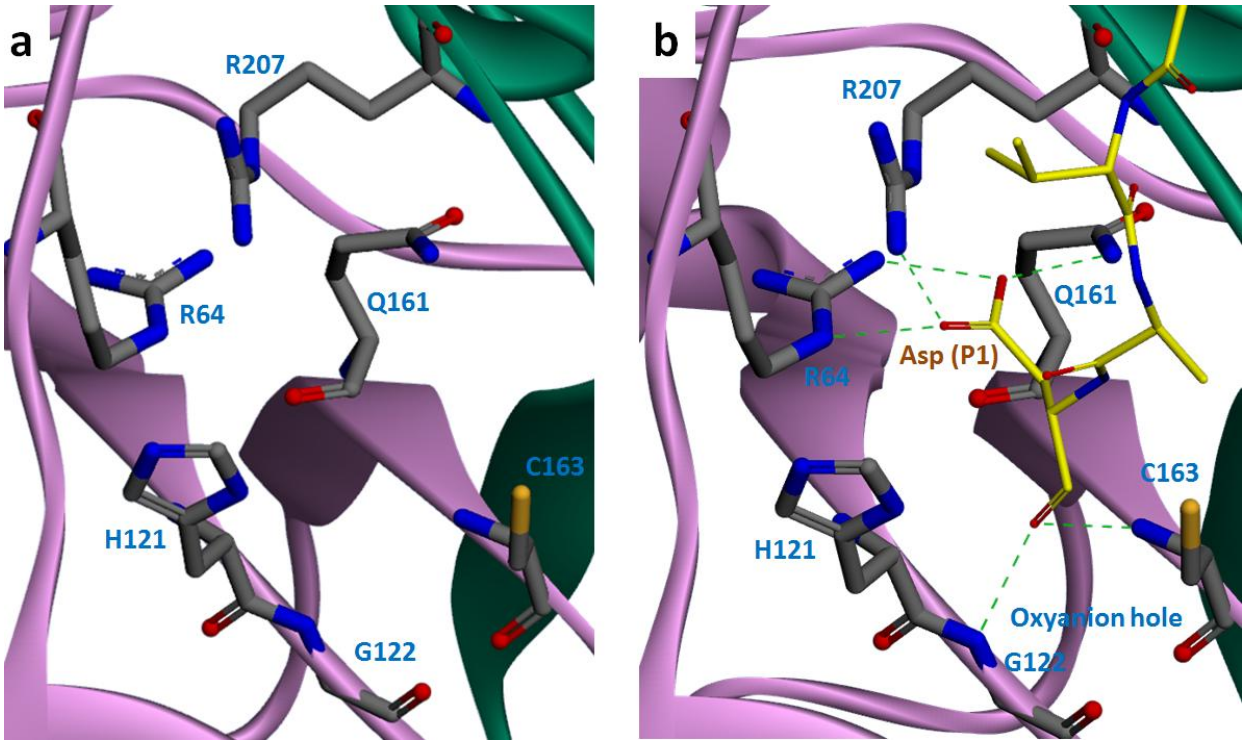

Figure 7.3. a) Active site residues of caspase-3: The catalytic residues and residues important for substrate recognition are shown. b) Substrate recognition at the active site: the hydrogen bonding interactions between the basic residues of caspase and the P1 Asp of the substrate that confers the specificity are shown. (PDB ID: 1CP3)[116]

The active site of caspases is comprised of the catalytic residues His121, Cys163 (the dyad) and three basic residues (Arg64, Q161 and Arg207) that are involved in substrate recognition (Figure 7.3a). Among the basic residues, Arg64 is part of the L1 loop and Arg207 is part of the L3 loop. These residues are also folded in to proper position following the activation. All caspases have a high specificity towards a tetrapeptide sequence that they recognize. The residues are labeled P1-P2-P3-P4. The P1 aspartate is invariable to all caspases. Residues at the other positions vary for different caspases, which is due to shape of the pockets formed by the residues specific each caspase. Caspase-3 and -7 are highly specific to the sequence DEVD. The

substrate recognition in caspase-3 is shown in Figure 7.3b. The P1 Asp is recognized through several hydrogen bonding interactions formed between it and the basic residues mentioned before. Further, the amide carbonyl to be cleaved interacts with the backbone amide hydrogens of residues Gly122 and Cys163 and this pocket is called the oxyanion hole. It can be seen that the catalytic residues are positioned well to react with the carbonyl of P1 residue of the substrate.

7.4. The Odds of Zinc Competing with the Substrate

It is a general belief that the catalytic dyad of caspases is the inhibitory zinc binding site. Since His and Cys are good zinc ligands and also they are well spaced at about 6 Å, it is a reasonable speculation. However binding to just two protein ligands may not offer the affinity to compete with the substrate that is well suited for the active site pocket. Moreover, the catalytic dyad may not offer the flexibility for zinc to bind properly. Previous studies have only assumed a competitive type model and there is a lack of proper enzyme kinetics data for zinc inhibition of caspase-3 from which the type of inhibition can be deduced. Hence, to begin, systematic enzyme kinetics will be performed to obtain further information about the type of zinc inhibition of caspase-3.

7.5. Methods and Materials

WT Human caspase-3 gene in pET23b vector was obtained from Addgene (plasmid 11821).[157] Casapase-3 substrate, Ac-DEVD-pNA, was obtained from Enzo® Life Sciences. Tris, $ZnSO_4$, Chelex® and Ac-DEVD-CHO were obtained from Sigma-Aldrich. NaCl was obtained from Fisher Scientific. FITC-C6-DEVD-fmk was obtained from Assay Biotechnology.

7.5.1. Point Mutation:

Site directed mutagenesis using Quikchange II kit (Agilent Technologies) was performed to repair a mutation (F55S) in the original plasmid. The following were the primers used for the reaction: 5'-agatgggtttatgtataataattaataataagaattttcataaaagcactggaatgaca-3' and 5'-tgtcattccagtgcttttatgaaaat-tcttattattaattattatacataaacccatct-3'.

7.5.2. Expression and Purification of WT caspase-3:

The plasmid containing the WT caspase-3 gene was transformed into BL21(DE3)pLysS cells, expressed and purified as per published procedures[158], except that after SDS-PAGE analysis, the fractions were pooled and concentrated using centrifugal filters (Millipore, M.W. cutoff 3.5 kDa) BME to a final concentration of 20 mM was added and further purified by dialysis in the minimal buffer. The purified protein was stored in small aliquots at -80^{o}C until required.

7.5.3 Caspase-3 Activity Assay

Activity assays were performed in 96 well plates. Appropriate volume of buffer (50 mM Tris, 100 mM NaCl) was added to the wells, followed by the addition of the enzyme (100 nM). If required, EDTA or BME was added to the wells. The substrate (Ac-DEVD-pNA) was added to the reaction at the end. The final reaction volume was 100 μL. The activity of the enzyme was measured by monitoring the absorbance of *para*-nitroaniline (pNA) released due to the action of caspase-3 on the substrate.

7.5.4. Enzyme Kinetics:

In a 96 well plate, caspase-3 (100 nM) was incubated in minimal buffer (Tris, 100 mM NaCl) without or with 200 nM to 1400 nM of Zn^{2+}, followed by the addition of the substrate (25 μM – 200 μM). The final reaction volume was 100 μL. After 30 s the absorbance at 405 nm was measured every 10 s for 3 min using Envision Plate reader. The experiment was repeated 3 times. The concentration of pNA was calculated from the absorbance values based on pNA standards. The points from a linear range of first 1 – 2 min were used to calculate the reaction velocity. The data was plotted in a Michaelis-Menten type plot and analyzed in Graphpad Prism®. Further by active site titration using the irreversible inhibitor Ac-DEVD-fmk, the total active enzyme concentration was found to be 17.5 nM.

7.5.5. Fluorescence Polarization:

100nM of caspase-3 was incubated with 0.5 – 10 μM Zn^{2+} before the addition of 40 nM FITC-C6-DEVD-fmk. The mixture was transferred to the cuvette and equilibrated for 5 min (the FP did not change after 3 min) before measurement. The excitation wavelength was 492 nm and

the polarization was measured at 515 nm with an averaging time of 2 s. The experiments were done using a Varian Cary Eclipse spectrophotometer.

7.5.6. Fluorescence Spectroscopy:

The concentration of caspase-3 was 1 μM. The enzyme was incubated with 1 μM – 10 μM $Zn2^{+}$. Following this, Ac-DEVD-CHO was added in experiments that required it. The samples were excited at 280 nm and the spectra were scanned from 290 nm to 400 nm with an averaging time of 4 s. The experiments were done using a Varian Cary Eclipse spectrophotometer.

7.6. Results and Discussion

7.6.1. Fixing a Mutation in Original Plasmid

During the preparations for expression of WT caspase-3, mutations were found while comparing the sequence provided by Addgene with the WT Caspase-3 sequence. There were three point mutations (164T>C, 441C>T and 444C>T) in the plasmid. The last two mutations were part of a PstI restriction site. These were confirmed by digestion with PstI restirction enzyme. Both the C>T mutations were silent but 164T>C was a missense mutation which would translate as F55S. As mentioned in section 7.2, F55 is one of the hydrophobic residues responsible for the proper positioning of catalytic His. Hence this mutation was repaired by site directed mutagenesis before proceeding further.

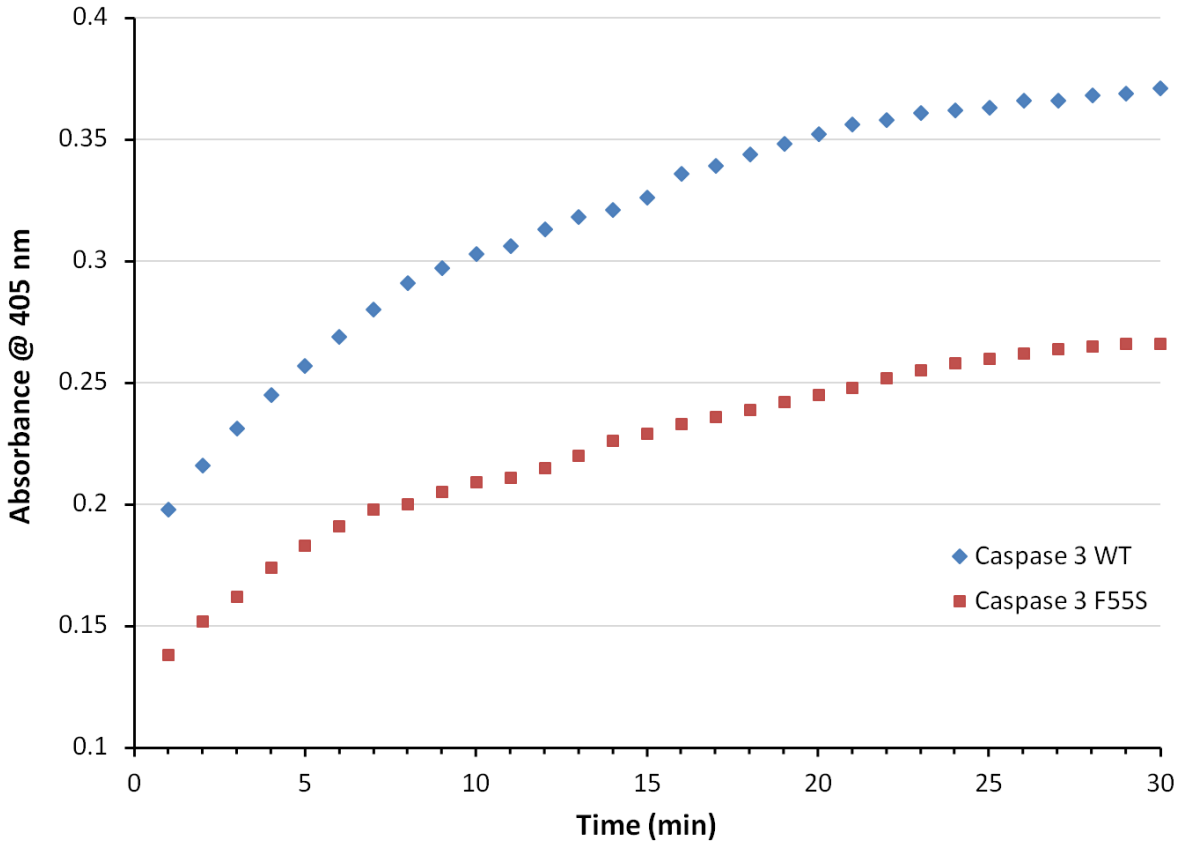

Figure 7.4. Comparison of the activities of caspase-3 WT and caspase-3 F55S.

After this repair, both caspase-3 WT (obtained by fixing F55S) and Caspase-3 F55S were expressed, purified and their activities were compared. The F55S mutant was found to be less active than the WT (Figure 7.4), which proves the importance of proper positioning of catalytic His.

7.6.2. Buffer and Conditions

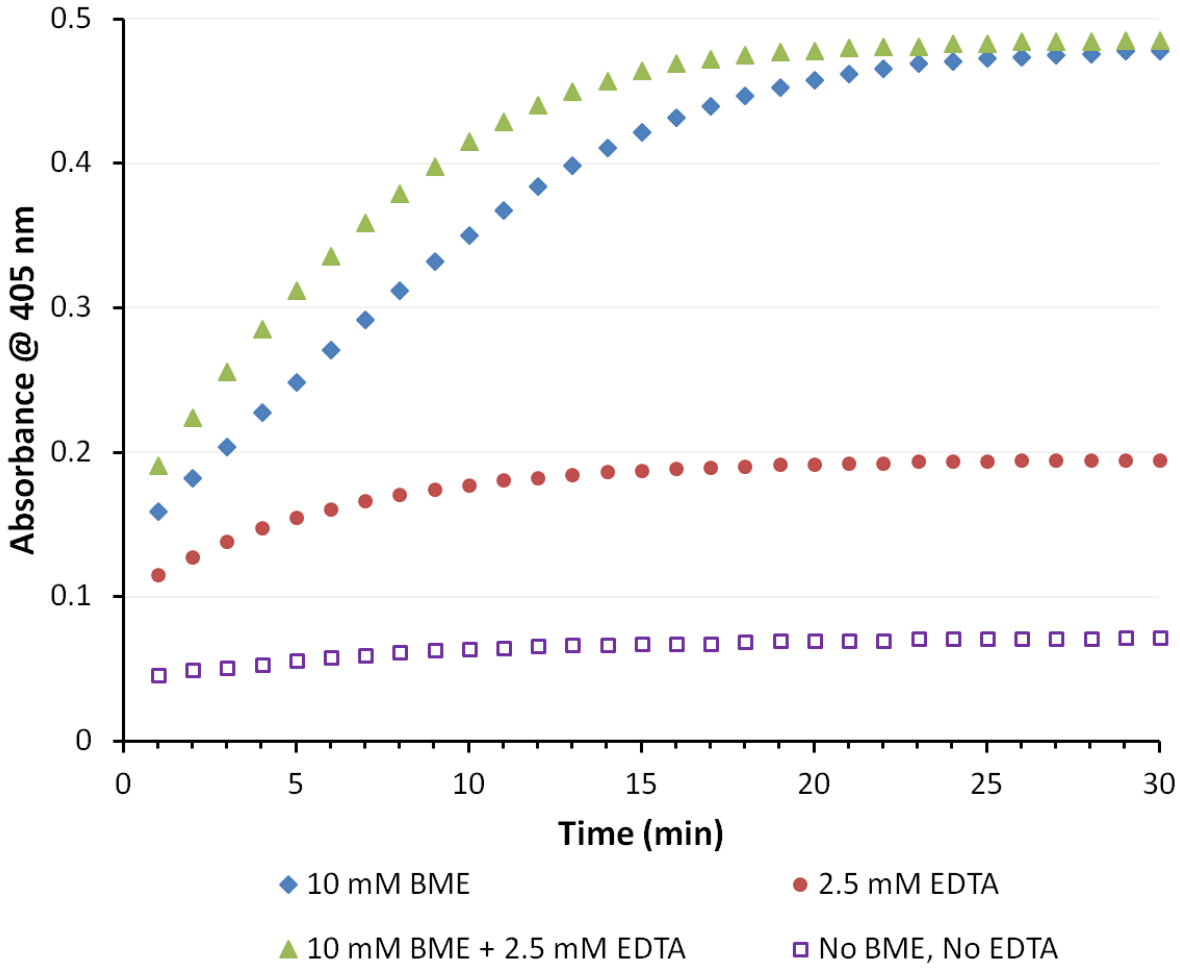

Figure 7.5. The requirement of chelating agent (EDTA) or reducing agent (BME) for the activity of caspase-3 purified from Ni – affinity column without further purification.

In order to obtain useful information from enzyme kinetics, conditions suitable for both the enzyme and zinc should be chosen. As many other enzymes, caspases have been shown to

perform better in the presence of reducing agents and other additives.[135] Indeed caspase-3 WT obtained from the Ni affinity column without further purification, required EDTA or BME to be active (Figure 7.5). Nevertheless, the zinc inhibition kinetics will be affected by their presence. Further thiol based reducing agents may directly interact with the thioester intermediate in the mechanism of caspases, thus altering the kinetics.[159] In fact, thiol based reducing agents may not be a good choice for enzymes that are dependent on cysteine for their activity. Hence, 50 mM Tris containing 100 mM NaCl at pH 7.4 was chosen as the minimal buffer to be used in all these studies. As done previously, the buffer was treated with Chelex® resin to eliminate any trace metal contaminants.[152]

During the initial trials, it was found that zinc inhibition of caspase-3 is immediate. Moreover, caspase-3 loses its activity over time as shown by a previous study.[160] Increase in temperature facilitates this deactivation. Hence, the incubation time was restricted to 15 min at room temperature in all the studies reported here.

7.6.3. Enzyme Kinetics Studies

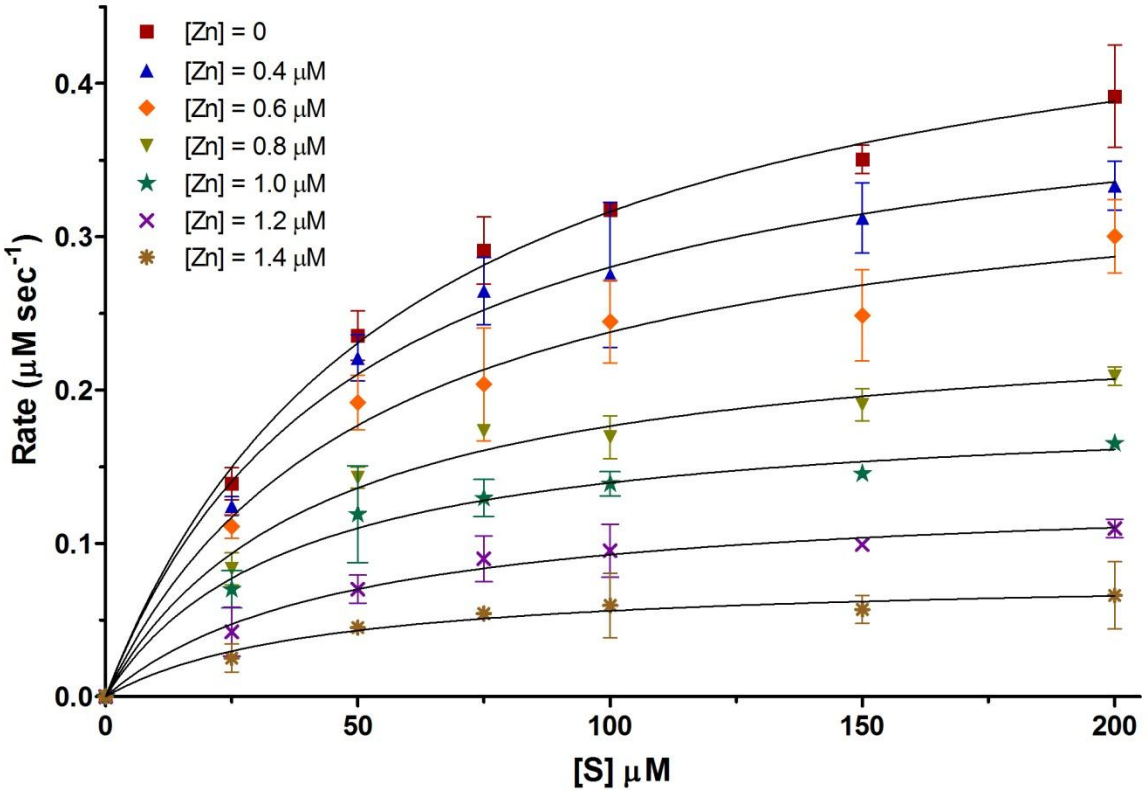

Figure 7.6. Michaelis – Menten plot of caspase-3 WT with various concentrations of Zn^{2+}. Mixed inhibition model was used to fit the data.

The rate of the reaction was plotted against various substrate concentrations to obtain a Michaelis – Menten plot (Figure 7.6). The analysis of the plot was done using enzyme kinetics nonlinear regression models in Graphpad Prism®. Among the enzyme inhibition models, using the mixed inhibition model provided the overall best fit. The kinetic parameters obtained from the fitting are shown in Table 7.1. Under these conditions the enzyme showed significant activity with k_{cat}/K_m = 0.50 x 10^6 $M^{-1}s^{-1}$, comparable or better than previously published results.[161-163]

Table 7.1. Kinetic parameters of Zn^{2+} inhibition enzyme kinetics obtained by fitting Michaelis – Menten plot (Figure 7.6) using mixed type inhibition model

[Zn] (μM)	V_{max}^{app} (μM s^{-1})	K_m^{app} (μM)
0	0.50 ± 0.02	59 ± 5
0.4	0.42 ± 0.02	50 ± 7
0.6	0.36 ± 0.03	52 ± 11
0.8	0.25 ± 0.01	42 ± 8
1.0	0.20 ± 0.01	37 ± 6
1.2	0.14 ± 0.01	47 ± 8
1.4	0.08 ± 0.01	42 ± 10

Under the conditions used, the IC_{50} of Zn^{2+} towards caspase-3 is found to be around 0.8 μM. In the range of 0.4 μM to 1.4 μM, V_{max}^{app} decreases with increasing concentration of Zn^{2+}, indicating a mechanism other than competitive inhibition. Up to 1 μM, the K_m^{app} value decreases, followed by an increase above 1 μM. Although the change in K_m value is not large, this reproducible trend indicates a sudden change in the mode of inhibition. The complexity involved in the inhibition is also apparent from the Lineweaver – Burk plot (Figure 7.7). The decrease in K_m^{app} in the sub- micromolar range along with a steady decrease in V_{max}^{app} resembles uncompetitive inhibition. However, above 1 μM, there is an obvious change in inhibition to noncompetitive type. The decreased K_m value indicates higher substrate affinity to caspase-3 in the presence of zinc. This suggests that substrate binding is unaffected even while Zn^{2+} binds to the inhibitory binding site.

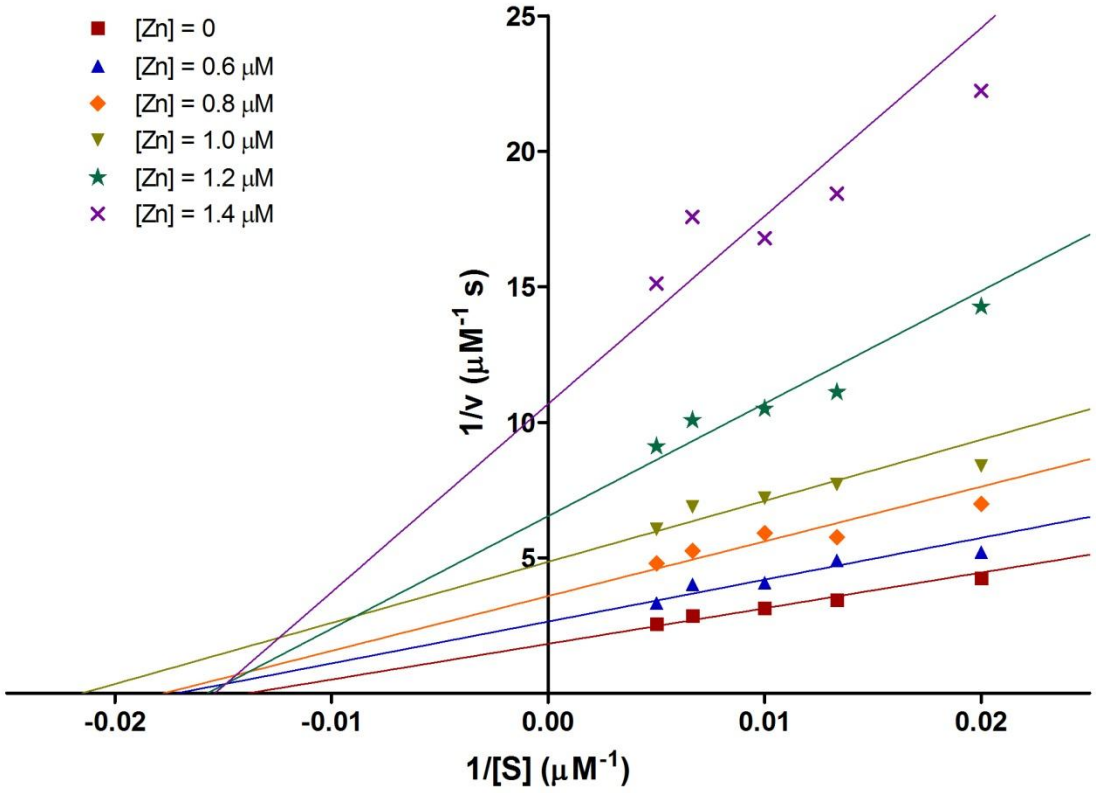

Figure 7.7. Lineweaver-Burk Plot of caspase-3 WT with various concentrations of Zn^{2+}. Up to 1μM the inhibition is competitive after which it changes to noncompetitive type inhibition.

Analysis of the dissociation constants K_i and K_i' obtained by fitting the Michaelis – Menton plot shows that K_i and K_i' which are different at low concentration of Zn^{2+}, approach equality as the concentration of Zn^{2+} is increased (Figure 7.8). The initial higher value of K_i compared to K_i' is once again supportive of uncompetitive type inhibition. Once again, this at least suggests unperturbed binding of substrate to the active site, if not higher affinity binding of substrate in the presence of zinc. With increase in the concentration of Zn^{2+}, the K_i value decreases and approaches the value of K_i', which implies a transition towards noncompetitive type inhibition. The existence of more than one zinc binding site in caspase-3 is speculated from

this analysis. This is consistent with the previous report using ICP-OES, which suggests the possibility of three Zn^{2+} ions binding per molecule of caspase-3. However, one of these sites was speculated to constitute the active site dyad which is to the contrary to what is inferred from this kinetics study.

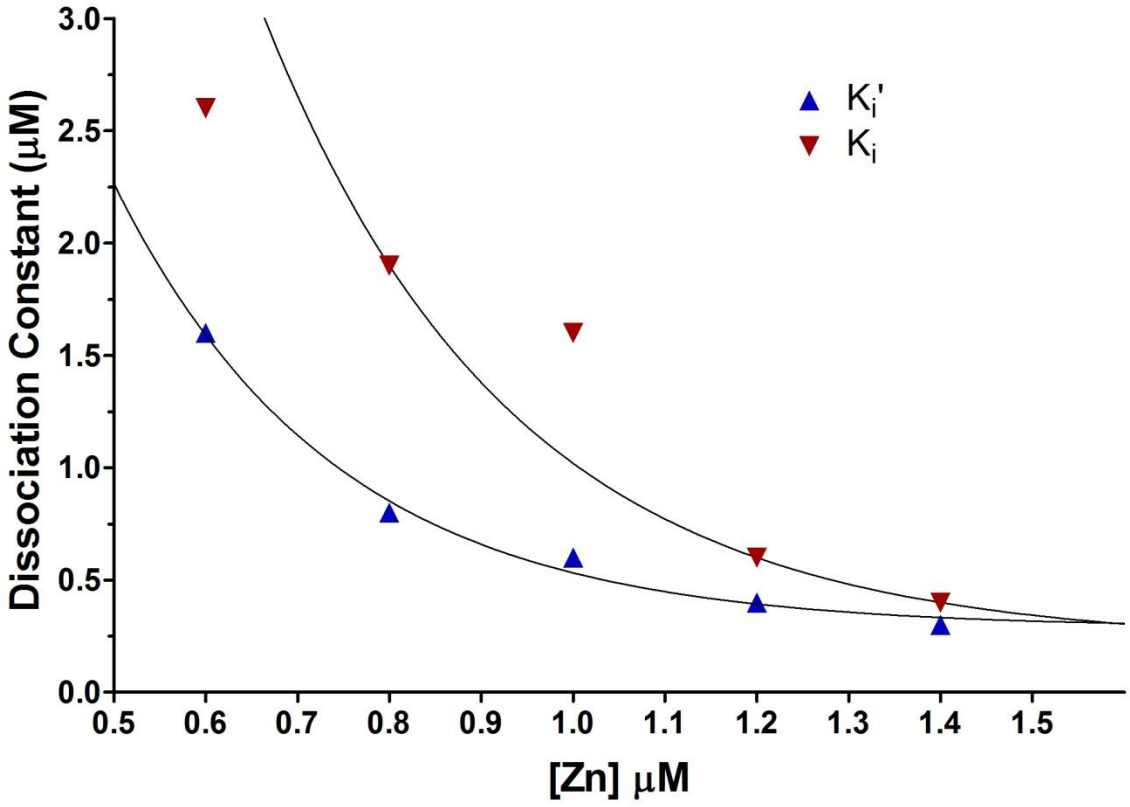

Figure 7.8. Change in dissociation constants of Zn^{2+} as a function of [Zn^{2+}], which indicates change in the mode of inhibition with varying [Zn^{2+}].

7.6.4. Fluorescence Polarization Studies

The substrate binding trend observed in the kinetics experiments needs further confirmation. For this purpose, a fluorescence polarization experiment was designed. A fluorescently tagged irreversible inhibitor, FITC-C6-DEVD-fmk, will be used as a substrate mimic and its binding caspase-3 will be monitored with varied concentration of Zn^{2+}.

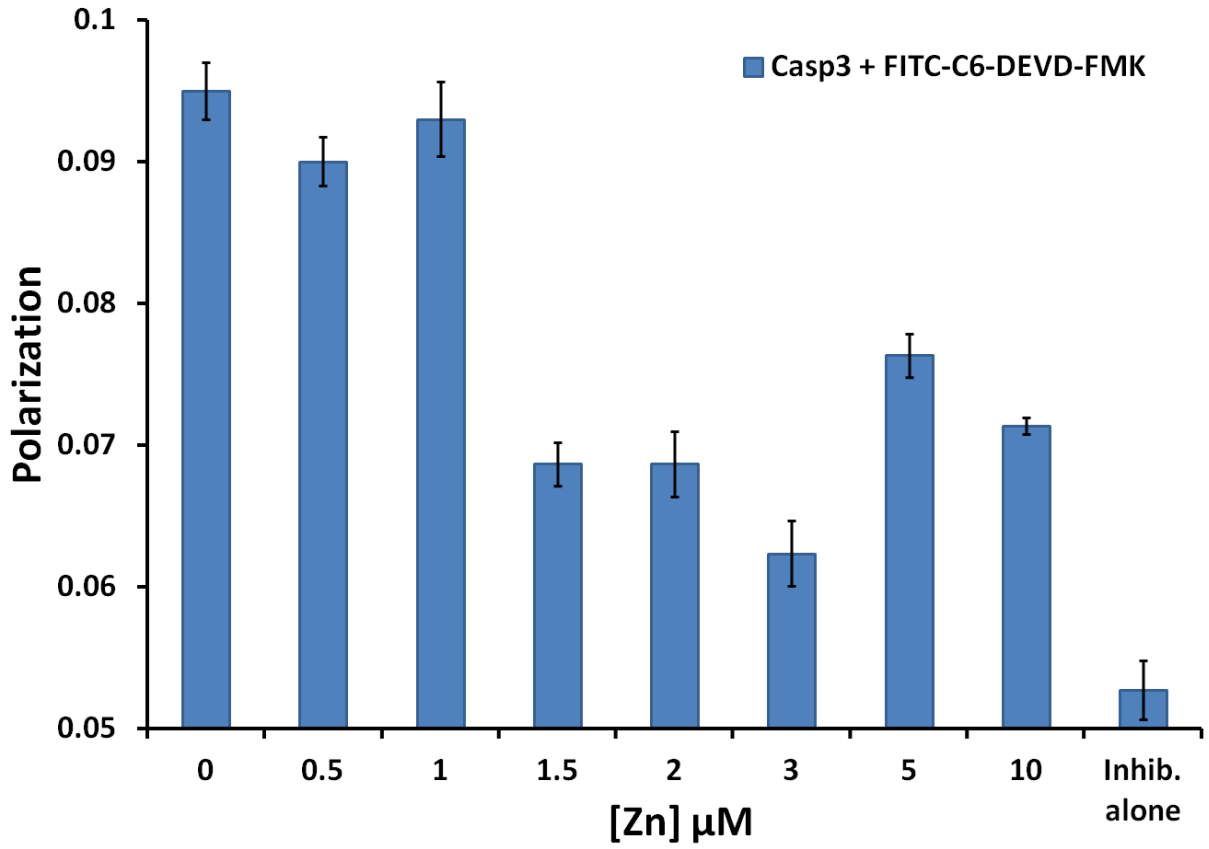

Figure 7.9. Effect of Zn^{2+} on substrate binding to caspase-3 WT observed by monitoring fluorescence polarization of a fluorescently tagged caspase-3 inhibitor, FITC-C6-DEV-fmk.

The fluorescence polarization experiment confirmed the trends in substrate binding affinity that were observed in the kinetics study. As seen from Figure 7.9, at up to 1 µM of Zn^{2+}, the fluorescence polarization remains unchanged, which indicates that the binding of the substrate to the enzyme is not affected by Zn^{2+} at these concentrations. At higher concentrations of Zn^{2+} there is significant decrease in the polarization values, which indicates reduced substrate binding. The increase in polarization seen at 5 µM and 10 µM might be due to nonspecific interactions in the presence of zinc, as the enzyme is totally inactive at these high concentrations. These results serve as a proof for the inference from kinetics studies that substrate binding to caspase-3 is not affected due to zinc binding at the inhibitory site.

7.6.5. Intrinsic Fluorescence Studies

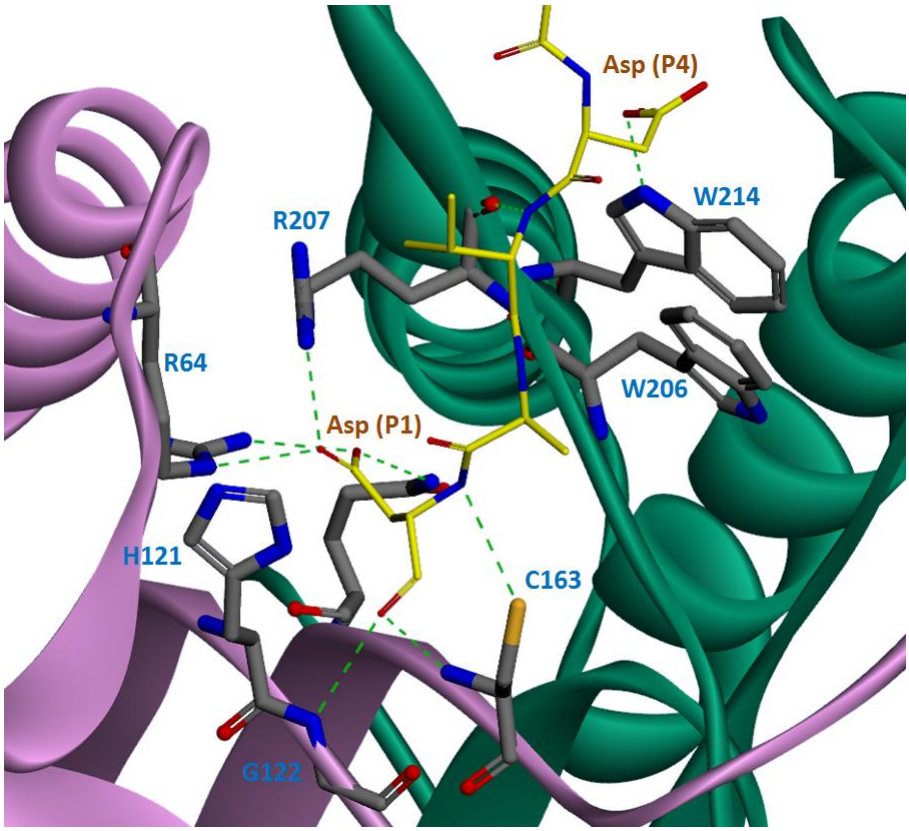

Figure 7.10. Active site of caspase-3 bound to an inhibitor (yellow stick): Two Trp residues which are closer to the active site along with other important residues are shown. The P4 residue of the inihbitor is in contact with Trp214.

Caspase-3 has two Trp residues (W206 and W214) near the substrate binding pocket (Figure 7.10). W214 is known to make contact with the P4 Asp on the substrate as it binds to the pocket. The change in fluorescence from these residues could be used to monitor perturbation around the active site during substrate binding.[164,165] The same may provide information about the change in local environment around the active site during zinc inhibition. Thus, monitoring the intrinsic fluorescence in the presence of zinc and/or a substrate analogous inhibitor (Ac-DEVD-CHO) would shed light on the local environment around the active site in the presence of these inhibitors.

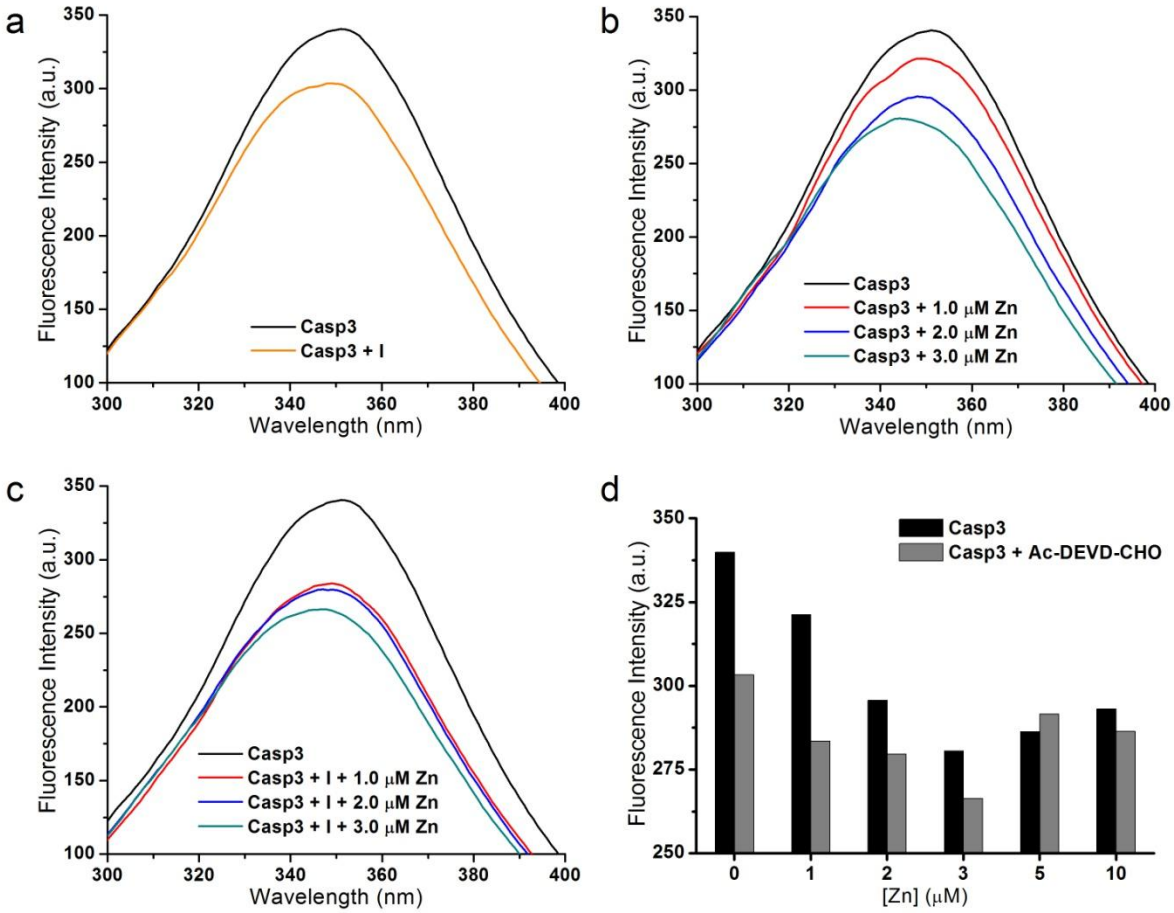

Figure 7.11. Fluorescence spectra of caspase-3 under various conditions: Fluorescence quenching of caspase-3 (1μM) by a) Ac-DEVD-CHO (I). b) 1-10 μM [Zn^{2+}] and c) a combination of Ac-DEVD-CHO and 1-10 μM [Zn^{2+}]. d) Fluorescence intensity at λ_{max} of caspase-3 with or without a reversible inhibitor under the influence of various [Zn^{2+}].

The quenching in caspase-3 fluorescence that results from the interaction of substrate is shown in Figure 7.11a. Further, just zinc by itself was seen to quench the fluorescence of caspase-3 (Figure 7.11b). Again, interaction of zinc with caspase-3 seems to vary with change in the concentration of zinc. Up to 2 μM of zinc, a small blue shift and decrease in fluorescence with a narrowing of the band was observed. At 3 μM of zinc, however, a bigger blue shift accompanied by a decrease in fluorescence and band broadening is observed. Above 3 μM of zinc, the band broadened further with a small blue shift but the intensity increased again. These

observations may be interpreted as direct interaction of zinc with the Trp residues or a result of change in solvation environment around the Trp residues due to zinc binding somewhere close by. This may again indicate existence of more than one zinc binding site with different binding affinities.

In another experiment, the fluorescence of caspase-3 was monitored in the presence of both the peptide inhibitor and various concentrations of zinc (Figure 7.11c). This would again help assess the effect of zinc on substrate binding to the caspase. Comparing the spectra with those where only zinc was used to produce the quenching, it can be seen that only at 1 µM of zinc the quenching is additive (Figure 7.11d). At higher concentrations, the quenching that is seen is mostly due to the perturbation by zinc. Since the peptidic inhibitor affects Trp214, the additivity leads to the speculation that zinc directly or indirectly affects the Trp206 and the same confirms that the binding of zinc and the substrate are independent up to 1 µM.

7.6.6. Circular Dichroism Studies

From the fluorescence studies it was inferred that zinc induces some change around the active site, which then affects the Trp fluorescence. In order to see if this change is part of a bigger change in the secondary structure of caspase-3, CD experiments were performed. Comparing the CD spectrum of caspase-3 alone with the spectrum of caspase-3 with zinc, no significant change can be noticed (Figure 7.12). Thus, it can be concluded that there is no global change in the structure of caspase in the presence of Zn^{2+} but only local changes.

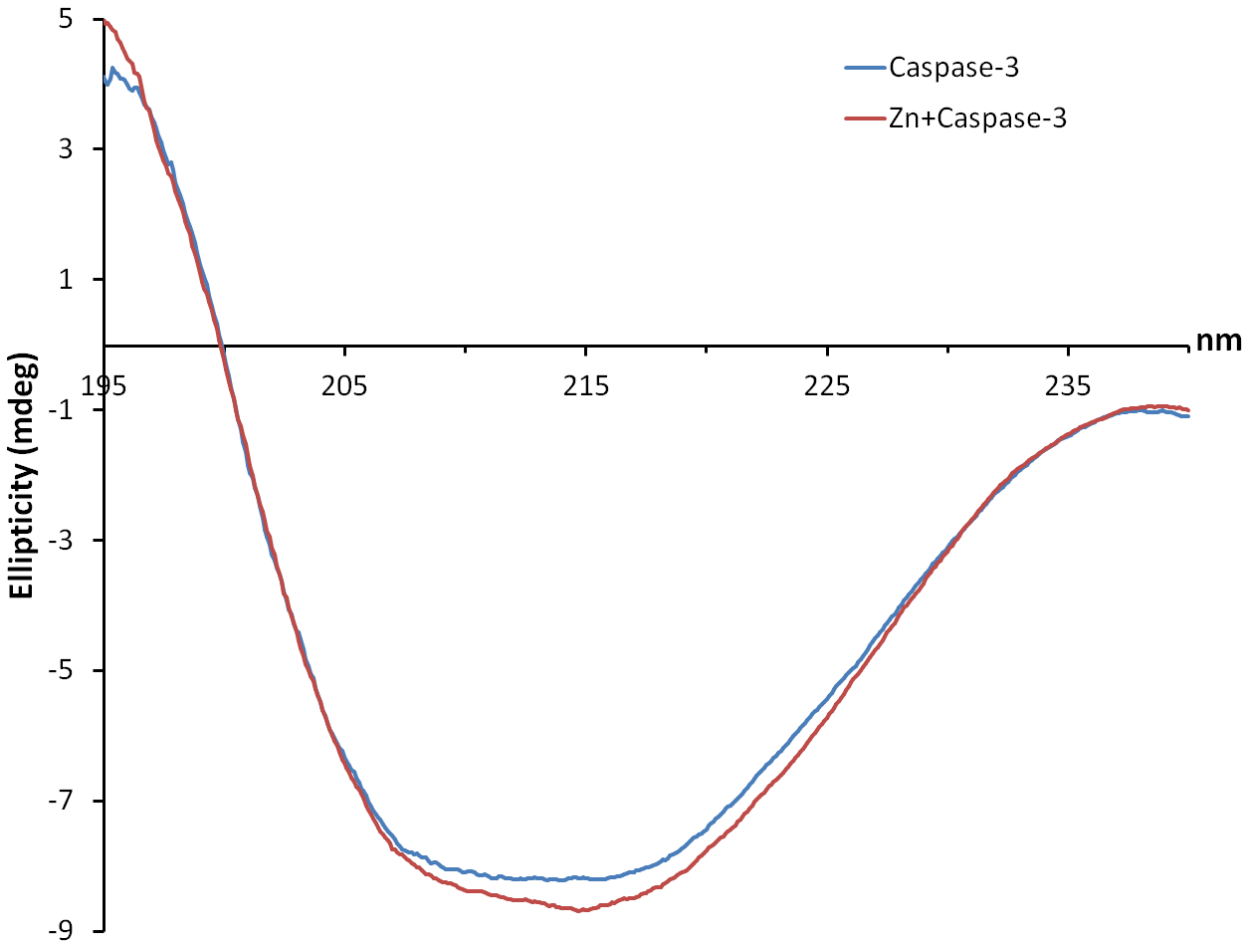

Figure 7.12. CD spectra of caspase-3 (20 µM) and caspase-3 with Zn^{2+} (10 µM). There is no significant change implying that zinc dose not induce noticeable change in secondary structure of caspase-3.

7.6.7. Prediction of Zinc Binding Site

From all of the above experiments, it is clear that concentration of zinc in the sub micromolar range, where more that 50% of the inhibition occurs, does not affect substrate binding to the caspase-3. Thus, the possibility of Zn^{2+} binding to the active site dyad is small. However, from fluorescence studies, it can be inferred that Zn^{2+} binds closer to the active site. Further, since zinc inhibition of caspase-3 is uncompetitive in the sub-micromolar range, the inhibition should be happening at a later stage, after the substrate binds to the active site.

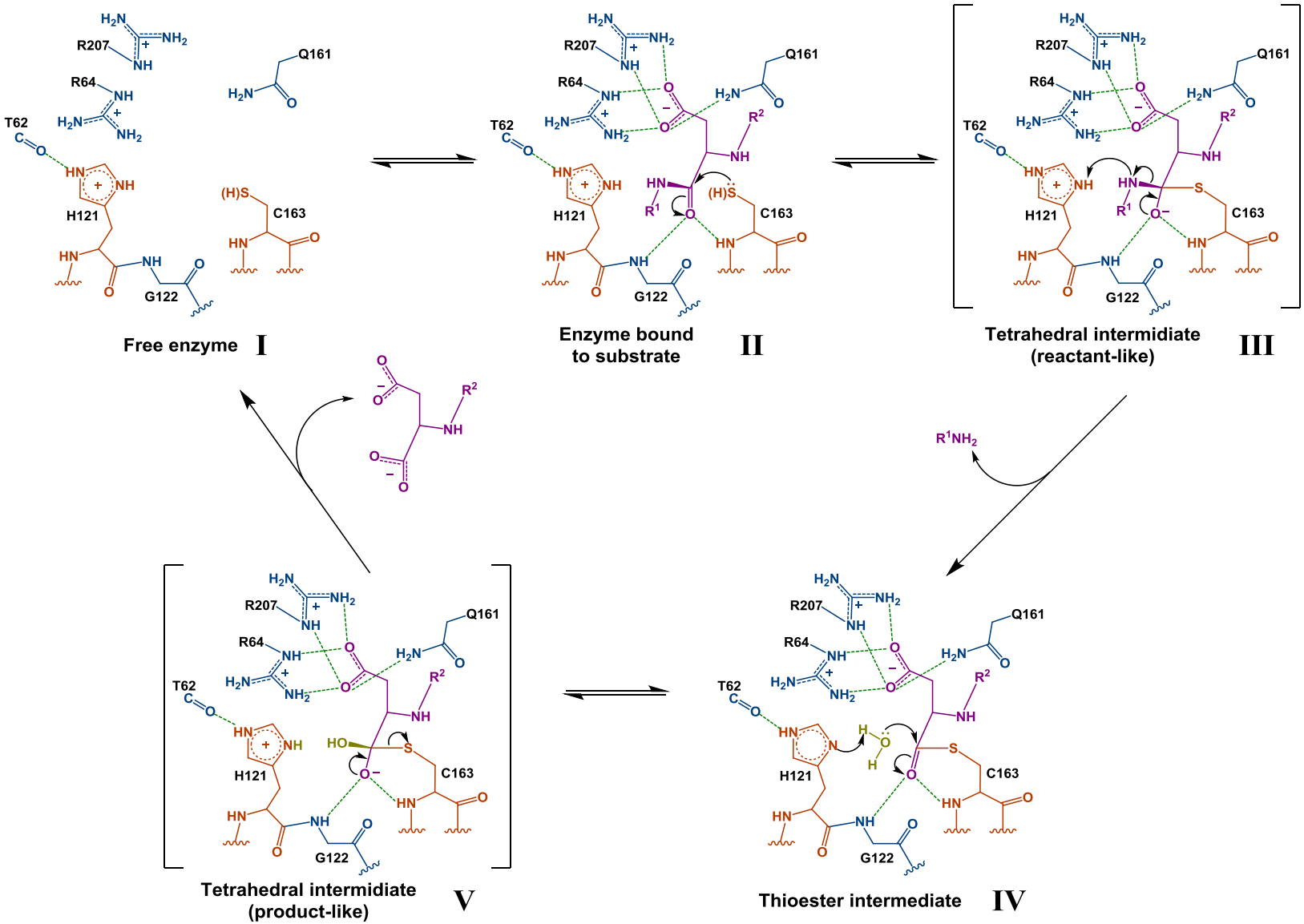

Figure 7.13. Mechanism of action of caspase-3: The residues involved and the mechanistic events are shown.

The mechanism of activity of caspase-3 involves five steps (Figure 7.13).[114] At first, the substrate binds to the active site pocket and is positioned by the recognition units (Figure 7.13 **II**). If zinc binds to the catalytic dyad and thus competes with the substrate, the inhibition would take place at this step. Following the recognition and positioning of the substrate, the sulfur of Cys163 is involved in a nucleophilic attack of the P1 carbonyl carbon, which is activated by the interaction in the oxyanion hole. This results in the formation of a tetrahedral intermediate that resembles the reactant (Figure 7.13 **III**). Facilitated by His121 acting as a general acid, the amino group of the scissile amide bond leaves as an amine. This leads to a rather stable thioester intermediate (Figure 7.13 **IV**), which may undergo slow hydrolysis if unassisted. However, the hydrolysis is assisted by His121 now acting as a general base, which would help polarize a water molecule involved in the hydrolysis. Eventually, a product-like tetrahedral intermediate (Figure 7.13 **V**) is formed which transforms into the product spontaneously by giving the free enzyme (Figure 7.13 **I**).

Considering the mechanism of proteolysis by caspases, this could be either at the stage where formation of thioester bond between the substrate and the enzyme occurs (Figure 7.13 **III**) or at the stage where the thioester is hydrolyzed to form the final product (Figure 7.13 **IV**). Both these steps are assisted by the His121 residue, which acts as a general acid or base as required. Zinc could inhibit the activity just by affecting the activity of the histidine by binding to the histidine alone or the histidine could be a part of a binding site that does not involve the catalytic cysteine. By investigating several crystal structures[116,124,153-156] of caspase-3, Met61, which was in close proximity to His121 (Figure 7.14), was chosen as a potential zinc binding ligand to make a binding site along with the histidine. Met61 is one of the hydrophobic residues from the L1 loop, which aids in positioning His121 in place and suitable for catalysis. Met61 is partially

conserved as Leu or Ile in all of the caspases and it is common to caspase-3 and 7. As this residue may be critical for the proper positioning, and thus the function of His121, the involvement of these residues in forming a zinc binding site may lead to the observed inhibition. Further, being part of the L1 loop, which is more flexible compared to the others (Figure 7.2), and methionine itself having a flexible side chain, it may offer the flexibility required to bind zinc.

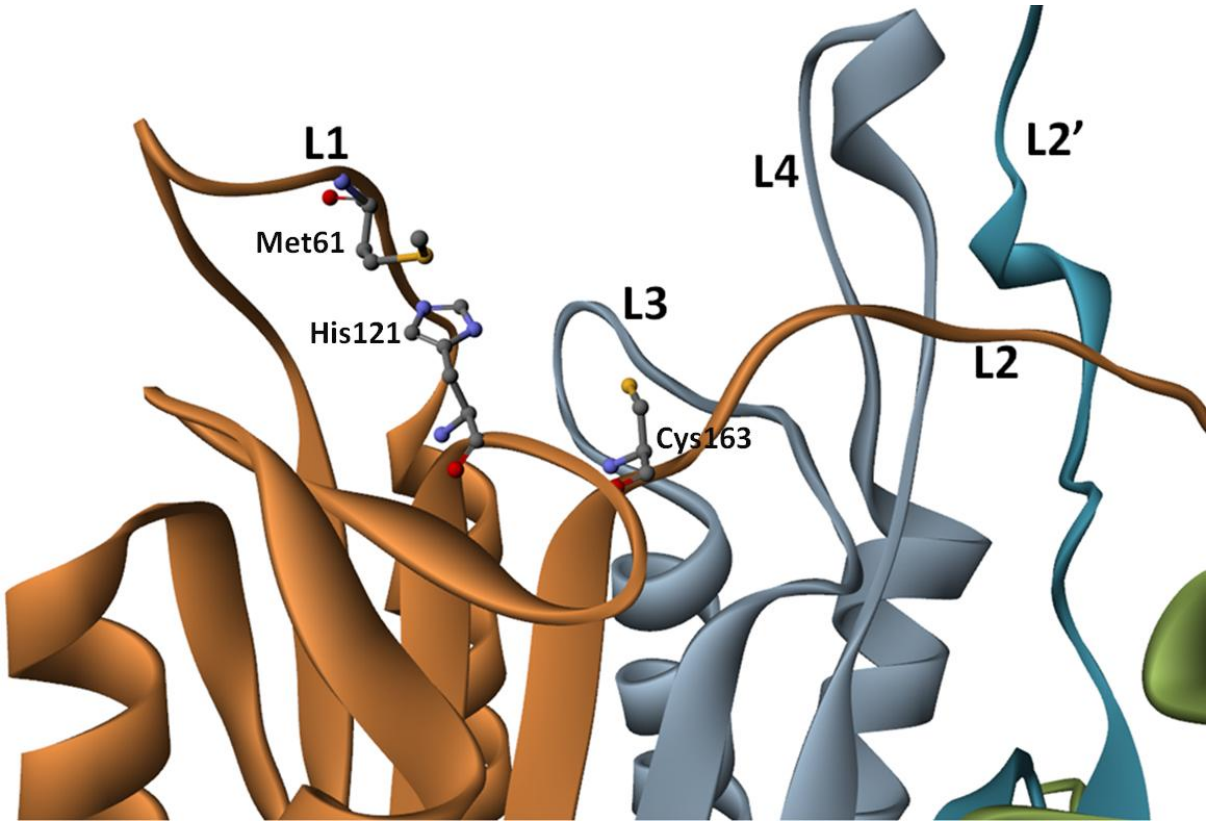

Figure 7.14. The position of Met61 which is proposed to make a zinc binding site together with His121 is shown. Met61 is part of the L1 loop which is flexible.[124]

7.6.8. DFT Modeling of the Zinc Binding Sites

Zinc binding to the catalytic dyad (ZnCH) and to the newly proposed site constituting the catalytic histidine and Met61 (ZnMH) were modeled and geometry optimized using DFT. The models for zinc binding sites were constructed from a crystal structure of caspase-3 (PDB ID: 1I3O)[124], in which the active site is not perturbed due to substrate binding. Ala163 in the crystal structure was changed to Cys163.

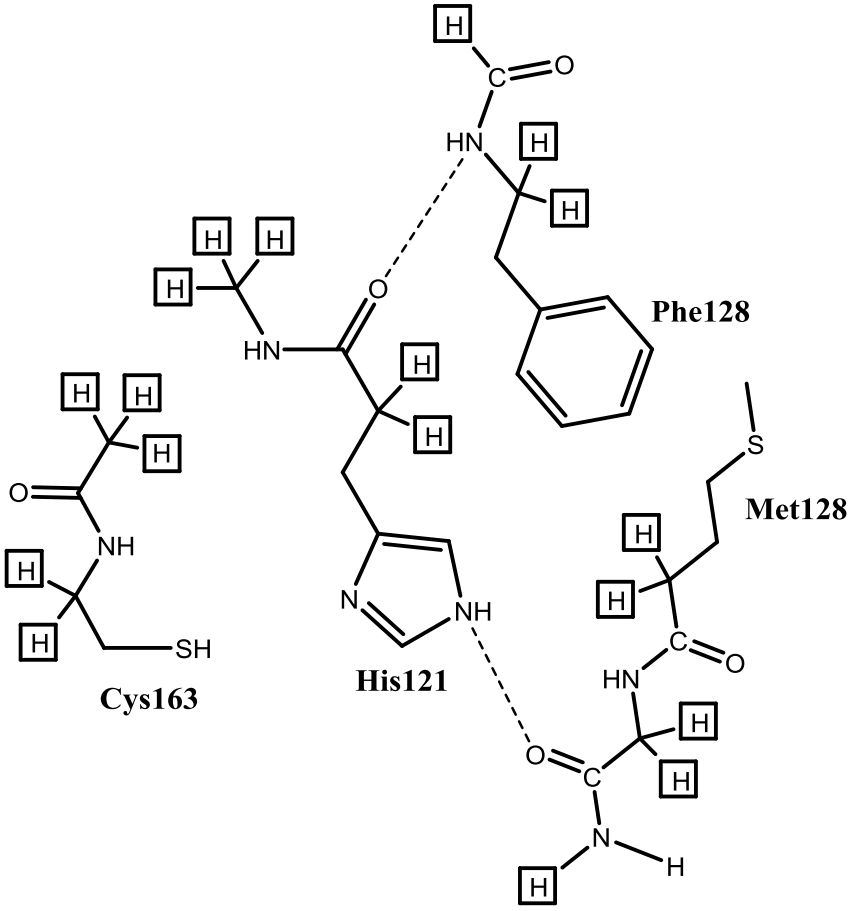

Figure 7.15. A 2D scheme of the residues used in modeling the zinc binding sites: the atoms that were fixed during the optimization to mimic the rigidity of the backbone are shown in boxes.

The models were built with consideration for stabilizing interactions and steric constraints. These consisted of truncated fragments of potential zinc ligands Met61, His121,

Cys163 and Phe128 which is in direct contact the Met or that may be sterically important. The coordination sphere of zinc was saturated with two water molecules as permitted by space. The positions of hydrogens on the α-carbons and a few other hydrogens were frozen in order to model the rigidity enforced by the backbone (Figure 7.15). The computations were performed at the PBE0/6-311G(3df, 2dp) level of theory with diffuse functions on sulfur atoms using Gaussian03.[100] As a consequence of fixing the position of hydrogens, the vibrational analysis resulted in a few small imaginary frequencies in the range of 10i to 50i, which predominantly involved atoms of the peptide backbone. The energies were corrected for BSSE using the Counterpoise method.[166]

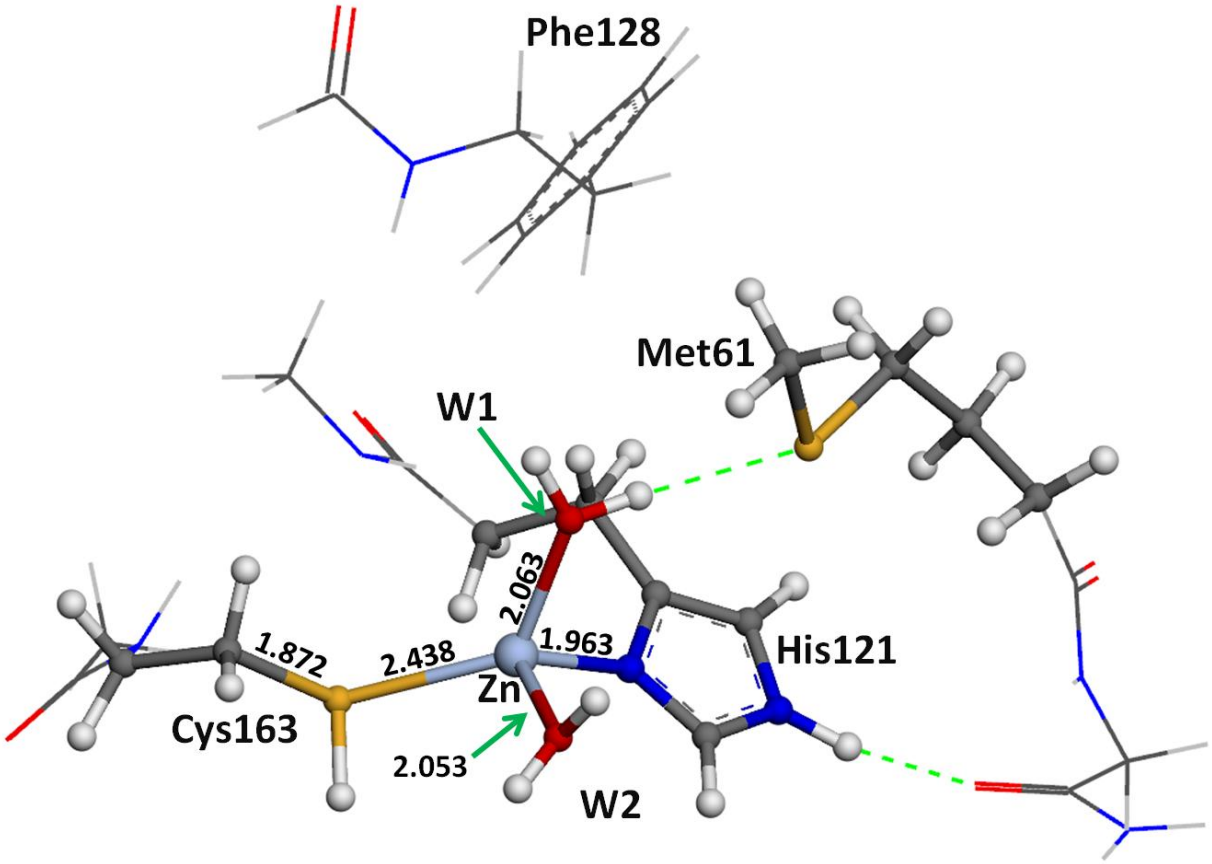

Figure 7.16. Geometry optimized structure of zinc bound to the catalytic dyad. Important bond lengths (Å) are shown. W1 and W2 are water molecules.

The optimized geometry of ZnCH site is a distorted tetrahedron with a Zn-S bond distance of 2.438 Å and the S-Zn-N bond angle being 126.6°. Zinc bound to His and the two water molecules with Zn-N bond length of 1.963 Å, Zn-O bond lengths of 2.053 Å and 2.063 Å, respectively (Figure 7.16).

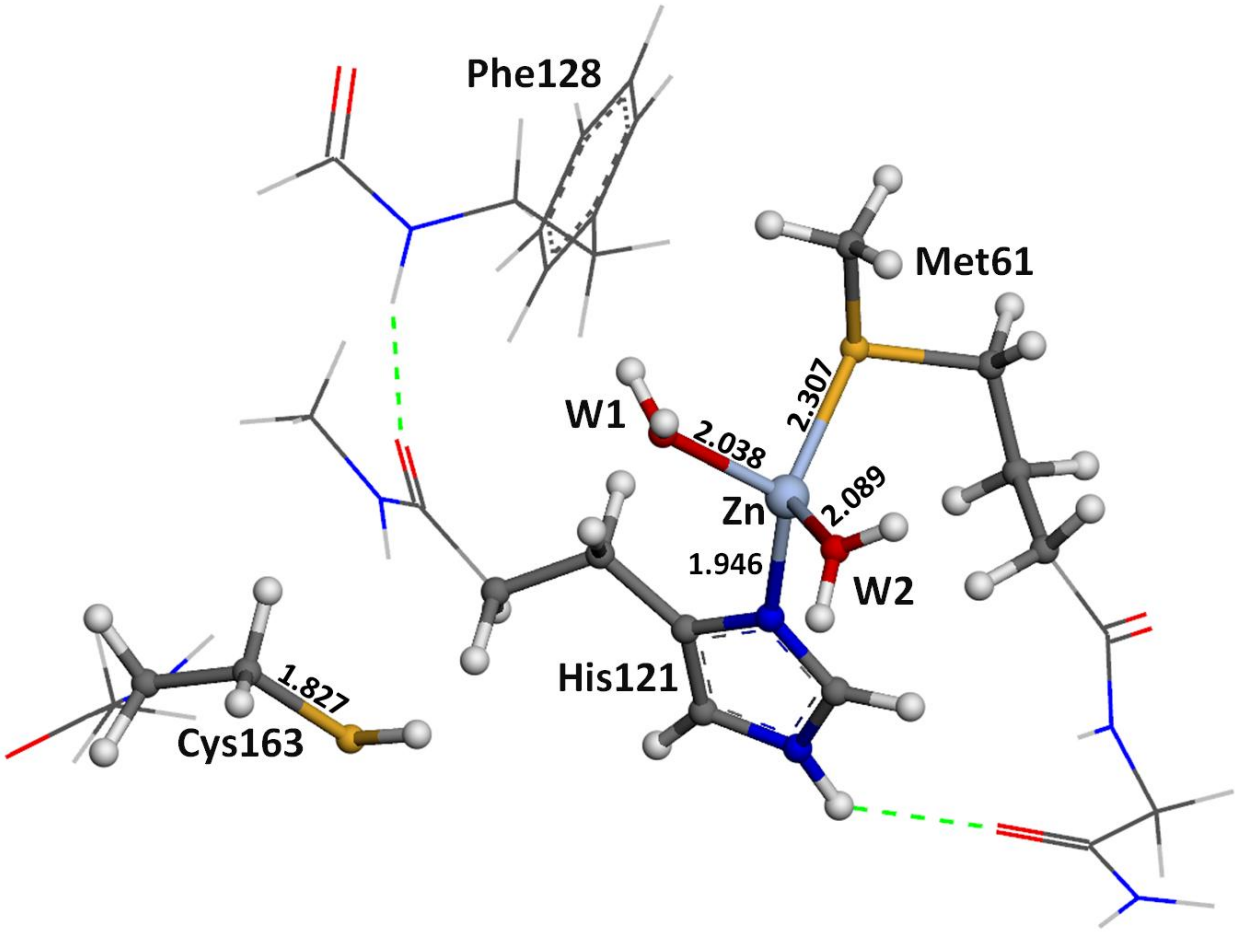

Figure 7.17. Geometry optimized structure of zinc bound to the newly proposed site constituting the catalytic histidine and Met61. Important bond lengths (Å) are shown. W1 and W2 are water molecules.

In the case of the ZnMH site, the Zn-S and Zn-N bond distances were 2.307 Å and 1.946 Å and S-Zn-N bond angle was 119.8°. Moreover, the ZnMH site was 11.0 kcal mol^{-1} more stable than the ZnCH site (Figure 7.17). The geometric parameters of these models are given in Table 7.2.

Table 7.2. Structural parameters of inhibitory Zn^{2+} binding sites modeled using DFT. Bond lengths in Å and bond angles in deg. W1 and W2 are water molecules.

	ZnCH site	ZnCH site C_α of Cys relaxed	ZnMH site
Zn-S	2.438	2.386	2.307
Zn-N	1.963	1.942	1.946
Zn-O (W1)	2.063	2.046	2.038
Zn-O (W2)	2.053	2.050	2.089
∠S-Zn-N	126.6	119.2	119.8
∠S-Zn-O (W1)	126.4	126.5	98.1
∠S-Zn-O (W2)	105.0	109.1	120.7
∠N-Zn-O (W1)	94.5	98.4	119.7
∠N-Zn-O (W2)	106.1	108.7	106.4
∠O-Zn-O	92.1	90.8	88.2

It should be noted that in ZnCH site the C_β-S bond of Cys163 is 1.872 Å, which is longer than normal. This might be an artifact arising due to fixing the positions of the hydrogens on the α-carbons, but such longer C-S bonds have been observed in a strained system.[167] Re-optimization of the ZnCH site with the hydrogens on the α-carbons released resulted in a better geometry. Notably, the Zn-S bond distance measured 2.385 Å, the C_β-S bond of Cys163 was 1.841 Å and the S-Zn-N bond length was 119.2°. Consequently, the system was stabilized by 8.7 kcal mol^{-1} compared to original ZnCH site. This illustrates that if Zn binds to the catalytic dyad, it would need a rearrangement of the backbone in order to bind tightly. Although movement of backbone atoms occurs during metal coordination in some proteins,[168] it may not be favored in the case of the catalytic Cys of active caspases because of the constraints discussed earlier. Similarly, the catalytic His, which is part of a β-sheet, is also rigid. However, the Met being part of the flexible L1 loop (Figure 7.2), with a long side chain may be more accommodative to zinc.

These considerations, along with the observed trends in energy and geometric parameters of these models, led us to conclude that the ZnMH site would be favored over the ZnCH site.

7.6.9 Consistency of the Proposed Site with Experimental Results

Considering the ZnMH site to be one of the inhibitory zinc binding sites, we evaluated how well it could help explain our experimental observations. Firstly, as zinc binds to the His–Met site, it induces a 90^{o} rotation around the C_{β}-C_{γ} bond of the His, flipping the imidazole ring away from the substrate binding groove. This is facilitated by the favorable σ-π interaction between a zinc bound water molecule, the methyl group on Met61 residue and Phe128. Interestingly, this flipping expands the substrate binding groove, and thus may increase substrate binding affinity by reducing steric hindrance. This is noticeable by examining the trends in the K_m^{app} and K_i' values from the kinetics studies. Further, as this complex is away from the Trp residues, the change in fluorescence intensities observed in the presence of zinc may be due to a change in the solvation environment ensuing zinc binding. Mechanistically, since the catalytic His is no longer capable of acting as a general acid or base in its zinc bound state, the inhibition would occur at the reactant-like tetrahedral intermediate stage (Figure 7.13 **III**) or more likely at the thioester intermediate stage (Figure 7.13 **IV**) of the catalytic cycle where the His plays a role. In light of these rationales, this inhibitory zinc site accounts for the uncompetitive-like inhibition of caspase-3 observed in the sub-micromolar range of zinc.

7.7. Conclusion

From the results of this study aimed at gaining molecular details of zinc inhibition of caspase-3, the following conclusions can be deduced:

More than one zinc inhibitory sites present in caspase-3 give rise to a complex type of inhibition. At least one of these sites is local to the active site. But the catalytic dyad is not the inhibitory zinc binding site because during the inhibition substrate binding is not affected. There is a great possibility that zinc produces the inhibition by affecting the function of catalytic histidine. Based on this hypothesis, the predicted inhibitory zinc binding site constituting catalytic histidine and a nearby methionine, supported by DFT modeling, consistently explains all the experimental observations.

8. Overall Conclusion

The studies presented here investigated the structural aspects of two less common zinc coordination environments. Some of the structures of the complexes studied here can be considered as the extreme cases that test the well known coordination flexibility of zinc. Here, zinc is seen to adapt to its ligand environment very well, resulting in structures ranging from highly distorted to well-organized geometries. However, for effective bonding, flexibility of the ligand is required. The huge variability seen in bond lengths between Zn^{2+} and ligating atoms suggests variable binding affinities. Coordination number of Zn^{2+} depends on its effective charge. Thus, as the number of strongly bound ligands increase, the coordination number decreases. Therefore, it may be possible to increase or decrease the coordination number of Zn^{2+} in a given structure by perturbing the effective bonding of the currently bound ligands.

List of References

1. Ivano, B.; Harry, B. G.; Edward, I. S.; Joan, S. V., Eds.; In *Biological Inorganic Chemistry. Structure and Reactivity.* WILEY-VCH Verlag: 2007; Vol. 46, pp 739.

2. Rosenzweig, A. C. Metallochaperones: bind and deliver. *Chem. Biol.* **2002**, *9*, 673-677.

3. Waldron, K. J.; Rutherford, J. C.; Ford, D.; Robinson, N. J. Metalloproteins and metal sensing. *Nature* **2009**, *460*, 823-830.

4. Dupont, C. L.; Butcher, A.; Valas, R. E.; Bourne, P. E.; Caetano-Anolles, G. History of biological metal utilization inferred through phylogenomic analysis of protein structures. *Proc. Natl. Acad. Sci. U. S. A.* **2010**, *107*, 10567-10572.

5. Irving, H.; Williams, R. J. P. Order of Stability of Metal Complexes. *Nature* **1948**, *162*, 746-747.

6. Fromme, P.; Grotjohann, I. Structure of Photosystems I and II. *Results Probl. Cell Differ.* **2008**, *45*, 33-72.

7. Crichton, R. R. *Biological Inorganinc Chemistry An Introduction;* Elsevier: Oxford, UK, **2008**, pp 369.

8. Yamasaki, S.; Sakata-Sogawa, K.; Hasegawa, A.; Suzuki, T.; Kabu, K.; Sato, E.; Kurosaki, T.; Yamashita, S.; Tokunaga, M.; Nishida, K.; Hirano, T. Zinc is a novel intracellular second messenger. *J. Cell Biol.* **2007**, *177*, 637-645.

9. Andreini, C.; Banci, L.; Bertini, I.; Rosato, A. Zinc through the three domains of life. *J. Proteome Res.* **2006**, *5*, 3173-3178.

10. Anzellotti, A. I.; Farrell, N. P. Zinc metalloproteins as medicinal targets. *Chem. Soc. Rev.* **2008**, *37*, 1629-1651.

11. Maret, W.; Jacob, C.; Vallee, B. L.; Fischer, E. H. Inhibitory sites in enzymes: zinc removal and reactivation by thionein. *Proc. Natl. Acad. Sci. U. S. A.* **1999**, *96*, 1936-1940.

12. Pearson, R. G. Hard and Soft Acids and Bases. *Journal of American Chemical Society* **1963**, *85*, 3533.

13. Trzaskowski, B.; Adamowicz, L.; Deymier, P. A. A theoretical study of zinc(II) interactions with amino acid models and peptide fragments. *J. Biol. Inorg. Chem.* **2008**, *13*, 133-137.

14. Vahrenkamp, H. Why does nature use zinc--a personal view. *Dalton Trans.* **2007**, *(42)*, 4751-4759.

15. Lee, Y. M.; Lim, C. Physical basis of structural and catalytic Zn-binding sites in proteins. *J. Mol. Biol.* **2008**, *379*, 545-553.

16. Iuchi, S.; Kuldell, N. *Zinc Finger Proteins: From Atomic Contact to Cellular Function.* Kluwer Academic: New York, **2005**, pp 276.

17. Sousa, S. F.; Lopes, A. B.; Fernandes, P. A.; Ramos, M. J. The Zinc proteome: a tale of stability and functionality *Dalton Trans.* **2009**, *38*, 7946-56.

18. Maret, W. Inhibitory zinc sites in enzymes. *Biometals* **2013**, *26*, 197-204.

19. Xue, Y.; Liljas, A.; Jonsson, B. H.; Lindskog, S. Structural analysis of the zinc hydroxide-Thr-199-Glu-106 hydrogen-bond network in human carbonic anhydrase II. *Proteins* **1993**, *17*, 93-106.

20. Bahnson, B. J.; Colby, T. D.; Chin, J. K.; Goldstein, B. M.; Klinman, J. P. A link between protein structure and enzyme catalyzed hydrogen tunneling. *Proc. Natl. Acad. Sci. U. S. A.* **1997**, *94*, 12797-12802.

21. Tamilselvi, A.; Mugesh, G. Zinc and antibiotic resistance: metallo-beta-lactamases and their synthetic analogues. *J. Biol. Inorg. Chem.* **2008**, *13*, 1039-1053.

22. Zhang, C. M.; Christian, T.; Newberry, K. J.; Perona, J. J.; Hou, Y. M. Zinc-mediated amino acid discrimination in cysteinyl-tRNA synthetase. *J. Mol. Biol.* **2003**, *327*, 911-917.

23. Christianson, D. W. Carboxypeptidase A. *Accounts of Chemical Research* **1989**, *22*, 62.

24. Vallee, B. L.; Auld, D. S. Active-site zinc ligands and activated H2O of zinc enzymes. *Proc. Natl. Acad. Sci. U. S. A.* **1990**, *87*, 220-224.

25. Auld, D. S. Zinc coordination sphere in biochemical zinc sites. *Biometals* **2001**, *14*, 271-313.

26. Parkin, G. Synthetic analogues relevant to the structure and function of zinc enzymes. *Chem. Rev.* **2004**, *104*, 699-767.

27. Elrod-Erickson, M.; Rould, M. A.; Nekludova, L.; Pabo, C. O. Zif268 protein-DNA complex refined at 1.6 A: a model system for understanding zinc finger-DNA interactions *Structure* **1996**, *4*, 1171-1180.

28. Lu, D.; Klug, A. Invariance of the zinc finger module: a comparison of the free structure with those in nucleic-acid complexes. *Proteins* **2007**, *67*, 508-512.

29. Yin, Q.; Lamothe, B.; Darnay, B. G.; Wu, H. Structural basis for the lack of E2 interaction in the RING domain of TRAF2. *Biochemistry* **2009**, *48*, 10558-10567.

30. Bates, D. L.; Chen, Y.; Kim, G.; Guo, L.; Chen, L. Crystal structures of multiple GATA zinc fingers bound to DNA reveal new insights into DNA recognition and self-association by GATA. *J. Mol. Biol.* **2008**, *381*, 1292-1306.

31. Krishna, S. S.; Majumdar, I.; Grishin, N. V. Structural classification of zinc fingers: survey and summary. *Nucleic Acids Res.* **2003**, *31*, 532-550.

32. Wolfe, S. A.; Nekludova, L.; Pabo, C. O. DNA recognition by Cys2His2 zinc finger proteins. *Annu. Rev. Biophys. Biomol. Struct.* **2000**, *29*, 183-212.

33. Fox, A. H.; Liew, C.; Holmes, M.; Kowalski, K.; Mackay, J.; Crossley, M. Transcriptional cofactors of the FOG family interact with GATA proteins by means of multiple zinc fingers *EMBO J.* **1999**, *18*, 2812-2822.

34. Polekhina, G.; House, C. M.; Traficante, N.; Mackay, J. P.; Relaix, F.; Sassoon, D. A.; Parker, M. W.; Bowtell, D. D. Siah ubiquitin ligase is structurally related to TRAF and modulates TNF-alpha signaling *Nat. Struct. Biol.* **2002**, *9*, 68-75.

35. Klug, A. The discovery of zinc fingers and their applications in gene regulation and genome manipulation. *Annu. Rev. Biochem.* **2010**, *79*, 213-231.

36. COLEMAN, J. E.; VALLEE, B. L. Metallocarboxypeptidases. *J. Biol. Chem.* **1960**, *235*, 390-395.

37. Bukrinsky, J. T.; Bjerrum, M. J.; Kadziola, A. Native carboxypeptidase A in a new crystal environment reveals a different conformation of the important tyrosine 248. *Biochemistry* **1998**, *37*, 16555-16564.

38. Maret, W.; Jacob, C.; Vallee, B. L.; Fischer, E. H. Inhibitory sites in enzymes: zinc removal and reactivation by thionein. *Proc. Natl. Acad. Sci. U. S. A.* **1999**, *96*, 1936-1940.

39. Maret, W. Optical methods for measuring zinc binding and release, zinc coordination environments in zinc finger proteins, and redox sensitivity and activity of zinc-bound thiols *Methods Enzymol.* **2002**, *348*, 230-237.

40. Henehan, C. J.; Pountney, D. L.; Zerbe, O.; Vasak, M. Identification of cysteine ligands in metalloproteins using optical and NMR spectroscopy: cadmium-substituted rubredoxin as a model [Cd(CysS)4]2- center *Protein Sci.* **1993**, *2*, 1756-1764.

41. Maret, W.; Li, Y. Coordination dynamics of zinc in proteins. *Chem. Rev.* **2009**, *109*, 4682-4707.

42. Chiou, S. J.; Riordan, C. G.; Rheingold, A. L. Synthetic modeling of zinc thiolates: quantitative assessment of hydrogen bonding in modulating sulfur alkylation rates *Proc. Natl. Acad. Sci. U. S. A.* **2003**, *100*, 3695-3700.

43. Picot, D.; Ohanessian, G.; Frison, G. The alkylation mechanism of zinc-bound thiolates depends upon the zinc ligands *Inorg. Chem.* **2008**, *47*, 8167-8178.

44. Lin, Y.; Dotsch, V.; Wintner, T.; Peariso, K.; Myers, L. C.; Penner-Hahn, J. E.; Verdine, G. L.; Wagner, G. Structural basis for the functional switch of the E. coli Ada protein *Biochemistry* **2001**, *40*, 4261-4271.

45. Ermler, U.; Grabarse, W.; Shima, S.; Goubeaud, M.; Thauer, R. K. Crystal structure of methyl-coenzyme M reductase: the key enzyme of biological methane formation *Science* **1997**, *278*, 1457-1462.

46. Matthews, R. G. Cobalamin-dependent methyltransferases *Acc. Chem. Res.* **2001**, *34*, 681-689.

47. Huang, M.; Maynard, A.; Turpin, J. A.; Graham, L.; Janini, G. M.; Covell, D. G.; Rice, W. G. Anti-HIV agents that selectively target retroviral nucleocapsid protein zinc fingers without affecting cellular zinc finger proteins. *J. Med. Chem.* **1998**, *41*, 1371-1381.

48. Morellet, N.; Jullian, N.; De Rocquigny, H.; Maigret, B.; Darlix, J. L.; Roques, B. P. Determination of the structure of the nucleocapsid protein NCp7 from the human immunodeficiency virus type 1 by 1H NMR. *EMBO J.* **1992**, *11*, 3059-3065.

49. de Rocquigny, H.; Shvadchak, V.; Avilov, S.; Dong, C. Z.; Dietrich, U.; Darlix, J. L.; Mely, Y. Targeting the viral nucleocapsid protein in anti-HIV-1 therapy. *Mini Rev. Med. Chem.* **2008**, *8*, 24-35.

50. Vuilleumier, C.; Bombarda, E.; Morellet, N.; Gerard, D.; Roques, B. P.; Mely, Y. Nucleic acid sequence discrimination by the HIV-1 nucleocapsid protein NCp7: a fluorescence study. *Biochemistry* **1999**, *38*, 16816-16825.

51. Bourbigot, S.; Ramalanjaona, N.; Boudier, C.; Salgado, G. F.; Roques, B. P.; Mely, Y.; Bouaziz, S.; Morellet, N. How the HIV-1 nucleocapsid protein binds and destabilises the (-)primer binding site during reverse transcription. *J. Mol. Biol.* **2008**, *383*, 1112-1128.

52. Musah, R. A. The HIV-1 nucleocapsid zinc finger protein as a target of antiretroviral therapy. *Curr. Top. Med. Chem.* **2004**, *4*, 1605-1622.

53. Bombarda, E.; Cherradi, H.; Morellet, N.; Roques, B. P.; Mely, Y. Zn(2+) binding properties of single-point mutants of the C-terminal zinc finger of the HIV-1 nucleocapsid protein: evidence of a critical role of cysteine 49 in Zn(2+) dissociation. *Biochemistry* **2002**, *41*, 4312-4320.

54. Hathout, Y.; Fabris, D.; Han, M. S.; Sowder, R. C.,2nd; Henderson, L. E.; Fenselau, C. Characterization of intermediates in the oxidation of zinc fingers in human immunodeficiency virus type 1 nucleocapsid protein P7. *Drug Metab. Dispos.* **1996**, *24*, 1395-1400.

55. Maynard, A. T.; Huang, M.; Rice, W. G.; Covell, D. G. Reactivity of the HIV-1 nucleocapsid protein p7 zinc finger domains from the perspective of density-functional theory. *Proc. Natl. Acad. Sci. U. S. A.* **1998**, *95*, 11578-11583.

56. Miller Jenkins, L. M.; Hara, T.; Durell, S. R.; Hayashi, R.; Inman, J. K.; Piquemal, J. P.; Gresh, N.; Appella, E. Specificity of acyl transfer from 2-mercaptobenzamide thioesters to the HIV-1 nucleocapsid protein. *J. Am. Chem. Soc.* **2007**, *129*, 11067-11078.

57. Jenkins, L. M.; Byrd, J. C.; Hara, T.; Srivastava, P.; Mazur, S. J.; Stahl, S. J.; Inman, J. K.; Appella, E.; Omichinski, J. G.; Legault, P. Studies on the mechanism of inactivation of the HIV-1 nucleocapsid protein NCp7 with 2-mercaptobenzamide thioesters. *J. Med. Chem.* **2005**, *48*, 2847-2858.

58. Sartori, D. A.; Miller, B.; Biebach, U.; Farrell, N. Modulation of the chemical and biological properties of trans platinum complexes: monofunctional platinum complexes containing one nucleobase as potential antiviral chemotypes. *J. Biol. Inorg. Chem.* **2000**, *5*, 575-583.

59. Anzellotti, A. I.; Liu, Q.; Bloemink, M. J.; Scarsdale, J. N.; Farrell, N. Targeting retroviral Zn finger-DNA interactions: a small-molecule approach using the electrophilic nature of trans-platinum-nucleobase compounds. *Chem. Biol.* **2006**, *13*, 539-548.

60. de Paula, Q. A.; Mangrum, J. B.; Farrell, N. P. Zinc finger proteins as templates for metal ion exchange: Substitution effects on the C-finger of HIV nucleocapsid NCp7 using M(chelate) species (M=Pt, Pd, Au) *J. Inorg. Biochem.* **2009**, *103*, 1347-1354.

61. Almaraz, E.; de Paula, Q. A.; Liu, Q.; Reibenspies, J. H.; Darensbourg, M. Y.; Farrell, N. P. Thiolate bridging and metal exchange in adducts of a zinc finger model and Pt(II) complexes: biomimetic studies of protein/Pt/DNA interactions *J. Am. Chem. Soc.* **2008**, *130*, 6272-6280.

62. Young, D. C. *Computational Chemistry A Practical Guide for Applying Techniques to Real-World Problems;* John Wiley & Sons, Inc.: New York, NY, **2001**, pp 370.

63. Thijssen, J. M. *Computational Physics;* Cambridge University Press: Cambridge, UK, **2007**, pp 621.

64. Born, M.; Oppenheimer, R. Zur Quantentheorie der Molekeln. *Annalen der Physik, Ann. Phys.* **1927**, *389*, 457.

65. Schrodinger, E. An undualtory theory of the mechanics of atoms and molecules. *The Physical Review* **1926**, *28*, 1049.

66. Parr, R. G.; Yang, W. *Density-Functional Theory of Atoms and Molecules;* Oxford University Press: Cary, NC, USA, **1994**, pp 344.

67. Lieb, E. H.; Simon, B. The Hartree-Fock theory for Coulomb systems *Communications in Mathematical Physics* **1977**, *53*, 185-194.

68. Slater, J. Note on Hartree's Method *Physical Review* **1930**, *35*, 210-211.

69. Frank, J. *Introduction to Computational Chemistry;* John Wiley & Sons Ltd: West Sussex, UK, **2007**, pp 599.

70. Cramer, C. J.; Truhlar, D. G. Density functional theory for transition metals and transition metal chemistry *Physical Chemistry Chemical Physics* **2009**, *11*, 10757.

71. Kohn, W.; Becke, A. D.; Parr, R. G. Density Functional Theory of Electronic Structure *J. Phys. Chem.* **1996**, *100*, 12974-12980.

72. Hohenberg, P. Inhomogeneous Electron Gas *Physical Review* **1964**, *136*, B864- B871.

73. Kohn, W.; Sham, L. J. Self-Consistent Equations Including Exchange and Correlation Effects *Physical Review* **1965**, *140*, A1133-A1138.

74. Lieb, E. H.; Simon, B. The Thomas-Fermi theory of atoms, molecules and solids *Advances in Mathematics* **1977**, *23*, 22-116.

75. Vosko, S. H.; Wilk, L.; Nusair, M. Accurate spin-dependent electron liquid correlation energies for local spin density calculations: a critical analysis *Can. J. Phys.* **1980**, *58*, 1200-1211.

76. Perdew, J. P.; Wang, Y. Accurate and simple analytic representation of the electron-gas correlation energy *Physical Review B* **1992**, *45*, 13244-13249.

77. Becke, A. D. Density-functional exchange-energy approximation with correct asymptotic behavior *Physical Review A* **1988**, *38*, 3098-3100.

78. Perdew, J. Density-functional approximation for the correlation energy of the inhomogeneous electron gas *Physical Review B* **1986**, *33*, 8822-8824.

79. Lee, C.; Yang, W.; Parr, R. G. Development of the Colle-Salvetti correlation-energy formula into a functional of the electron density *Physical Review B* **1988**, *37*, 785-789.

80. Perdew, J. P.; Jackson, K. A.; Pederson, M. R.; Singh, D. J.; Fiolhais, C. Atoms, molecules, solids, and surfaces: Applications of the generalized gradient approximation for exchange and correlation *Physical Review B* **1992**, *46*, 6671-6687.

81. Perdew, J. P.; Burke, K.; Ernzerhof, M. Generalized Gradient Approximation Made Simple *Phys. Rev. Lett.* **1996**, *77*, 3865-3868.

82. Adamo, C.; Barone, V. Exchange functionals with improved long-range behavior and adiabatic connection methods without adjustable parameters: The mPW and mPW1PW models *J. Chem. Phys.* **1998**, *108*, 664.

83. Becke, A. D. Density-functional thermochemistry. III. The role of exact exchange *J. Chem. Phys.* **1993**, *98*, 5648.

84. Adamo, C.; Barone, V. Toward reliable density functional methods without adjustable parameters: The PBE0 model *J. Chem. Phys.* **1999**, *110*, 6158.

85. Slater, J. Atomic Shielding Constants *Physical Review* **1930**, *36*, 57-64.

86. Boys, S. F. Electronic Wave Functions. I. A General Method of Calculation for the Stationary States of Any Molecular System *Proceedings of the Royal Society A: Mathematical, Physical and Engineering Sciences* **1950**, *200*, 542-554.

87. Ditchfield, R. Self-Consistent Molecular-Orbital Methods. IX. An Extended Gaussian-Type Basis for Molecular-Orbital Studies of Organic Molecules *J. Chem. Phys.* **1971**, *54*, 724.

88. Schultz, N. E.; Zhao, Y.; Truhlar, D. G. Density Functionals for Inorganometallic and Organometallic Chemistry *The Journal of Physical Chemistry A* **2005**, *109*, 11127-11143.

89. Harrison, J. F. Electronic Structure of Diatomic Molecules Composed of a First-Row Transition Metal and Main-Group Element (H-F) *Chem. Rev.* **2000**, *100*, 679-716.

90. Gill, P. M. W. A new gradient-corrected exchange functional. *Molecular physics, Mol. Phys.* **1996**, *89*, 433-445.

91. Notni, J.; Görls, H.; Anders, E. Zinc Thiolate Complexes [ZnLn(SR)]+ with Azamacrocyclic Ligands: Synthesis and Structural Properties *European Journal of Inorganic Chemistry* **2006**, *2006*, 1444-1455.

92. Bhattacharyya, S.; Kumar, S. B.; Dutta, S. K.; Tiekink, E. R. T.; Chaudhury, M. Zinc(II) and Copper(II) Complexes of Pentacoordinating (N4S) Ligands with Flexible Pyrazolyl Arms: Syntheses, Structure, and Redox and Spectroscopic Properties *Inorg. Chem.* **1996**, *35*, 1967-1973.

93. Moloto, N.; Revaprasadu, N.; Moloto, M. J.; O'Brien, P.; Raftery, J. N,N'-diisopropylthiourea and N,N'-dicyclohexylthiourea zinc(II) complexes as precursors for the synthesis of ZnS nanoparticles. *South African Journal of Science, S. Afr. J. Sci.* **2009**, *105*, 258.

94. Williams, D. J.; Ly, T. A.; Mudge, J. W.; Pennington, W. T.; Schimek, G. L. Dichlorobis[1-methyl-3-(prop-2-enyl)imidazole-2(3H)-thione-S]zinc(II) *Acta Crystallographica Section C Crystal Structure Communications* **1997**, *53*, 415-416.

95. Cavalca, L.; Nardelli, M.; Branchi, G. The crystal structure of monothiosemicarbazide-zinc chloride *Acta Crystallogr.* **1960**, *13*, 688-693.

96. Kunchur, N. R.; Truter, M. R. 701. The crystal structure of dichlorobisthioureazinc *Journal of the Chemical Society (Resumed)* **1958**, 3478.

97. Ben Gharbia, I.; Kefi, R.; El Glaoui, M.; Jeanneau, E.; Ben Nasr, C. 1-(4-Chloro-phenyl)piperazine-1,4-diium tetra-chlorido-zincate(II) monohydrate *Acta Crystallogr. Sect. E. Struct. Rep. Online* **2008**, *64*, m880.

98. Ajibade, P. A.; Zulu, N. H. Metal complexes of diisopropylthiourea: synthesis, characterization and antibacterial studies *Int. J. Mol. Sci.* **2011**, *12*, 7186-7198.

99. Peters, M. B.; Yang, Y.; Wang, B.; Fusti-Molnar, L.; Weaver, M. N.; Merz, K. M.,Jr Structural Survey of Zinc Containing Proteins and the Development of the Zinc AMBER Force Field (ZAFF). *J. Chem. Theory Comput.* **2010**, *6*, 2935-2947.

100. Gaussian 03, Revision D.02, Frisch, M. J.; Trucks, G. W.; Schlegel, H. B.; Scuseria, G. E.; Robb, M. A.; Cheeseman, J. R.; Montgomery, J., J. A.; Vreven, T.; Kudin, K. N.; Burant, J. C.; Millam, J. M.; Iyengar, S. S.; Tomasi, J.; Barone, V.; Mennucci, B.; Cossi, M.; Scalmani, G.; Rega, N.; Petersson, G. A.; Nakatsuji, H.; Hada, M.; Ehara, M.; Toyota, K.; Fukuda, R.; Hasegawa, J.; Ishida, M.; Nakajima, T.; Honda, Y.; Kitao, O.; Nakai, H.; Klene, M.; Li, X.; Knox, J. E.; Hratchian, H. P.; Cross, J. B.; Bakken, V.; Adamo, C.; Jaramillo, J.; Gomperts, R.; Stratmann, R. E.; Yazyev, O.; Austin, A. J.; Cammi, R.; Pomelli, C.; Ochterski, J. W.; Ayala, P. Y.; Morokuma, K.; Voth, G. A.; Salvador, P.; Dannenberg, J. J.; Zakrzewski, V. G.; Dapprich, S.; Daniels, A. D.; Strain, M. C.; Farkas, O.; Malick, D. K.; Rabuck, A. D.; Raghavachari, K.; Foresman, J. B.; Ortiz, J. V.; Cui, Q.; Baboul, A. G.; Clifford, S.; Cioslowski, J.; Stefanov, B. B.; Liu, G.; Liashenko, A.; Piskorz, P.; Komaromi, I.; Martin, R. L.; Fox, D. J.; Keith, T.; Al-Laham, M. A.; Peng, C. Y.; Nanayakkara, A.; Challacombe, M.; Gill, P. M. W.; Johnson, B.; Chen, W.; Wong, M. W.; Gonzalez, C.; and Pople, J. A. Gaussian, Inc., Wallingford CT, **2004**.

101. Dudev, T.; Lim, C. Modeling Zn2+-Cysteinate Complexes in Proteins *The Journal of Physical Chemistry B* **2001**, *105*, 10709-10714.

102. Topol, I. A.; Nemukhin, A. V.; Dobrogorskaya, Y. I.; Burt, S. K. Interactions of Azodicarbonamide (ADA) Species with the Model Zinc Finger Site: Theoretical Support of the Zinc Finger Domain Destruction in the HIV-1 Nucleocapsid Protein (NCp7) by ADA *The Journal of Physical Chemistry B* **2001**, *105*, 11341-11350.

103. Maynard, A. T.; Covell, D. G. Reactivity of zinc finger cores: analysis of protein packing and electrostatic screening *J. Am. Chem. Soc.* **2001**, *123*, 1047-1058.

104. Fischer, U.; Schulze-Osthoff, K. Apoptosis-based therapies and drug targets *Cell Death Differ.* **2005**, *12 Suppl 1*, 942-961.

105. Fulda, S.; Debatin, K. M. Extrinsic versus intrinsic apoptosis pathways in anticancer chemotherapy *Oncogene* **2006**, *25*, 4798-4811.

106. Adams, J. M. Ways of dying: multiple pathways to apoptosis *Genes Dev.* **2003**, *17*, 2481-2495.

107. Riedl, S. J.; Shi, Y. Molecular mechanisms of caspase regulation during apoptosis *Nat. Rev. Mol. Cell Biol.* **2004**, *5*, 897-907.

108. Reed, J. C. Bcl-2 and the regulation of programmed cell death *J. Cell Biol.* **1994**, *124*, 1-6.

109. Deveraux, Q. L.; Reed, J. C. IAP family proteins--suppressors of apoptosis *Genes Dev.* **1999**, *13*, 239-252.

110. Kurokawa, M.; Kornbluth, S. Caspases and kinases in a death grip *Cell* **2009**, *138*, 838-854.

111. Riedl, S. J.; Fuentes-Prior, P.; Renatus, M.; Kairies, N.; Krapp, S.; Huber, R.; Salvesen, G. S.; Bode, W. Structural basis for the activation of human procaspase-7 *Proc. Natl. Acad. Sci. U. S. A.* **2001**, *98*, 14790-14795.

112. Huang, Y.; Park, Y. C.; Rich, R. L.; Segal, D.; Myszka, D. G.; Wu, H. Structural basis of caspase inhibition by XIAP: differential roles of the linker versus the BIR domain *Cell* **2001**, *104*, 781-790.

113. Degterev, A.; Boyce, M.; Yuan, J. A decade of caspases *Oncogene* **2003**, *22*, 8543-8567.

114. Fuentes-Prior, P.; Salvesen, G. S. The protein structures that shape caspase activity, specificity, activation and inhibition *Biochem. J.* **2004**, *384*, 201-232.

115. Thornberry, N. A. The caspase family of cysteine proteases *Br. Med. Bull.* **1997**, *53*, 478-490.

116. Mittl, P. R.; Di Marco, S.; Krebs, J. F.; Bai, X.; Karanewsky, D. S.; Priestle, J. P.; Tomaselli, K. J.; Grutter, M. G. Structure of recombinant human CPP32 in complex with the tetrapeptide acetyl-Asp-Val-Ala-Asp fluoromethyl ketone *J. Biol. Chem.* **1997**, *272*, 6539-6547.

117. Hardy, J. A.; Lam, J.; Nguyen, J. T.; O'Brien, T.; Wells, J. A. Discovery of an allosteric site in the caspases *Proc. Natl. Acad. Sci. U. S. A.* **2004**, *101*, 12461-12466.

118. Scheer, J. M.; Romanowski, M. J.; Wells, J. A. A common allosteric site and mechanism in caspases *Proc. Natl. Acad. Sci. U. S. A.* **2006**, *103*, 7595-7600.

119. Fesik, S. W. Insights into programmed cell death through structural biology *Cell* **2000**, *103*, 273-282.

120. Crawford, E. D.; Wells, J. A. Caspase substrates and cellular remodeling *Annu. Rev. Biochem.* **2011**, *80*, 1055-1087.

121. Acehan, D.; Jiang, X.; Morgan, D. G.; Heuser, J. E.; Wang, X.; Akey, C. W. Three-dimensional structure of the apoptosome: implications for assembly, procaspase-9 binding, and activation *Mol. Cell* **2002**, *9*, 423-432.

122. Krueger, A.; Baumann, S.; Krammer, P. H.; Kirchhoff, S. FLICE-inhibitory proteins: regulators of death receptor-mediated apoptosis *Mol. Cell. Biol.* **2001**, *21*, 8247-8254.

123. Srinivasula, S. M.; Hegde, R.; Saleh, A.; Datta, P.; Shiozaki, E.; Chai, J.; Lee, R. A.; Robbins, P. D.; Fernandes-Alnemri, T.; Shi, Y.; Alnemri, E. S. A conserved XIAP-interaction motif in caspase-9 and Smac/DIABLO regulates caspase activity and apoptosis *Nature* **2001**, *410*, 112-116.

124. Riedl, S. J.; Renatus, M.; Schwarzenbacher, R.; Zhou, Q.; Sun, C.; Fesik, S. W.; Liddington, R. C.; Salvesen, G. S. Structural basis for the inhibition of caspase-3 by XIAP *Cell* **2001**, *104*, 791-800.

125. Mace, P. D.; Shirley, S.; Day, C. L. Assembling the building blocks: structure and function of inhibitor of apoptosis proteins *Cell Death Differ.* **2010**, *17*, 46-53.

126. Clapham, D. E. Calcium signaling *Cell* **2007**, *131*, 1047-1058.

127. Rizzuto, R.; Brini, M.; Murgia, M.; Pozzan, T. Microdomains with high Ca2+ close to IP3-sensitive channels that are sensed by neighboring mitochondria *Science* **1993**, *262*, 744-747.

128. Goll, D. E.; Thompson, V. F.; Li, H.; Wei, W.; Cong, J. The calpain system *Physiol. Rev.* **2003**, *83*, 731-801.

129. Devireddy, L. R.; Green, M. R. Transcriptional program of apoptosis induction following interleukin 2 deprivation: identification of RC3, a calcium/calmodulin binding protein, as a novel proapoptotic factor *Mol. Cell. Biol.* **2003**, *23*, 4532-4541.

130. Martin, S. J.; Mazdai, G.; Strain, J. J.; Cotter, T. G.; Hannigan, B. M. Programmed cell death (apoptosis) in lymphoid and myeloid cell lines during zinc deficiency *Clin. Exp. Immunol.* **1991**, *83*, 338-343.

131. Kuo, I. C.; Seitz, B.; LaBree, L.; McDonnell, P. J. Can zinc prevent apoptosis of anterior keratocytes after superficial keratectomy? *Cornea* **1997**, *16*, 550-555.

132. Truong-Tran, A. Q.; Ho, L. H.; Chai, F.; Zalewski, P. D. Cellular zinc fluxes and the regulation of apoptosis/gene-directed cell death *J. Nutr.* **2000**, *130*, 1459S-66S.

133. Cohen, G. M.; Sun, X. M.; Snowden, R. T.; Dinsdale, D.; Skilleter, D. N. Key morphological features of apoptosis may occur in the absence of internucleosomal DNA fragmentation *Biochem. J.* **1992**, *286 (Pt 2)*, 331-334.

134. Lazebnik, Y. A.; Cole, S.; Cooke, C. A.; Nelson, W. G.; Earnshaw, W. C. Nuclear events of apoptosis in vitro in cell-free mitotic extracts: a model system for analysis of the active phase of apoptosis *J. Cell Biol.* **1993**, *123*, 7-22.

135. Stennicke, H. R.; Salvesen, G. S. Biochemical characteristics of caspases-3, -6, -7, and -8 *J. Biol. Chem.* **1997**, *272*, 25719-25723.

136. Perry, D. K.; Smyth, M. J.; Stennicke, H. R.; Salvesen, G. S.; Duriez, P.; Poirier, G. G.; Hannun, Y. A. Zinc is a potent inhibitor of the apoptotic protease, caspase-3. A novel target for zinc in the inhibition of apoptosis *J. Biol. Chem.* **1997**, *272*, 18530-18533.

137. Peterson, Q. P.; Hsu, D. C.; Goode, D. R.; Novotny, C. J.; Totten, R. K.; Hergenrother, P. J. Procaspase-3 activation as an anti-cancer strategy: structure-activity relationship of procaspase-activating compound 1 (PAC-1) and its cellular co-localization with caspase-3 *J. Med. Chem.* **2009**, *52*, 5721-5731.

138. Velazquez-Delgado, E. M.; Hardy, J. A. Zinc-mediated allosteric inhibition of caspase-6 *J. Biol. Chem.* **2012**, *287*, 36000-36011.

139. Huber, K. L.; Hardy, J. A. Mechanism of zinc-mediated inhibition of caspase-9 *Protein Sci.* **2012**, *21*, 1056-1065.

140. Mufti, A. R.; Burstein, E.; Csomos, R. A.; Graf, P. C.; Wilkinson, J. C.; Dick, R. D.; Challa, M.; Son, J. K.; Bratton, S. B.; Su, G. L.; Brewer, G. J.; Jakob, U.; Duckett, C. S. XIAP Is a copper binding protein deregulated in Wilson's disease and other copper toxicosis disorders *Mol. Cell* **2006**, *21*, 775-785.

141. Makhov, P.; Golovine, K.; Uzzo, R. G.; Rothman, J.; Crispen, P. L.; Shaw, T.; Scoll, B. J.; Kolenko, V. M. Zinc chelation induces rapid depletion of the X-linked inhibitor of apoptosis and sensitizes prostate cancer cells to TRAIL-mediated apoptosis *Cell Death Differ.* **2008**, *15*, 1745-1751.

142. Hegde, M. L.; Bharathi, P.; Suram, A.; Venugopal, C.; Jagannathan, R.; Poddar, P.; Srinivas, P.; Sambamurti, K.; Rao, K. J.; Scancar, J.; Messori, L.; Zecca, L.; Zatta, P. Challenges associated with metal chelation therapy in Alzheimer's disease *J. Alzheimers Dis.* **2009**, *17*, 457-468.

143. Gupte, A.; Mumper, R. J. Elevated copper and oxidative stress in cancer cells as a target for cancer treatment *Cancer Treat. Rev.* **2009**, *35*, 32-46.

144. Grattan, B. J.; Freake, H. C. Zinc and cancer: implications for LIV-1 in breast cancer *Nutrients* **2012**, *4*, 648-675.

145. Briggs, G. E.; Haldane, J. B. A Note on the Kinetics of Enzyme Action *Biochem. J.* **1925**, *19*, 338-339.

146. Lineweaver, H.; Burk, D. The Determination of Enzyme Dissociation Constants *J. Am. Chem. Soc.* **1934**, *56*, 658-666.

147. Vivian, J. T.; Callis, P. R. Mechanisms of tryptophan fluorescence shifts in proteins *Biophys. J.* **2001**, *80*, 2093-2109.

148. Fischer, U.; Schulze-Osthoff, K. Apoptosis-based therapies and drug targets *Cell Death Differ.* **2005**, *12 Suppl 1*, 942-961.

149. Ghobrial, I. M.; Witzig, T. E.; Adjei, A. A. Targeting apoptosis pathways in cancer therapy *CA Cancer. J. Clin.* **2005**, *55*, 178-194.

150. West, D. C.; Qin, Y.; Peterson, Q. P.; Thomas, D. L.; Palchaudhuri, R.; Morrison, K. C.; Lucas, P. W.; Palmer, A. E.; Fan, T. M.; Hergenrother, P. J. Differential effects of procaspase-3 activating compounds in the induction of cancer cell death *Mol. Pharm.* **2012**, *9*, 1425-1434.

151. Putt, K. S.; Chen, G. W.; Pearson, J. M.; Sandhorst, J. S.; Hoagland, M. S.; Kwon, J. T.; Hwang, S. K.; Jin, H.; Churchwell, M. I.; Cho, M. H.; Doerge, D. R.; Helferich, W. G.; Hergenrother, P. J. Small-molecule activation of procaspase-3 to caspase-3 as a personalized anticancer strategy *Nat. Chem. Biol.* **2006**, *2*, 543-550.

152. Peterson, Q. P.; Goode, D. R.; West, D. C.; Ramsey, K. N.; Lee, J. J.; Hergenrother, P. J. PAC-1 activates procaspase-3 in vitro through relief of zinc-mediated inhibition *J. Mol. Biol.* **2009**, *388*, 144-158.

153. Lee, D.; Long, S. A.; Adams, J. L.; Chan, G.; Vaidya, K. S.; Francis, T. A.; Kikly, K.; Winkler, J. D.; Sung, C. M.; Debouck, C.; Richardson, S.; Levy, M. A.; DeWolf, W. E.,Jr; Keller, P. M.; Tomaszek, T.; Head, M. S.; Ryan, M. D.; Haltiwanger, R. C.; Liang, P. H.; Janson, C. A.; McDevitt, P. J.; Johanson, K.; Concha, N. O.; Chan, W.; Abdel-Meguid, S. S.; Badger, A. M.; Lark, M. W.; Nadeau, D. P.; Suva, L. J.; Gowen, M.; Nuttall, M. E. Potent and selective nonpeptide inhibitors of caspases 3 and 7 inhibit apoptosis and maintain cell functionality *J. Biol. Chem.* **2000**, *275*, 16007-16014.

154. Rotonda, J.; Nicholson, D. W.; Fazil, K. M.; Gallant, M.; Gareau, Y.; Labelle, M.; Peterson, E. P.; Rasper, D. M.; Ruel, R.; Vaillancourt, J. P.; Thornberry, N. A.; Becker, J. W. The three-dimensional structure of apopain/CPP32, a key mediator of apoptosis *Nat. Struct. Biol.* **1996**, *3*, 619-625.

155. Du, J. Q.; Wu, J.; Zhang, H. J.; Zhang, Y. H.; Qiu, B. Y.; Wu, F.; Chen, Y. H.; Li, J. Y.; Nan, F. J.; Ding, J. P.; Li, J. Isoquinoline-1,3,4-trione derivatives inactivate caspase-3 by generation of reactive oxygen species *J. Biol. Chem.* **2008**, *283*, 30205-30215.

156. Fang, B.; Fu, G.; Agniswamy, J.; Harrison, R. W.; Weber, I. T. Caspase-3 binds diverse P4 residues in peptides as revealed by crystallography and structural modeling *Apoptosis* **2009**, *14*, 741-752.

157. Zhou, Q.; Snipas, S.; Orth, K.; Muzio, M.; Dixit, V. M.; Salvesen, G. S. Target protease specificity of the viral serpin CrmA. Analysis of five caspases *J. Biol. Chem.* **1997**, *272*, 7797-7800.

158. Denault, J. B.; Salvesen, G. S. Expression, purification, and characterization of caspases *Curr. Protoc. Protein Sci.* **2003**, *Chapter 21*, Unit 21.13.

159. Gates, Z. P.; Stephan, J. R.; Lee, D. J.; Kent, S. B. Rapid formal hydrolysis of peptide-alphathioesters *Chem. Commun. (Camb)* **2013**, *49*, 786-788.

160. Feeney, B.; Clark, A. C. Reassembly of active caspase-3 is facilitated by the propeptide *J. Biol. Chem.* **2005**, *280*, 39772-39785.

161. Fu, G.; Chumanevich, A. A.; Agniswamy, J.; Fang, B.; Harrison, R. W.; Weber, I. T. Structural basis for executioner caspase recognition of P5 position in substrates. *Apoptosis* **2008**, *13*, 1291-1302.

162. Ganesan, R.; Mittl, P. R.; Jelakovic, S.; Grutter, M. G. Extended substrate recognition in caspase-3 revealed by high resolution X-ray structure analysis. *J. Mol. Biol.* **2006**, *359*, 1378-1388.

163. Feeney, B.; Pop, C.; Tripathy, A.; Clark, A. C. Ionic interactions near the loop L4 are important for maintaining the active-site environment and the dimer stability of (pro)caspase 3 *Biochem. J.* **2004**, *384*, 515-525.

164. Kyoung, M.; Kim, S. Y.; Seok, H. Y.; Park, I. S.; Lee, M. Probing the caspase-3 active site by fluorescence lifetime measurements *Biochim. Biophys. Acta* **2002**, *1598*, 74-79.

165. Park, I. S.; Moon, H. R.; Seok, H.; Lee, M. Rearrangement of tryptophan residues in caspase-3 active site upon activation *Biochim. Biophys. Acta* **2004**, *1700*, 5-9.

166. Boys, S. F.; Bernardi, F. The calculation of small molecular interactions by the differences of separate total energies. Some procedures with reduced errors. *Molecular physics, Mol. Phys.* **1970**, *19*, 553-566.

167. Kuchitsu, K.; Fukuyama, T.; Tamaru, Y.; Yoshida, Z.; Tabushi, I. Carbon-sulfur bond distances and sulfur valence angles in 5-thiabicyclo[2.1.1]hexane and 7-thiabicyclo[2.2.1]heptane as determined by gas electron diffraction *J. Am. Chem. Soc.* **1971**, *93*, 2799-2800.

168. Babor, M.; Greenblatt, H. M.; Edelman, M.; Sobolev, V. Flexibility of metal binding sites in proteins on a database scale *Proteins: Structure, Function, and Bioinformatics* **2005**, *59*, 221 - 230.